UNIVERSITAT ROVIRA i VIRGILI

CFD MODELING OF MULTIPHASE TURBULENT FLOWS IN A BUBBLE

COLUMN REACTOR

Mojtaba Goraki Fard

CFD Modeling of Multiphase Turbulent Flows in a Bubble Column Reactor

A Dissertation Presented

by

Mojtaba Goraki Fard

UNIVERSITAT ROVIRA I VIRGILI
2020

DOCTORAL THESIS
Nanoscience, Materials and Chemical Engineering

UNIVERSITAT ROVIRA I VIRGILI
CFD MODELING OF MULTIPHASE TURBULENT FLOWS IN A BUBBLE COLUMN REACTOR
Mojtaba Goraki Fard

UNIVERSITAT ROVIRA I VIRGILI
CFD MODELING OF MULTIPHASE TURBULENT FLOWS IN A BUBBLE COLUMN REACTOR
Mojtaba Goraki Fard

UNIVERSITAT ROVIRA I VIRGILI
CFD MODELING OF MULTIPHASE TURBULENT FLOWS IN A BUBBLE COLUMN REACTOR
Mojtaba Goraki Fard

CFD Modeling of Multiphase Turbulent Flows in a Bubble Column Reactor

A Dissertation Presented

by

Mojtaba Goraki Fard

Supervised
by

Dr. Youssef Stiriba
Prof. Francesc Xavier Grau

UNIVERSITAT ROVIRA I VIRGILI
Tarragona 2020

DOCTORAL THESIS
Nanoscience, Materials and Chemical Engineering

UNIVERSITAT ROVIRA I VIRGILI
CFD MODELING OF MULTIPHASE TURBULENT FLOWS IN A BUBBLE COLUMN REACTOR
Mojtaba Goraki Fard

UNIVERSITAT ROVIRA I VIRGILI
CFD MODELING OF MULTIPHASE TURBULENT FLOWS IN A BUBBLE COLUMN REACTOR
Mojtaba Goraki Fard

UNIVERSITAT ROVIRA i VIRGILI

Department of Mechanical Engineering-ETSEQ
Campus Sescelades-URV
Av. Països Catalans, 26, 43007 Tarragona, Spain
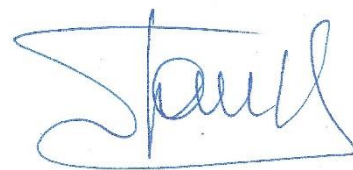
We **STATE** that the present study, entitled **"CFD Modeling of Multiphase Turbulent Flows in a Bubble Column Reactor"**, presented by Mojtaba Goraki Fard for the award of the degree of Doctor, has been carried out under our supervision at the **Department of Mechanical Engineering** of this university.

Tarragona, 30 de 10 de 2020

Doctoral Thesis Supervisors.

Dr. Youssef Stiriba   Prof. Francesc Xavier Grau

UNIVERSITAT ROVIRA I VIRGILI
CFD MODELING OF MULTIPHASE TURBULENT FLOWS IN A BUBBLE COLUMN REACTOR
Mojtaba Goraki Fard

ACKNOWLEDGMENTS

It is a great pleasure to acknowledge my deepest thanks to **Dr. Youssef Stiriba**, and **Prof. Francesc Xavier Grau** for providing me a chance to work under their supervision in the department of mechanical engineering of university of Rovira i Virgili as well as genuinely appreciative of them for great efforts, creative and comprehensive advices, guides and support during their supervision of this PhD work.

My thankfulness is also to my love, **Somayeh Baseri** for brilliant words of wisdom and never-ending love, and my parents**, Ebrahim Goraki Fard** and **Sedigeh Bolkheyr** due to preparing positive and lovely atmosphere and comprehensive supports to achieve my goals and aims in my life as well as my borders, **Dr. Ehsan Kianfar** and **Mohsen Goraki Fard** for their guides, encouragements and helps.

CFD MODELING OF MULTIPHASE TURBULENT FLOWS IN A BUBBLE COLUMN REACTOR

Mojtaba Goraki Fard

ABSTRACT

CFD Modeling of Multiphase Turbulent Flows in a Bubble Column Reactor

Mojtaba Goraki Fard

Ph.D., UNIVERSITY OF ROVIRA I VIRGILI

Directed by: Dr. Youssef Stiriba and Prof. Francesc Xavier Grau

This work presents a numerical study of turbulent two-phase flows in a 3D bubble column reactor using different models at different scales. The focus is first set on the hydrodynamics, flow regime transitions and mass transfer using the Euler-Euler mixture $k - \varepsilon$ model at wide ranges of superficial gas velocities. The emphasis is to assess the performance of this model and the analysis of the flow regime transition as well as the transient flow behavior inside the bubble column reactor. The quantification of the interfacial forces at different parts of the reactor were presented. Different models of the overall mass transfer coefficient estimation, namely the slip penetration model and the eddy cell model, are compared against the experimental data for the mass transfer analysis. The results reveal some of the characteristic features of homogeneous and heterogeneous flow regimes on the liquid circulation, gas holdup, turbulent fluctuations and gas-liquid mass transfer.

For transient and turbulent flow regimes, Euler-Euler large eddy simulations were used for a reliable scale resolution. The flow is more dynamic, and more details of the instantaneous local flow structure have been obtained including large-scale structures and vortices developed in the bubble plume edge. The power spectra was analyzed for both high and low frequencies regions at different gas velocities.

In addition to the different simulation scales, the three-dimensional Euler-Euler large eddy simulation model was used to calculate large-scale structures and their interaction with bubbles at inlet superficial gas velocities where vortical-spiral and turbulent flow regimes occur. We used a conditional sampling procedure of liquid velocity and gas hold-up time series to identify and educe the development of coherent flow structures which consists in a pair of counter-rotating vortices convected in a staggered pattern along the column in both the vortical-spiral and central plume regions. The yielded averaged topology of the three-dimensional large-scale structures was reconstructed and visualized using iso-surfaces.

UNIVERSITAT ROVIRA I VIRGILI
CFD MODELING OF MULTIPHASE TURBULENT FLOWS IN A BUBBLE COLUMN REACTOR
Mojtaba Goraki Fard

PUBLICATIONS

Indexed Publications:

- Fard, M.G., Stiriba, Y., Gourich, B., Vial, C. and Grau, F.X., 2020. Euler-Euler large eddy simulations of the gas–liquid flow in a cylindrical bubble column. *Nuclear Engineering and Design*, *369*, p.110823.

- Fard, M.G., Vernet, A., Stiriba, Y. and Grau, X., 2020. Transient large-scale two-phase flow structures in a 3D bubble column reactor. *International Journal of Multiphase Flow*, p.103236.

Conferences and Workshops:

- Mojataba Goraki Fard, Youssef Stiriba, Xavier F. Grau, "The numerical study of the effects of LES/RANS turbulent models to estimate flow structure within bubble column reactor (BCR)", XII International Conference on Computational Heat, Mass and Momentum Transfer (ICCHMT 2019), September, 2019, Rome, Italy

- Mojataba Goraki Fard, Youssef Stiriba, Xavier F. Grau, "The 3D numerical study of flow regimes within Bubble Column Reactor", 5th World Congress on Mechanical, Chemical, and Material Engineering (MCM'19), Agust, 2019, Lisbon, Portugal

- Mojataba Goraki Fard, Youssef Stiriba, Xavier F. Grau, "The effect of Coalescence Behavior of Liquid on Bubble Column Hydrodynamics", 2nd World Congress on Momentum, Heat and Mass Transfer (MHMT17), April, 2017, Barcelona, Spain

- Mojataba Goraki Fard, Workshop on Fluid Mechanics. Tarragona, Spain 20-21th July 2017

- Youssef Stiriba, Mojataba Goraki Fard, Xavier F. Grau, "Numerical simulation of turbulent two-phase flow in a 3D bubble column", International Workshop on complex turbulent flow. Tangier, Morocco 27th November 2017

UNIVERSITAT ROVIRA I VIRGILI
CFD MODELING OF MULTIPHASE TURBULENT FLOWS IN A BUBBLE COLUMN REACTOR
Mojtaba Goraki Fard

TABLE OF CONTENTS

LIST OF TABLES

LIST OF FIGURES

NOMENCLATURE

C_D	drag force coefficient
C_L	lift force coefficient
C_S	Smagorinsky constant
C_{TD}	turbulent dispersion coefficient
C_{VM}	virtual mass force coefficient
$C_{\mu,BI}$	constant in bubble induced turbulence model
d_B	bubble diameter, m
D	diameter of the column, m
g	gravity acceleration, m s^{-2}
H	height of the column, m
k_φ	turbulent kinetic energy of phase φ, m^2 s^{-2}
k_{SGS}	Sub-grid scale kinetic energy of phase, m^2 s^{-2}
$\mathbf{M}_\varphi$	total interfacial force acting between the phase φ and the other phase, N m^{-3}
$\mathbf{M}_\varphi^D$	drag force for the phase φ, N m^{-3}
$\mathbf{M}_\varphi^L$	lift force for the phase φ, N m^{-3}
$\mathbf{M}_\varphi^{TD}$	turbulent dispersion force for the phase φ, N m^{-3}
$\mathbf{M}_\varphi^{VM}$	virtual mass force for the phase φ, N m^{-3}
p	pressure, N m^{-2}
r	radial radius, m
R	column radius, m
Re_B	bubble Reynolds number
t	time, s
$\mathbf{U}_\varphi$	resolved velocity of phase φ, m s^{-1}
$\mathbf{U}_r$	relative velocity, m s^{-1}
U_G	superficial gas velocity, m s^{-1}

u'	fluctuating velocity, m s^{-1}
u_L	time-averaged axial liquid velocity, m s^{-1}
W	width of the rectangular column, m

Greek symbols

Δ	grid size, m
Δt	time step, s
Δx	grid spacing in x direction, m
Δy	grid spacing in y direction, m
Δz	grid spacing in z direction, m
α_φ	gas fraction of phase φ
$\nu_{L,L}$	liquid molecular viscosity, m^2 s^{-1}
ν_{SGS}	sub-grid scale viscosity, m^2 s^{-1}
ν_φ^{eff}	effective viscosity, m^2 s^{-1}
$\nu_{L,Tur}$	shear-induced turbulent viscosity, Pa s
$\mu_{L,BIT}$	bubble induced viscosity, Pa s
ρ	density, kg/m^3
τ_φ	shear stress of phase φ, Pa

Subscripts

φ	phase ($\varphi = G$; gas phase, $\varphi = L$; liquid phase)

Chapter 1

Introduction

1.1 Multiphase bubble column reactors in the process industry

Bubble column are widely used as multiphase flow contactors and reactors to carry out gas-liquid and gas-liquid-solid reactions in chemical, petrochemical, biochemical, and metallurgical processes. As to this, they are commonly utilized in processes involving relatively slow chemical reactions such as oxidations, hydrogenations, halogenations, etc., where oxygen is the most atmo-economic oxidizing agent and thus, only oxygen in the air is used as dispersed gas phase. In bubble column reactors (BCRs), the gas phase is dispersed in the form of tiny bubbles in a large volume of continuous liquid phase or liquid-solid suspensions medium. The liquid phase may be liquid or slurry liquid such as water or mixture water, while solid particles of different size and shapes are typically present in heterogeneously catalytic processes. Applications of BCRs in industrial processes also include the partial oxidation of ethylene to acetaldehyde, liquid phase methanol oxidation, Fisher-Tropsch synthesis, wastewater treatment, fermentations, bioleaching of mineral ores. In biochemical applications, they are utilized as bioreactors to produce industrially valuable bio-products such as enzymes, proteins, antibiotics, etc. Numerous processes which are presentative of reaction systems in bubble column can be found in (Schlüter et al., 1995, Kantarci et al., 2005, and Paul et al., 2018) and references therein.

Fig 1.1 shows typical bubble column reactors; their operation is very simple and offer numerous advantages, both in design and operations, over other types of multiphase reactors such as their simplicity with respect to construction, low operating and maintenance cost, no internal and moving parts are present to produce mixing, excellent reactors for processes requiring large interface area between the liquid and gas phases for mass transfer and,

eventually, high reaction rate, and good mixing in both phases with low energy consumption. Its design is simple and often consists in a cylinder tube filled with a liquid, distributed co-currently or counter-currently, and the gas phase is dispersed in the liquid phase using different types of gas distribution devices such as plate, sparger, and nozzle usually located at the bottom of the column, see Fig 1.1(a). More complex classes of bubble column may be found such as those with internal baffles or internal draft tubes, to enhance axial mixing and mass transfer, see Fig 1.1(b).
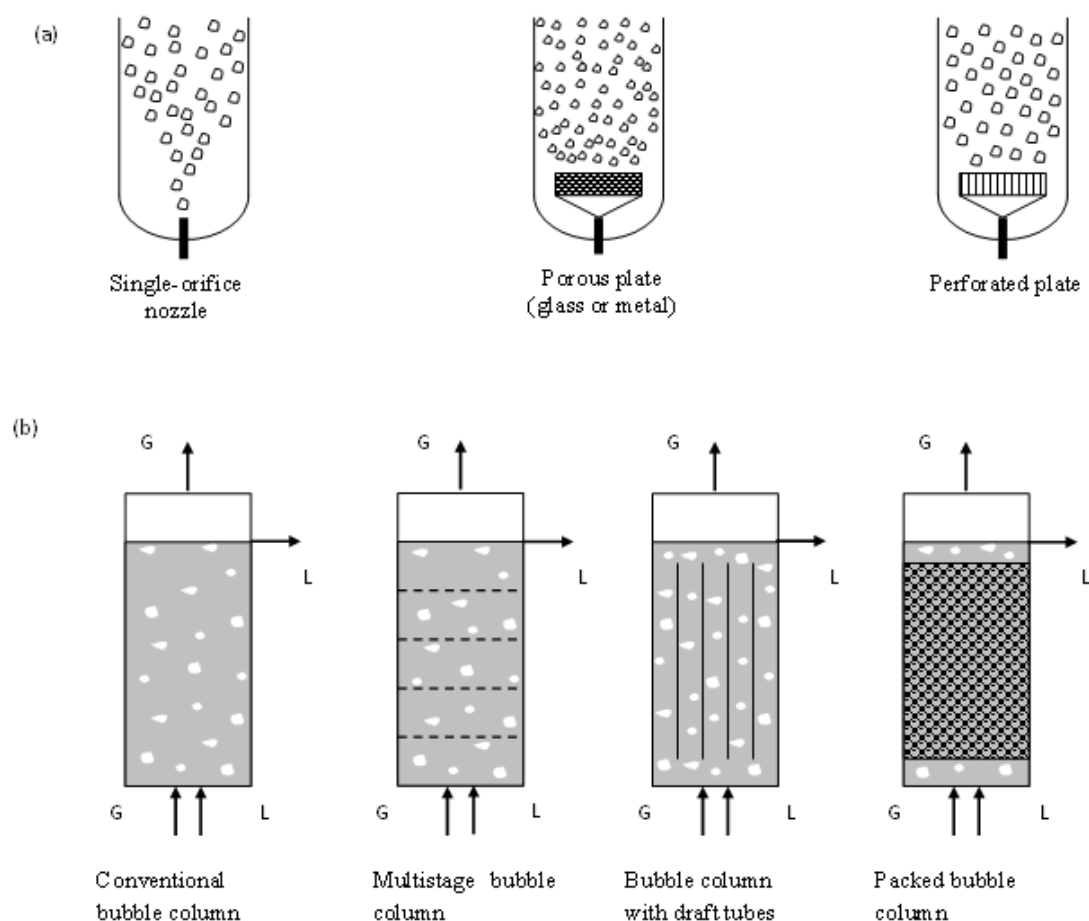
Fig 1.1 Schematic of typical bubble column configurations: (a) gas distributor with different holes distributions, (b): different bubble column reactors.

Despite the simple column configuration, arrangement and its popularity in the process industry, its design is still much closer to an art than design as pointed by (Joshi, 2001). The bubble dynamics inside the reactor are complex, and the detailed description of the complex interaction between the local fluid dynamics, hydrodynamics, mixing, mass transfer properties, and the reaction kinetics is usually not feasible. The design and operations of BCRs require the choice of many key parameters, for example, in the case of the gas-liquid BCRs:

- physicochemical properties of the gas and liquid phases like density, viscosity, and surface tension, etc., which affects the interfacial mass transfer and reactions kinetics,

- operating parameters like gas and liquid flow rates and pressure,

- dimensions of the geometry like the height and the diameter of the column,

- distributor type and geometry which affect the primary bubble size distribution,

- presence of solid catalyst,

- presence of internals.

Other key design parameters and non-operating parameters for either gas-liquid or gas-liquid-solid cases may be found in several references (Vial and Stiriba, 2013).

Several lectures and publications have presented to measure and analyze different key flow parameters that affect the design of efficient bubble column reactors employing comprehensive measurements such as Particle Image Velocimetry (PIV) (Chen et al. 1994, Lin et al. 1996), Laser Doppler Anemometry (LDA) (Vial et al. 2001), and/or computational fluid simulations (CFD). CFD is increasingly used for the prediction of the flow pattern of multiphase flow reactors in the last three decades because of the difficulties that are still found in the design and scale-up of such reactors, see for instance Joshi, 2001 and Besagni et al. 2018 and references therein. Table 1.1 lists a summary of some relevant information of several literatures reviewed for bubble column reactors with special emphasis on the range of the inlet superficial gas velocity considered, closures for interfacial forces, and turbulence models employed for the numerical simulations.

Most of the numerical studies outlined in Table 1.1 have focused on low superficial gas velocity values (≤ 40 mm/s) and atmospheric pressure where homogeneous regime prevails. Such regime is characterized by almost uniformly bubble size distribution and low liquid turbulence (Mudde 2005 and Camarasa et al. 1999). At high gas flow rate the flow regime changes from homogeneous bubbly flow to turbulent bubbly flow and heterogeneous churn flow, depending on the gas throughput, where the flow through the column becomes unstable, highly irregular and the bubble cluster in form of swarms (Groen, 2004) leading to large-scale circulation pattern, wide bubble diameter distribution due to coalescence and breakup phenomena and turbulent flow structure for further high superficial gas-velocities. Those flow regimes are separated by the transition flow regime and took place at 4 cm/s superficial gas velocity from previous experimental works (Gourich et al. and Vial et al. 2001) and the linear stability theory of Snip et al. 1992 and Cockx et al. 2004. Other flow regimes such as slug and annular were observed in many situations, however, BCRs in the process industry generally operate in either the homogeneous or heterogeneous churn flow regimes. Observed flow regimes in BCRs are displayed in Fig. 1.2 where clusters of bubbles move upward in a spiral manner from the center of column and downward in the near-wall region (Chen et al. 1994). Furthermore, various turbulence models have been used in the literature to capture the hydrodynamics properties and describe the flow pattern in the BCRs (Table 1.1). For industrial applications, the Eulerian-Eulerian modelling, which employs ensemble-averaged equations to describe the time-dependent motion of the mixture in a macro sense, is the most adopted approach for numerical simulations, especially for highly dispersed void fraction reactors. The extension of the single phase standard $k - \varepsilon$ model has been intensively used to model turbulence in two-phase flow, where turbulence is associated to the dominant continuous phase and the dispersed phase can only respond or modify the continuous phase turbulence.

Reference	Domain	U_G (cm/s)	Aspect ratio and areation	Multiphase model	CFD software	Drag	Lift	Virtual mass	Turbulent dispersion	Turbulence model
Parekh and Rzehak, 2017	2D axisymmetric	1.5 - 20	H/D = 80, 66, 46	E-E	OpenFOAM	Ishii Zuber	Tomiyama	0.5	Burns et al.	RSM
Saleh et al., 2018	3D	1.5 - 3.25	H/D = 7.7	E-E	ANSYS - CFX	Ishii Zuber	Tomiyama	0.5	Lopez de Bertodano	$k - \varepsilon$ model
Bhusare et al., 2017	3D	1.4 - 13.2	H/D = 10	E-E	OpenFOAM	constant	constant	0.5	0.008 - 0.07	mixture $k-\varepsilon$ model
Khan et al., 2017	3D	2.4 and 10		E-E	ANSYS - CFX	Ishii Zuber	Tomiyama	0.5	Lopez de Bertodano	$k-\varepsilon$, RSM, and LES model
Asad et al., 2017	3D	0.49	W = 0.15 m, H/L = 13.5	VOF	OpenFOAM	Ishii Zuber, Tomiyama, Simonnet	Tomiyama	0.5	NA	Spalart-Allmaras: Near the wall LES: in the bulk of flow
Eppinger et al., 2015	3D	20	W = 0.05 m, H/L = 2.25	E-E	STAR-CCM+	constant	Tomiyama	0.5	NA	$k - \varepsilon$ model (realizable)
Ma el al., 2015b	3D	0.3 and 1.3	W = 0.24 m, H = 0.72, D = 0.072 m	E-E	ANSYS - CFX	Ishii Zuber	Tomiyama	0.5	NA	LES
Selma et al., 2010	3D	0.14	W = 0.05 m, H/L = 6, sparger area 4×10^{-6}m², 9×10^{-6}m², 2.5×10^{-5}m²	E-E	OpenFOAM	Schiller-Naumann	Tomiyama	0.25	NA	$k - \varepsilon$ model
Rampure et al., 2009	3D	1.0 - 10	H/L = 10, sparger area 1.13 %	E-E	ANSYS - Fluent	Modified Ishii Zuber	NA	NA	NA	$k - \varepsilon$ model (mixture)
Law et al., 2018	2D	5.0 - 40	H/L = 10	E-E	ANSYS - Fluent	Schiller-Naumann and White	NA	0.5	NA	$k - \varepsilon$ model
Rampure et al., 2003	3D	0.16 - 0.83	H/L = 10, sparger area 3.5×10^{-4}m²	E-E	ANSYS - Fluent	Modified Ishii Zuber	NA	NA	NA	$k - \varepsilon$ model
Buwa et al., 2006	3D	0.16 - 0.83	W = 0.05 m, H/L = 6, sparger area 4×10^{-6}m², 9×10^{-6}m², 2.5×10^{-5}m²	E-L	ANSYS - Fluent	Tuschiya	Tomiyama	0.5	NA	$k - \varepsilon$ model
Bech, 2005	3D	0.16 - 0.83	W = 0.05 m, H/L = 2.25	E-E	ANSYS - Fluent	Rusche Issa	Tomiyama	NA	NA	LES, $k - \varepsilon$ model
Buwa and Ranade, 2004	3D	0.16 - 0.83	W = 0.05 m, H/L = 6, sparger area 4×10^{-6}m², 9×10^{-6}m², 2.5×10^{-5}m²	E-E, E-L	ANSYS - Fluent	Tuschiya	Tomiyama	0.5	NA	$k - \omega$ model
Buwa and Ranade, 2003	3D	0.16 - 0.83	W = 0.05 m, H/L = 6, sparger area 4×10^{-6}m², 9×10^{-6}m², 2.5×10^{-5}m²	E-E	ANSYS - Fluent	Tuschiya	Tomiyama	0.5	NA	$k - \varepsilon$ model
Rampure et al., 2003	3D	1.0 - 20.0	H/L = 10, sparger area 3.5×10^{-4}m²	E-E	ANSYS - Fluent	Ishii Zuber	Tomiyama	0.5	NA	$k - \varepsilon$ model
Buwa et al., 2002	3D	0.16 - 0.83	W = 0.05 m, H/L = 6, sparger area 4×10^{-6}m², 9×10^{-6}m², 2.5×10^{-5}m²	E-E	ANSYS - Fluent	Modified Ishii Zuber	0.5	0.5	NA	$k - \varepsilon$ model
Deen et al., 2001	3D	0.49	W = 0.15 m, H/L = 3, sparger area 3.5×10^{-4}m²	E-E	ANSYS - CFX	Ishii Zuber	0.5	0.5	NA	$k - \varepsilon$ model and LES based on Smagorinsky
Ranade, 1997	2D axisymmetric	2.0 - 8.0	H/D = 32.6, 23.6, 15.5, 7.5	E-E	In-house code SPARE	Ishii Zuber	NA	NA	NA	$k - \varepsilon$ model
Boisson and Malin, 1996	3D	0.038, 0.08	H/D = 14.75, 9.93	E-E	PHOENICS	Ishii Zuber	0.5	0.5	NA	$k - \varepsilon$ model
Ranade, 1992	2D axisymmetric	1.0 - 10.0	H/D = 1, sparger area 64%, 36%	E-E	In-house code TPFLOW	NA	NA	NA	NA	$k - \varepsilon$ model
Kannan et al., 2019	3D	3, 10, 20, 40	H/D = 7.895 4×10^{-6}m², 9×10^{-6}m², 2.5×10^{-5}m²	E-E	OpenFOAM	Modified Ishii Zuber	NA	NA	NA	Mixture $k - \varepsilon$ model
Zhang et al. 2006	3D	0.49	W = 0.15 m, H/L = 3, sparger area 3.5×10^{-4}m²	E-E	ANSYS - CFX	Ishii Zuber	0.5	0.5	NA	LES based on Smagorinsky and Vremen SGS
Dhotre et al. 2008	3D	0.49	W = 0.15 m, H/L = 3, sparger area 3.5×10^{-4}m²	E-E	ANSYS - CFX	Ishii Zuber	0.5	0.5	Lopez de Bertodano	$k - \varepsilon$ model and LES based on Smagorinsky and Germano SGS
Niceno et al. 2008	3D	0.49	W = 0.15 m, H/L = 3, sparger area 3.5×10^{-4}m²	E-E	ANSYS - CFX	Ishii Zuber	0.5	0.5	Lopez de Bertodano	LES based on Germano SGS and one-equation model based on SGS kinetic energy
Ekambara and Dhotre, 2010	3D	2	H = 0.9 m, D = 0.15 m, multipoint sparger	E-E	ANSYS - CFX	Ishii Zuber	Tomiyama	0.5	Lopez de Bertodano	Standard $k - \varepsilon$, $k - \omega$, RNG $k - \varepsilon$ RSM and LES based on Smagorinsky SGS
Masood and Delgado, 2014	3D	0.49	W = 0.15 m, H/L = 3, sparger area 3.5×10^{-4}m²	E-E	ANSYS - CFX	Ishii Zuber	0.5	NA	NA	Standard $k - \varepsilon$, and DES based on SST $k - \omega$
Ma et al. 2015a	3D	0.49	W = 0.15 m, H/L = 3, sparger area 3.5×10^{-4}m²	E-E	ANSYS - CFX	Ishii Zuber	Tomiyama	0.5	NA	SAS and LES based on Smagorinsky SGS
Masterov et al. 2018	3D	0.49	W = 0.15 m, H/L = 3, sparger area 3.5×10^{-4}m²	E-E	In-house code FoxBerry	Tomiyama	Tomiyama	0.5	NA	DES based on SA, $k - \varepsilon$, SST $k - \omega$ and LES based on Smagorinsky and Vreman SGS
Tang et al. 2020	3D	12	W = 0.15 m, H/L = 3, sparger area 3.5×10^{-4}m²	E-E	ANSYS-Fluent	Schiller-Naumann	Magnaudet-Legendre	0.5	Lopez de Bertodano	W-A one-equation

Table 1.1 – Summary of previous numerical simulations of gas-liquid flow in bubble columns using different reactor geometry, operating conditions and two-fluid models.

5

The turbulent viscosity is assumed as a contribution of shear- and bubble induced turbulence (Sato and Sekogushi 1975), or as a production source terms in the two-equation turbulence model (Mudde and Simonin 2001, Pfleger and Beker 2001, Bel F'dhila and Simonin 1992, Lopez de Bertodano et al. 1994, Troshko and Hassan 2001, Rusche 2002). The model becomes more popular due to its simplicity and reasonable accuracy at reasonable computational cost. A mixture $k - \varepsilon$ model has been proposed by Behzadi et al. 2004 for gas-liquid and liquid-liquid flow at high volume fraction of the dispersed phase. We refer the reader to the review of Pourtousi et al. 2014 and the recent work of Tang et al. 2020 for a review of different RANS model ($k - \varepsilon$, $k - \omega$, Reynolds stress model (RSM), WA) and a discussion of their accuracy in certain multiphase flow processes.

Another approach for accurate representation of turbulence phenomena in bubbly flows is the Eulerian-Eulerian large eddy simulations (LES) which combines interpenetrating continua modelling interface details with the LES for computing explicitly the largest and most energetic scales, while modelling the sub-grid scales of turbulence (Niceno et al. 2008, and Tabib and Schwarz 2011). The Eulerian-Eulerian LES models, namely the zero-equation model of Smagorinsky and the one-equation SGS model, can capture the transient bubble and surrounding eddies interaction as well as the dynamic motion of the bubble plume. Furthermore, the Eulerian-Eulerian LES models are anisotropic in largest resolved scales in contrast to RANS models which assume isotropic turbulence. However, in such approach the cell size of the computational mesh must be larger than the bubble size which make the basic assumption of LES invalid (Nikeno et al. 2008). The LES two-phase flow model is more desirable for large-scale BCRs or churn-turbulent flow, and few studies have been done than the RANS models.
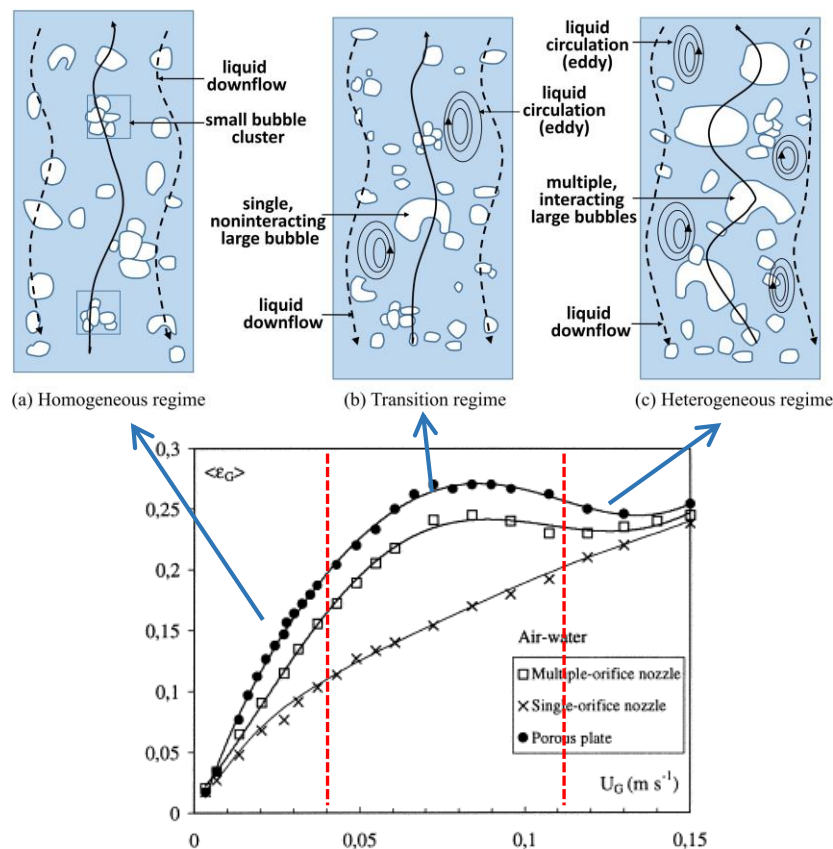
Fig 1.2 Observed regime transitions in a bubble column reactor (Vial et al. 2001 and Ruthiya et al. 2005).

Another important challenging issue in modelling multiphase flows in BCRs concerns the description of the interfacial forces that represent the momentum exchange between phases. Interphase forces are modelled through the combination of the drag, lift, added mass, turbulence dispersion forces, etc. Various closure laws have proposed and analyzed in several works in pair or simultaneously, see the works of Pourtousi et al. 2014, Jakobsen et al. 2005, Kulkarani et al. 2007, Tabib et al. 2008, and Masood and Delgado 2014 for a general review of empirical correlations for interfacial momentum transfer and their effects on flow pattern inside BCRs.

Interfacial force closures are a complex function of bubble size and shape, physical properties of the multiphase flow system, relative velocity, and void fractions, sparger configuration, operating pressure, and the presence of other components in the liquid phase (i.e., organic solvent,

surfactants, etc.), see Goen 2004 and Joshi 1998, which turn to depend on the bubble Reynolds number (Re_B), the Eötvos number (Eo), and the Morton number (M) given by

$$Re_B = \frac{\rho_L |\mathbf{U}_G - \mathbf{U}_L| d_B}{\mu_L},$$

$$Eo = \frac{g |\rho_G - \rho_L| d_B^2}{\sigma},$$

$$M = \frac{g |\rho_G - \rho_L| \mu_L^4}{\rho_L^2 \sigma^3}$$

Accurate and correct modelling of interfacial force remain open question in CFD modeling of multiphase turbulent flows. Therefore, one of the objectives of the present study is to analyze different interfacial forces on high aspect bubble column in churn-turbulent flows and focus on quantifying interfacial forces by calculating the instantaneous and time-averaged magnitude in different part of the reactor with special emphasis on the turbulent dispersion force. Such numerical calculations would help to compare different interfacial forces locally and how much effect it has on the flow profile.

1.2 Scales and structures in bubbly flows

Both experimental studies and numerical simulations reveal the existence of the spectrum of turbulent structures for transition and heterogeneous flow regimes and have been extensively studied in the published literature. For instance, Chen et al. 1994 reported that as we increase the inlet gas flow rate, clusters of bubbles travel through the column center carrying the liquid in almost a spiral rotating movement and small bubbles spirally downward in the near-wall region.
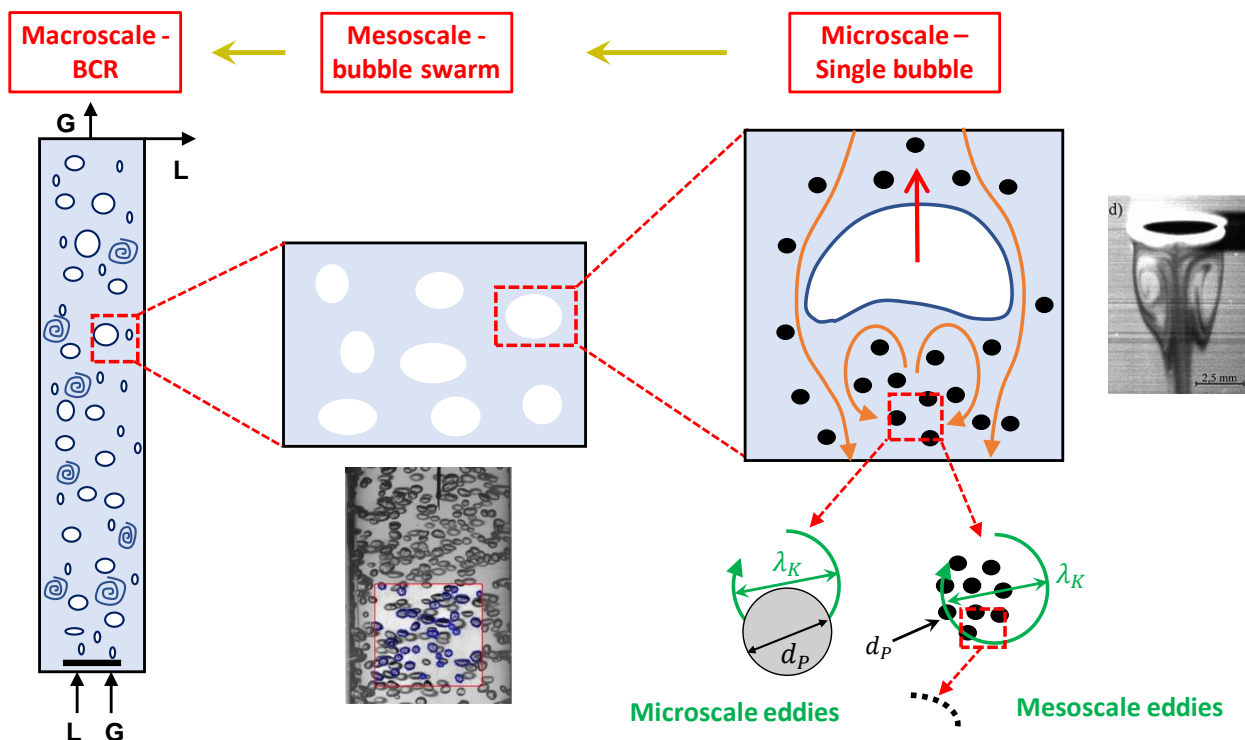
Fig 1.3 Different scales and structures in a churn-turbulent flow inside a bubble column reactor.

The numerical simulation of multiphase reactors such as BCRs is intimately linked to the notion of scale since the small scales are coupled with the medium and largest ones and then emerges different flow regimes. Fig 1.3, displays different scales gas-liquid-solid reactor, we can identify

- a macroscopic scale or reactor-scale with different liquid circulation cells and bubble plumes, typically from 1 to 10 m,

- a medium or mesoscale, where the interaction between turbulent eddies with dispersed bubbles and different solid particles take places. This scale is caused due to the swarm of rising bubble at large gas fractions and high superficial gas velocities.

- the small scale or bubble-scale where turbulence is generated in the wake behind the bubble to its movement.

- for mass transfer and chemical reaction modelling, other scales like particle scale in suspension, enzyme or cell supports and small catalyst, due to the small scales of liquid turbulence are also present,

- the scale of the reactive interface which considers the phenomena of adsorption and reaction.

According to the flow regimes and change in mixing, one can distinguish between different turbulences and integral scales of such turbulences, Risso 2018 and Panicker et al. 2020. For instance, in the homogeneous flow regime the injected bubbles generate the wakes behind them and the collective motions agitate the liquid and induce flow disturbances. Such agitation is referred by many authors as a bubble-induced turbulence or pseudo-turbulence, see Lance and Bataille 1991 and Risso 2018. The integral length scale of this turbulence is the order of the single bubble that can be resolved by direct numerical simulations (DNS) of the Navier-Stokes equations, and adds a sub-grid scale to the two-fluid model. At high gas flow rate, buoyancy forces become stronger and produce turbulent fluctuations. On one side, such turbulence gives rise to energy cascade, similar to turbulent production as a single-phase flow, as the buoyance gradient become stronger. The resulting turbulent fluctuations are referred to Buoyancy Driven Turbulence (BDT) and has a larger integral length scales that can be resolved by the two-fluid model, see section 2 and 3. On the other side, the turbulence generated by the bubble-rising motion induces liquid velocity fluctuations and therefore, inject energy in a narrow ranges of scale and produce turbulence with different statistical properties where the power spectral density decreased approximately as the −3 power of the wave number, see the works of Lance and Bataille 1991, Prakash et al. 2005, Risso 2018, and section 3. It thus concluded that the phenomena to be simulated depends on the scale to which the calculation is made.

The column becomes filled with transient circulation cells much larger than the bubble sizes in different parts of the reactor. Various authors discussed different circulation cell models

(e.g., overall circulation cell pattern, the 'donut' model of Joshi and Sharma, counterrotating donut cells, non-circulation cell model, etc.), see Groen, 2004 and Joshi et al., 2002 and section 4. The above references suggest that further analysis is required for identification of different unsteady structures in bubbly flow with high inlet gas flow rate using sophisticated turbulence models which motivated employing Eulerian-Eulerian LES with bubble-induced turbulence in transient and churn-turbulent flow regimes.

1.3 The objective of the project

The major goal of this thesis is to advance the understanding of the hydrodynamic and gas-liquid mass transfer in bubble columns. We perform a multiscale analysis using the two-equation mixture $k - \varepsilon$ model, the LES model like Smagorinsky, and the one-equation SGS LES model that allow the prediction of the gas hold-up and liquid velocity, and the assessment of the above turbulence models. In addition, we use a conditional sampling procedure of liquid velocity and gas hold-up time series to identify and educe the development of coherent flow structures. Specifically, four major objectives are set for this study:

- To test and assess the performance of the Euler-Euler mixture RANS model for simulations of gas-liquid two phase flow in high ratio BCRs operated with uniform aeration and at superficial gas velocities in the range of 1.35 – 8.4 cm/s covering different flow regimes. This study aims at studying different combination of interfacial momentum forces, closure correlations, bubble diameters, and computational meshes. Therefore, the goal is in part to establish a generic two-phase model with appropriate closures to predict the hydrodynamic and regime transition for broader ranges of flow conditions and compute mean scales of the flow.

- The previous two-phase flow model is employed to analyze the mass transfer.

- To simulate different flow scales using Eulerian-Eulerian LES for turbulent-churn heterogeneous flow regimes. We analyze the performance of Smagorinsky model and the one-equation SGS model, as well as the power spectral density of the resolved liquid velocities.

- To use conditional sampling technique with the sub-grid scale modeling based on the one-equation model and the bubble-induced turbulence to numerically investigate transient large flow structures associated with rising bubbles. Different coherent structures were identified in the transient and churn-turbulent flow regimes.

To accomplish these goals experimental data of Camarasa et al. 1999 and Gourich 2008 were used to validate the computational models. The column height (*H*) is 2 m and diameter (*D*) is 10 cm which makes the ratio H/D of 20. Water was filled up to a height of 1.5 m and the air was injected from the bottom through multiple-orifice nozzle consisting of 62 holes of 1 mm, and a porous glass plate of 10-16 μm mean pore diameter over the entire column cross-section. We refer the reader to the references for more information on operating flow conditions.

The open source toolkit Open-FOAM® (Open Field Operation And Field Manipulation) is used to carry out all the calculations. The Open-FOAM platform is a registered trademark of OpenCFD Limited, the developer of the Open-FOAM software. It is now gaining more popularity in CFD and chemical engineering community and became an open and unified research code for many research groups and industrial companies, since its library provides an easily extendable framework to implement new solver for the governing equations model and extensive range of features which include models, boundary conditions and robust algorithms, etc. However, up to our knowledge, most of the numerical simulations have been performed using in-house codes or licensed commercial packages which makes difficult reproducibility and accessibility. Less numerical simulations have conduced and validated for bubble columns in turbulent-churn heterogeneous flow regimes with Open-FOAM libraries. Therefore, in our

studies the twoPhaseFlowFoam solver implemented in Open-FOAM v.4.0.0 is used and validated.
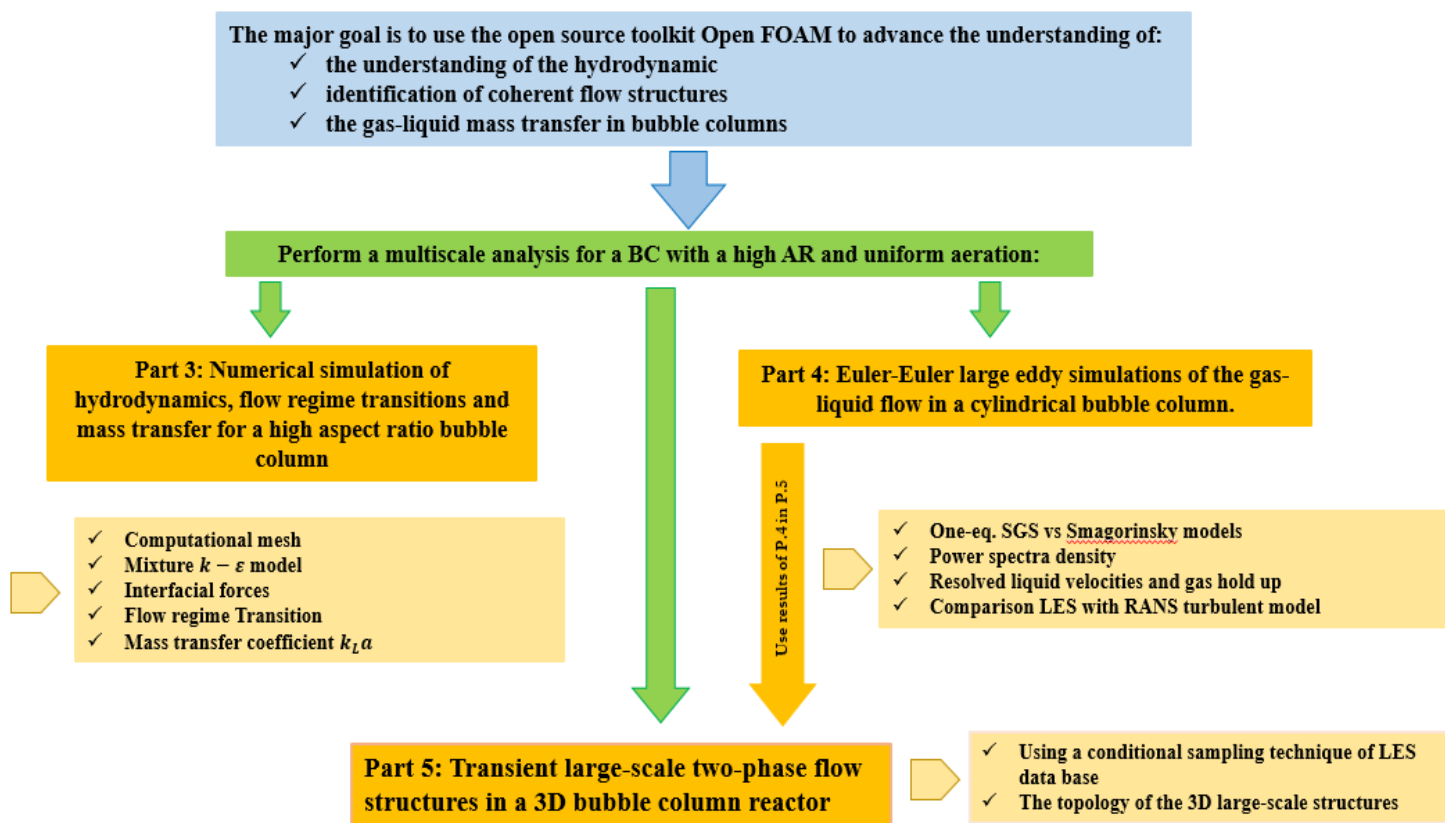
Fig 1.4 Summary of research plan in this dissertation

This thesis dissertation consists of the following parts and summarized in figure 1.4:

- Part 1: Introduction of the bubble column reactors, its uses in process engineering, and some highlights of this research project.

- Part 2: The Euler-Euler two-fluid models of scale resolving simulations including the mixture $k - \varepsilon$ model and the large eddy simulation.

- Part 3: Numerical simulation of hydrodynamics, flow regime transitions and mass transfer for a high aspect ratio bubble column. Part of this work were presented in the ***World Congress on Mechanical, Chemical, and Material Engineering, 2019.***

- Part 4: Euler-Euler large eddy simulations of the gas-liquid flow in a cylindrical bubble column. This work is accepted for publication in the journal of *Nuclear Engineering Design, 369 (2020), 110823.*

- Part 5: Transient large-scale two-phase flow structures in a 3D bubble column reactor. This work is accepted for publication in *International Journal of Multiphase Flows, 127 (2020), 102236.*

- Part 6: Summary and comments of the main contributions of this study.

Chapter 2

The two-fluid models

In the framework of Euler-Euler turbulent multiphase flow model for hydrodynamic simulations of large scales gas-liquid reactors such as bubble columns, two approaches of two-fluid models are used in this work. Both approaches, start from the two-fluid Navier-Stokes equations and then apply Reynolds averaging followed by phase averaging or spatial filtering. Hence, we predict macro- and meso-scale bubble induced turbulence. In the statistical and subgrid-scale modelling approaches additional unclosed terms appear such as those related to the pseudo-turbulent liquid phase fluctuations or those encompassing interfacial forces.

2.1 The mixture $k - \varepsilon$ two-phase flow model

A detailed description of the Euler-Euler two fluid model can be found in several textbooks, PhD dissertations, research papers and CFD software documentations, such as Drew and Lahey 1988, Drew and Passman 1999, Ishii and Hibiki 2011, Hill 1998, Rusche 2003, Panicker et al. 2020 and Weller 2005. The first two-phase flow model used to run RANS simulations is the mixture $k - \varepsilon$ model, see section 3. The construction of the model starts from the continuity and momentum equations, and then conditionally averaged by multiplying by the indicator function I_φ and ensemble averaging. The formulation closely follows the procedure outlined by Weller 2005, where the mass and momentum equations for the phase φ are given by

$$\frac{\partial(\rho_\varphi \alpha_\varphi)}{\partial t} + \nabla \cdot (\rho_\varphi \alpha_\varphi \mathbf{U}_\varphi) = 0 \tag{1}$$

15

$$\frac{\partial(\rho_\varphi \alpha_\varphi \mathbf{U}_\varphi)}{\partial t} + \nabla \cdot (\rho_\varphi \alpha_\varphi \mathbf{U}_\varphi \mathbf{U}_\varphi) \tag{2}$$

$$= -\alpha_\varphi \nabla p_\varphi + \alpha_\varphi \rho_\varphi \mathbf{g} - \nabla \cdot (\alpha_\varphi \rho_\varphi \boldsymbol{\tau}_\varphi) + \nabla \cdot (\alpha_\varphi \rho_\varphi \mathbf{R}_\varphi) + \mathbf{M}_\varphi$$

Here α_φ is the volume fraction of each phase, $\mathbf{U}_\varphi$ is the phase resolved velocity, and $\boldsymbol{\tau}_\varphi$ represents phase viscous stress tensor, $\mathbf{I}$ is the identity tensor, $\mathbf{R}_\varphi$ is Reynolds stress, and $\mathbf{M}_\varphi$ stands for the averaged inter-phase momentum transfer of phase φ. These last two terms arising from averaging require modelling and special attention.

The Reynolds-stress tensor in the RANS approach is modelled as

$$\mathbf{R}_\varphi = -v_\varphi^t \left[\nabla \mathbf{U}_\varphi + (\nabla \mathbf{U}_\varphi)^T - \frac{2}{3}(\nabla \cdot \mathbf{U}_\varphi)\mathbf{I} \right] + \frac{2}{3} k_\varphi \mathbf{I} \tag{3}$$

where k_φ is the turbulent kinetic energy of phase φ and v_φ^t the turbulent viscosity of phase φ, which is modelled from the mixture $k - \varepsilon$ model. As pointed out by Panicker et al. 2020, the literature of multiphase flow turbulence is flooded by $k - \varepsilon$ models, which assume the turbulence dictated by the continuous phase. However, the work of Behzadi et al. 2004 developed a mixture model to tackle turbulence at high phase fraction regimes and converts to the single-phase form in the extreme limits of the phase fractions. The $k - \varepsilon$ model (Behzadi et al. 2004) for the mixture of the continuous and dispersed phase is adopted to model the turbulence and compute the shear induced dynamic viscosity. The original model has shown improvement in the prediction of two-phase flows over other models considering only the turbulent kinetic energy on the continuous phase. Therefore, in the context of mixture $k - \varepsilon$ model, we solve two phase-averaged transport equations for the mixture kinetic energy (k_m) and turbulent dissipation rate for mixture (ε_m)

$$\frac{\partial}{\partial t}(\rho_m k_m) + \nabla \cdot (\rho_m k_m \mathbf{U}_m) = \nabla \cdot \left(\frac{\mu_m^t}{\sigma_k} \nabla k_m\right) + P_{k,m} - \rho_m \varepsilon_m + S_{k,m} \tag{4}$$

$$\frac{\partial}{\partial t}(\rho_m \varepsilon_m) + \nabla \cdot (\rho_m \varepsilon_m \mathbf{U}_m) \tag{5}$$

$$= \nabla \cdot \left(\frac{\mu_m^t}{\sigma_\varepsilon} \nabla \varepsilon_m\right) + \frac{\varepsilon_m}{k_m}\left(C_{\varepsilon 1} P_{k,m} - C_{\varepsilon 2} \rho_m \varepsilon_m\right) + C_{\varepsilon 3} \frac{k_m}{\varepsilon_m} S_{k,m}$$

where the mixture turbulent quantities are related to those of individual phases through the turbulent response coefficient C_t, which is defined as the ratio of the *r.m.s.* values of the gas velocity fluctuations to those of the liquid phase

$$C_t = \frac{U_G'}{U_L'} \tag{6}$$

and was modified to account for the influence for the gas volume fraction as in Rusche 2002. The other terms $\mathbf{U}_m$, $P_{k,m}$ and $S_{k,m}$ stand for the mixture velocity, turbulent production and the source term, see section 3.

To improve the ability of the model for predicting turbulent gas-liquid in bubble column reactors in the near wall region, a low Reynolds number can be applied to the original mixture $k - \varepsilon$ model and the turbulent dissipation rate for mixture becomes

$$\frac{\partial}{\partial t}(\rho_m \varepsilon_m) + \nabla \cdot (\rho_m \varepsilon_m \mathbf{U}_m) \tag{7}$$

$$= \nabla \cdot \left(\frac{\mu^t}{\sigma_\varepsilon} \nabla \varepsilon_m\right) + \frac{\varepsilon_m}{k_m}\left(C_{\varepsilon 1} f_1 P_{k,m} - C_{\varepsilon 2} \rho_m f_2 \varepsilon_m\right) + C_{\varepsilon 3} \frac{k_m}{\varepsilon_m} S_{k,m}$$

where model relations are given by

$$\mu^t = f_\mu \mu_m^t, \qquad f_1 = 1$$

$$f_2 = \left(1 - \frac{2}{9}\exp\left(-\frac{R_T}{6}\right)^2\right)\left(1 - \exp\left(-\frac{y^+}{5}\right)\right)^2,$$

$$f_\mu = \left(1 - \exp\left(-\frac{y^+}{70}\right)\right)\left(1 + \frac{3.45}{\sqrt{R_T}}\right)$$

$$y^+ = \frac{\rho_L \mu_\tau (R - r)}{\mu_L}, \qquad R_T = \frac{\rho_L k^2}{\mu_L \varepsilon}, \qquad C_f = \frac{3}{4}\left(\frac{C_D}{d_b}\right)(|v_z - u_z|)$$

see Myong and Kasagi 1990, the rest of the model coefficient are the same as specified by Wilcox 2006. The 1D model accounting for continuous turbulence was implemented and successfully applied to air-water and air-ethanol solution by Vitankar et al. 2002. The present 3D is still under evaluation.

2.2 The LES two-phase flow model

The shortcoming of the RANS approach to model gas-liquid dispersed flows has shifted the interest to extend the scale-resolving turbulence simulation by including the LES models (Milelli et al., 2001; Lakehal, 2002; Lakehal, 2018). These models resolve directly the interaction of the large-scale anisotropic motions with bubbles, whereas the less energetic smallest motions including the interaction of the bubbles with the surrounding turbulence are represented in terms of sub-grid scale closure models, see Fig. 2.1.

The derivation of Euler-Euler filtered two-fluid equations in the LES framework can be found in the paper of Lakehal et al. 2002. In fact, we start from the multi-fluid equations multiplied by the phase indicator function and applying a filter process results in multi-fluid equations similar to the phase-averaged equations (1) and (2). The effective viscosity of the liquid phase is obtained through the summation of the molecular viscosity, the shear-induced turbulent viscosity, and the bubble-induced turbulent viscosity and is formulated in the present study using two models: (a) the

Smagorinsky model proposed by Zhang et al. (2006), (b) and the one-equation sub-grid-scale model proposed by Niceno et al. (2008). The details of those models are presented in section 4.
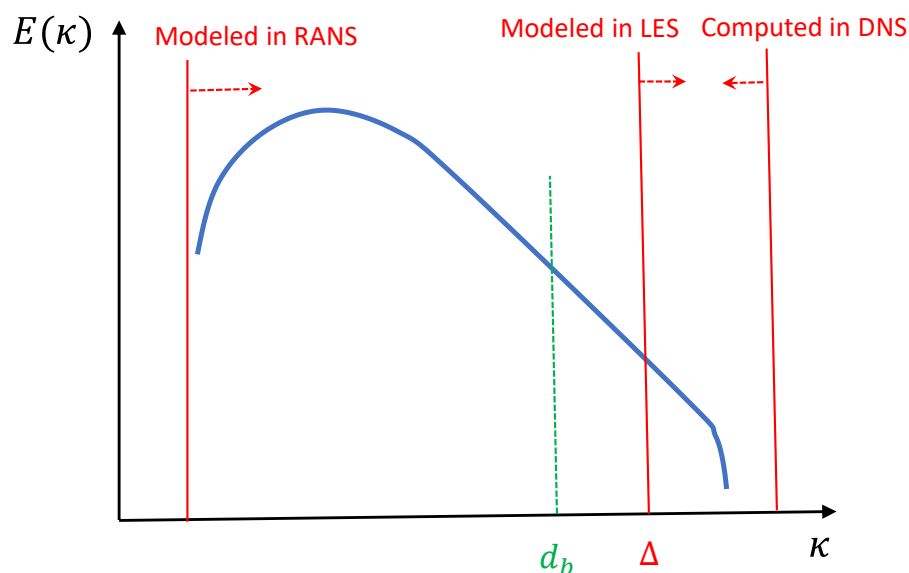
Fig. 2.1- Illustration of energy spectra of different modeling approaches.

For the present Euler-Euler LES approach, we have to consider the resolution requirement of both LES and the Euler-Euler approach simultaneously in order to choose a satisfactory grid. For the Euler-Euler model, the cell size should be larger enough than the largest interphase details of dispersed phase. In LES, the mesh has to be fine to resolve as much of the flow field as possible. According to Dhotre et al. 2013 and Zhang et al. 2008, a successful LES must have a filter width in the initial subrange region, and all scales of motion larger than that must be resolved on the numerical grid. They indicated that the bubble diameter must be smaller than the cell size. Milelli et al. 2001 reported a systematic posterior analysis of the ratio of the bubble diameter to cut-off filter size: $\Delta/d_B \geq 1.5$, that is the mesh size must be at least 50% larger than the bubble diameter for Eulerian-Eulerian simulations. We refer the reader to section 4 and Fig. 2.1.

The interfacial momentum exchange terms $\mathbf{M}_\varphi$ resulting from the phase averaging or filtering processes are highlighted in section 3 and 4

Chapter 3

Numerical simulation of hydrodynamics, flow regime transitions and mass transfer for a high aspect ratio bubble column

Numerical simulations of hydrodynamics, flow regime transitions and mass transfer were carried out in a 3D cylindrical bubble column reactor of high aspect ratio (H/D) of 20 with a multiple orifice gas distributor. A computational model based on the Euler-Euler two-phase flow model coupled with a $k - \varepsilon$ mixture turbulence model implemented in the Open-FOAM software package was validated with experimental data reported in Vial et al. 2002 and Gourich et al. 2008. The emphasis of this study is to assess the performance of this model and the analysis of the flow regime transitions and the transient flow behavior inside the bubble column reactor. All the non-drag forces (virtual mass, lift, turbulent dispersion) and drag force were incorporated in the model. A relatively the novel aspect of the present analysis is to quantify these forces and compare their magnitudes at different parts of the reactor. Different models of the overall mass transfer coefficient estimation, namely the slip penetration model and the eddy cell model, are compared against experimental data reported in Gourich at al. 2008 to verify these models and analyze the mass transfer. The results reveal some of the characteristic features of homogeneous and heterogeneous flow regimes on the liquid circulation, gas holdup, turbulent fluctuations and gas-liquid mass transfer. The flow field is characterized by different structures near the sparger corresponding to two transition flow regimes and several large scale vortical structures and circulation patterns along the column. The numerical simulations indicate that finer grid resolution was possible only for high superficial gas velocities cases and depends on the bubble diameter and refinements in the near wall region. The best agreement with experimental data were obtained by the inclusion of the turbulent dispersion force. Its relative magnitude as compared with other forces were smaller and is more pronounced near the wall. By comparing the predicted overall mass transfer coefficient, $K_L a_L$, with experimental data

20

for superficial gas velocities spanning both homogeneous and heterogeneous regimes, it is concluded that the mass transfer agrees only with the perfectly mixed liquid phase model using transient hydrodynamic effects.

3.1 Introduction

Bubble columns are widely used as gas-liquid and gas-liquid-solid reactors in many chemical, biotechnological and pharmaceutical industries due to their advantageous characteristics which they offer over other kind of multiphase bioreactors, especially stirred tanks, due to simple construction and operation, effective mixing and mass transfer between different phases. These reactors often consist of a simple cylindrical tube with a larger section at the top to promote the gas disengagement. The gas phase is dispersed in the form of tiny bubbles in a continuous liquid phase using a gas distribution device. Consequently, the flow pattern depends on many operating conditions such as the geometry, the gas distribution sparger that controls how the gas is spatially distributed and determines the primary bubble size distribution, and the gas flow rate that governs the flow regime. Furthermore, the complex interplay between operating conditions, the gas-liquid interfacial area, bubble size, bubble rise velocity, and bubble-bubble interactions lead to extensive range of flow regimes and complex flow structures. These make both computational modelling and experiments quite difficult and challenging, see Vial and Stiriba, 2013 and references therein.

Computational fluid dynamics (CFD) modelling of multiphase flow has been widely used as a cost-effective tool to predict the behavior of this type of reactor and simulate the flow pattern, local hydrodynamics and investigate the influence of design or other operating conditions. However, modelling and simulations results are considerably dependent on adopted closure models required for the interphase forces and bubble-induced turbulence. Interphase forces are modelled through the combination of the drag, lift, added mass and turbulence dispersion forces. Reviews of empirical correlations for interfacial forces on dispersed bubbles can be found in (Mudde and Simonin 1999;

Deen et al. 2001; Pfleger et al. 2001; Joshi 2001; Buwa et al. 2002; Sokolichin et al. 2004; Jakobsen 2001; Jakobsen et al. 2005; Kulkarani et al. 2007; Tabib et al. 2008; Simonnet et al. 2008; Selma et al. 2010; Bai et al. 2011; Masood and Delgado 2014). Therefore, to understand the effect of different interphase forces, many authors separated the various forces as far as possible to analyze the effects of each force on the flow pattern and validation models. The present study focus–on quantifying interfacial forces by calculating the instantaneous and time-averaged magnitude in different parts of the reactor with special emphasis on the turbulent dispersion force. Such numerical calculations would help to compare different interfacial forces locally and how much effect it has on the flow profile.

Besides the interfacial momentum transfer, turbulence modelling is one of the unresolved questions in the simulation of multiphase flows in bubble columns. Different turbulence models have been reported and evaluated. For instance, the zero equation turbulence models have been used by Pan et al. 1999, the $k - \varepsilon$ models in (Becker et al. 1994; Pfleger and Becker 1999; Sokolichin et al. 1999; Behzadi et al. 2004; Tabib et al. 2008; Laborde-Boutet et al. 2009; Selma et al. 2010; Masood and Delgado 2014; Stiriba et al. 2017), the Reynolds stress model (Le Moullec et al. 2008), and sub-grid scale models by Zhang et al. 2006 and Deen et al. 2001. The standard $k - \varepsilon$ model has been the most widely employed in the literature and at the moment there is no clear justification nor rules to prefer one model over another. However, very few studies have investigated the performance of the $k - \varepsilon$ mixture model (Behzadi et al. 2004) for bubble columns. This turbulence models are suitable for computation of the mixture and reduces to the equivalent single-phase model when only one of the phases is present. The present work performs such an analysis, wherein the mixture $k - \varepsilon$ model formulation implemented in the Eulerian two-phase solver twoPhaseEulerFoam along with the bubble induced turbulence and turbulence dispersion forces is qualitatively assessed through simulations of air-water flow experimental data of Vial et al. 2002 and Gourich et al. 2006. All the non-drag forces (virtual mass, lift, turbulent dispersion)

and drag force were incorporated in the model. Their effects separately have been analyzed and compared with experimental data.

Uniformly aerated bubble columns are characterized by the occurrence of different flow regimes which consist of the homogeneous (bubbly flow), the transition and heterogeneous (churn-turbulent) regimes. Identification of those flow regimes and their transitions as well as the description of prevailing flow structures strongly influence the hydrodynamic parameters, phase mixing, and mass transfer. Numerous studies have been proposed to study the flow structures and regimes transitions using different operating conditions and bubble column reactors (Mudde and Simonin 1999, Sokolchin et al. 1997, Soklinchin and Einberger 1999, Deen et al. 2001, Vial et al. 2001, Olmos et al. 2003a, Darmana et al. 2009). The aim of this work is to simulate the flow regimes transition for a high ratio cylindrical bubble column with a multiple orifice nozzle as an efficient gas distributor for uniform aeration. We present 3D transient flow simulations to validate the predicated local and global gas holdup, local liquid velocity against experimental measurements of Vial et al. 2001 and Gourich et al. 2006. Indeed, the statistical (averaged and fluctuations) quantities are compared with LDA and PIV measurement data and the flow regimes and transition points are validated with experimental data based on wall pressure fluctuations. We give a comparison with previous 2D works reported by Olmos et al. 2001 and Olmos et al. 2003a based on population balance and two-fluid models for the same reactor.

Mass transfer from the dispersed gas phase and the continuous liquid phase or vice versa is one of the most important and decisive factors in the design and scale-up of bubble columns. Generally, the mass transfer rate of the reactor is governed mainly by the volumetric mass transfer coefficient $K_L a_L$ in order to give a better understanding of the mass transfer phenomena. Its accurate prediction remains difficult due to experimental measurement methods such as the probe position or assumptions on hydrodynamic model (see Gourich et al. 2008) and also strongly depends on the sparger and reactor geometry, physical properties of the gas and liquid phases, and operating conditions. Gourich et al. 2008 gave a comparison between different models and showed the

23

sensitivity of $K_L a_L$ to those assumptions. Numerically, various mass transfer models have been developed and used for testing and accurate prediction (Van Batten and Krishna 2004; Dhanasekharan et al. 2005, Talvy et al. 2007, Fayolle et al. 2007, Wang et al. 2007, Huang et al. 2010, McClure et al. 2015). Careful analysis must be carried out in formulating and comparing between different CFD mass transfer models of $K_L a_L$ and experimental data since experimental estimation is tricky and may be sensible to the probe position in the bubble column, the sensor response time and hydrodynamic conditions. To the best of our knowledge, no computational work has been analyzed for predicting $K_L a_L$ against different experimental estimations. Therefore, we use the present CFD model to estimate $K_L a_L$ for different superficial gas velocities. The present study of the mass transfer specifically focuses on comparison of different mass transfer models to different estimations based on the gassing-in and gassing-out method, including the influence of the mixing phase conditions and oxygen sensor dynamics.

In a first step, details of the numerical procedure and twoPhaseEulerFoam (Open-FOAM two-fluid solver) using the mixture $k - \varepsilon$ turbulence model are described. Subsequently, we present the simulation results for superficial gas velocities U_G ranging from 1.4 to 8.4 cm/s and specifically focusing on quantifying the turbulent dispersion force compare to other forces, local flow characteristics such as turbulence, and the detailed regime map covering the three flow regimes. Finally, we analyze the volumetric mass transfer coefficient based on different mass transfer models.

3.2 Two fluid model and numerical setup

3.2.1 The governing equations of gas-liquid flow

The two-fluid model used for the simulations is based on the conditionally averaging of the conservation equations of mass and momentum, where both phases, the continuous liquid phase and the dispersed gas phases, are modelled as two interpenetrating continua. The present

24

formulation closely follows the procedure outlined by Weller 2005, where the conservation equations are averaged, along with the volumetric momentum exchange terms. The continuity equation mass and momentum equations for the phase φ are given by

$$\frac{\partial(\rho_\varphi \alpha_\varphi)}{\partial t} + \nabla \cdot (\rho_\varphi \alpha_\varphi \mathbf{U}_\varphi) = 0 \tag{1}$$

$$\frac{\partial(\rho_\varphi \alpha_\varphi \mathbf{U}_\varphi)}{\partial t} + \nabla \cdot (\rho_\varphi \alpha_\varphi \mathbf{U}_\varphi \mathbf{U}_\varphi) = -\alpha_\varphi \nabla p_\varphi + \alpha_\varphi \rho_\varphi \mathbf{g} - \nabla \cdot (\alpha_\varphi \rho_\varphi \boldsymbol{\tau}_\varphi^{\text{eff}}) + \mathbf{M}_\varphi \tag{2}$$

Here ρ_φ is the density, α_φ is the phase fraction, $\mathbf{U}_\varphi$ is the phase velocity vector, and $\tau_\varphi^{\text{eff}}$ represents the effective stress tensor usually decomposed into a mean viscous stress and turbulent stress tensor for the phase φ as

$$\boldsymbol{\tau}_\varphi^{\text{eff}} = -\nu_\varphi^{\text{eff}} \left[\nabla \mathbf{U}_\varphi + (\nabla \mathbf{U}_\varphi)^T - \frac{2}{3} (\nabla \cdot \mathbf{U}_\varphi) \mathbf{I} \right] + \frac{2}{3} k_\varphi \mathbf{I} \tag{3}$$

where k_φ is the turbulent kinetic energy of phase φ and I is the identity tensor. In Eq. (2), $\mathbf{M}_\varphi$ represents the inter-phase momentum exchange between phase φ and the other phase due to various interfacial forces. The present work is concerned with the effect of the drag, lift, virtual mass and turbulent drag which accounts for additional drag due to the fluctuations in the dispersed phase

$$\mathbf{M}_\varphi = \mathbf{M}_\varphi^D + \mathbf{M}_\varphi^L + \mathbf{M}_\varphi^{VM} + \mathbf{M}_\varphi^{TD} \tag{4}$$

Closures are required to model these forces and are extensively reported in many papers, see for instance the works of Jakobsen et al. 1997 and Joshi 2001 for a complete description. The drag force is formulated as

$$\mathbf{M}_\varphi^D = \frac{3}{4}\alpha_\varphi \rho_L \frac{C_D}{d_b} |\mathbf{U}_r|\mathbf{U}_r \tag{5}$$

with d_b is the bubble size and C_D is the drag coefficient which calculated based on the bubble

Reynolds number, $Re_b = \frac{\rho_L|\mathbf{U}_r|d_B}{\mu_L}$, and the relative velocity $\mathbf{U}_r = \mathbf{U}_G - \mathbf{U}_L$, according to the

Schiller-Naumann correlation

$$C_D = \begin{cases} \dfrac{24}{Re_b}\left(1 + 0.15Re_b^{0.687}\right), & Re_b \leq 1000 \\ 0.44, & Re_b > 1000 \end{cases} \tag{6}$$

The virtual mass force is modelled as

$$\mathbf{M}_\varphi^{VM} = \alpha_\varphi \rho_L C_{VM}\left(\frac{D\mathbf{U}_c}{Dt} - \frac{D\mathbf{U}_d}{Dt}\right) \tag{7}$$

which limits bubbles acceleration near the sparger to a physical value, see Simonnet et al. 2008. Most works adopted a constant virtual mass coefficient $C_{VM} = 0.5$.

The lift force is a lateral force with different mechanisms (Magnus, Saffman), see Jacobsen et al. 1997. It is represented by

$$\mathbf{M}_\varphi^L = \alpha_\varphi \rho_L C_L \mathbf{U}_r \times (\nabla \times \mathbf{U}_r) \tag{8}$$

where C_L is the non-dimensional lift force coefficient.

The turbulent dispersion force is accounted for the turbulent dispersed phase in the continuous phase. It is derived by Fave-averaging the multiphase Navier-Stokes equations, see Lopez and Bertonado 1998, as

26

$$\mathbf{M}_\varphi^{TD} = -C_{TD}\rho_L k_L \nabla\alpha_G \tag{9}$$

where C_{TD} is a constant and k_L is the kinetic turbulent energy in the liquid phase. There is still no agreement in the community on the closures or combinations to be used at best. We emphasis part of this work on testing different combination and quantification both instantaneous and time-averaged magnitude of each force in different part of the reactor.

The $k - \varepsilon$ mixture model (Behzadi et al. 2004) is adopted to model the turbulence and compute the shear induced dynamic viscosity. The model has shown improvement in the prediction of two-phase flows over other models considering only the turbulent kinetic energy on the continuous phase. We solve two phase-averaged transport equations for the mixture kinetic energy (k_m) and turbulent dissipation rate for mixture (ε_m)

$$\frac{\partial}{\partial t}(\rho_m k_m) + \nabla\cdot(\rho_m k_m \mathbf{U}_m) = \nabla\cdot\left(\frac{\mu_m^t}{\sigma_k}\nabla k_m\right) + P_{k,m} - \rho_m\varepsilon_m + S_{k,m} \tag{10}$$

$$\begin{aligned}
\frac{\partial}{\partial t}(\rho_m\varepsilon_m) &+ \nabla\cdot(\rho_m\varepsilon_m\mathbf{U}_m) \\
&= \nabla\cdot\left(\frac{\mu_m^t}{\sigma_\varepsilon}\nabla\varepsilon_m\right) + \frac{\varepsilon_m}{k_m}\left(C_{\varepsilon1}P_{k,m} - C_{\varepsilon2}\rho_m\varepsilon_m\right) + C_{\varepsilon3}\frac{k_m}{\varepsilon_m}S_{k,m}
\end{aligned} \tag{11}$$

where the mixture turbulent quantities are related to those of individual phases through the turbulent response coefficient C_t, which is defined as the ratio of the *r.m.s.* values of the gas velocity fluctuations to those of the liquid phase

$$C_t = \frac{U_G'}{U_L'} \tag{12}$$

and was modified to account for the influence for the gas volume fraction as in Rusche 2002. The rest of the mixture quantities appearing in the above transport equations are defined by mass-weighted averaging as

$$\rho_m = \alpha_L \rho_L + \alpha_G \rho_G, \quad \mathbf{U}_m = \frac{\alpha_L \rho_L \mathbf{U}_L + \alpha_G \rho_G \mathbf{U}_G C_t^2}{\alpha_L \rho_L + \alpha_G \rho_G C_t^2} \tag{13}$$

$$k_m = \left(\alpha_L \frac{\rho_L}{\rho_m} + \alpha_G \frac{\rho_G}{\rho_m} C_t^2\right) k_L, \qquad \varepsilon_m = \left(\alpha_L \frac{\rho_L}{\rho_m} + \alpha_G \frac{\rho_G}{\rho_m} C_t^2\right) \varepsilon_L \tag{14}$$

$$\mu_m^t = \rho_m C_\mu \frac{k_m^2}{\varepsilon_m} \tag{15}$$

The production of the kinetic energy of the mixture is related to both phases by

$$P_{k,m} = \alpha_L P_{k,L} + \alpha_G P_{k,G}, \quad P_{k,L} = \mu_k^t (\nabla \mathbf{U}_k + (\nabla \mathbf{U}_k)^T) : \nabla \mathbf{U}_k \tag{16}$$

The mixture $k - \varepsilon$ model constants have the same value as in the single-phase $k - \varepsilon$ model (Wilcox 2006). Details of the derivation of the model may be found in Behzadi et al. 2004 and Rusche 2002. The solution values are then used to calculate the turbulent kinetic energy for liquid (k_L) and turbulent dissipation rate energy for liquid (ε_L). Furthermore, the model accounts for the effect of the dispersed phase and the interfaces on the turbulence by adding a source term, $S_{k,m}$, expressed as the superposition of the shear-induced turbulent kinetic energy and the bubble-induced turbulence. The turbulent stress tensor in Eq. (3) is then computed at each iteration.

3.2.2 The mass-transfer model

The global mass transfer performance of the reactor is usually expressed in the term of the overall mass transfer coefficient, $K_L a_L$, which depends on many parameters including the gas hold-up, the bubble size distribution, the slip velocity and the turbulence energy dissipation rate. The

averaged transport equations of dissolved oxygen in the liquid phase are solved only when the oxygen concentrations are of interest and their source terms depend on $K_L a_L$. Many different models for estimating the mass transfer coefficient have been proposed. For instance, the laminar boundary layer model for the liquid side mass transfer coefficient is expressed as

$$K_L a_L = C \frac{6\alpha_G}{d_b \alpha_L} \sqrt{\frac{U_r}{d_b}} D_L^{2/3} v_L^{-1/6}$$

(17)

see Griffith et al. 1960. Here D_L is the molecular diffusivity of gas in liquid, and C is a constant that has been found experimentaly to vary from 0.4 to 0.95. This model can be applied to bubbles with rigid interface and have found to underestimate the mass transfer coefficient when it is applied to bubbly flows in an airlift reactor, see Huang et al. 2010.

Another model was proposed by Cockx et al. 2001 using the penetration theory of Higbie and leads to the following expression

$$K_L a_L = \frac{12\alpha_G}{d_b \alpha_L} \sqrt{\frac{D_L U_r}{\pi d_b}}$$

(18)

Here the interface area concentration is calculated based on the spherical bubble shape assumption

$$a = \frac{6\alpha_G}{d_b}$$

(19)

This model is based on the bubble diameter and the slip velocity. Based on the theory of Higbie and using the Kolmogorov theory of isotropic turbulence Lamon and Scott 1970 established the eddy cell model

$$K_L a_L = K \frac{12\alpha_G}{d_b \alpha_L} \left(\frac{D_L}{\pi}\right)^{1/2} \left(\frac{\varepsilon_L}{\nu_L}\right)^{1/4} \tag{20}$$

Here K is a model parameter. The cell eddy model assumed that the small scales of turbulent motion, which extend from smallest viscous motion to inertial ones, affects the mass transfer in the liquid. The model depends on the turbulent energy dissipation rate ε_L and is more appropriate for highly turbulent flow. There are many other mass transfer models available in the literature, see for instance the work of Huang et al. 2010 for a comprehensive literature survey and the published numerical studies proposed to analyze their performance. In this work, the three models described above will be tested against the experimental data of Gourich et al. 2008.

3.2.3 Numerical simulation set-up

The numerical simulations were carried out in a height to diameter ratio cylindrical bubble column (H/D) of 20 with uniform aeration using the open source CFD tool, Open-FOAM library (Weller et al. 1998). The averaged transport equations for mass and momentum for each phase as well as the turbulent kinetic energy and the dissipation rate transport equations for the mixture are solved by the two-phase flow solver twoPhaseEulerFoam implemented in Open-FOAM v.4.0.0. The solver is based on a finite volume formulation to discretize the model equations and has shown to be stable for transient calculations, see Weller 2005. The solving of the discretized transport equations proceeds iteratively in a sequential manner and starts by first predicting the gas and liquid phases by solving the continuity equation (1), we calculate the interfacial forces (4)-(9), we solve the momentum equations (2) to update all velocities in each phase, and then we employ the PIMPLE algorithm to solve the pressure-velocity coupling where the pressure equation is solved and the predicted velocities are corrected by the pressure change. Finally, the turbulence model equations (10) and (11) are solved and the same procedure is repeated for the next time step. The first-order bounded implicit Euler scheme is adopted for the time integration, the gradient terms

are discretized with a linear interpolation, the first-order upwind scheme for convective terms, and the diffusive terms are interpolated with the Gauss linear orthogonal scheme. The preconditioned conjugate gradient (PCG) is employed for solving the discretized pressure equation and the incomplete-Cholesky preconditioned bi-conjugate gradient (BICCG) is used for other set of linear equations. For a more detailed discussion of all steps mentioned above, see Rusche 2002, Selma et al. 2010, and Weller 2005.

The bubble column is the same as used by Vial et al. 2001, 2002 and Gourich et al. 2008 in their experiments. The height of the column is $H = 2$ m, the diameter is $D = 0.10$ m, and the static liquid height is 1.5 m. The reactor is operated with the water and air as the continuous and dispersed phases at room temperature and atmospheric pressure, respectively, and at a superficial gas velocity ranging from 1.4 to 8.4 cm/s. The gas is injected from the bottom of the column through a multiple orifice nozzle to ensure uniform aeration and study the flow regime transition. The initial and boundary conditions are summarized in Table 3.1. The gas distributor is treated as a uniform inlet mass flow rate calculated from superficial gas velocities for mass conservation with gas volume fraction of 1.0. The pressure at the inlet is set to zeroGradient and specified by the zero gradient boundary condition. At the outlet, the pressure is specified as atmospheric pressure, and the gas hold up is set to inletOutlet with zero gradient for outflow and fixed value for backward flow. The no-slip condition is applied at the walls for the velocities and Dirichlet condition for the gas hold-up.

Prior to the description of the computational mesh and presenting the results, we emphasis the implications of bubble size distribution on the model. In the present work, we assume a spherical bubble size distribution of 4 mm according to bubble size measurements of Vial et al. 2001. The same simplification was used by Khan et al. 2017 to simulate successfully their bubble column using $k - \varepsilon$, RSM, and Smagorinsky turbulence models at high superficial gas velocities. Perhaps the incorporation of bubble coalescence and break up in the present model may help in prediction of the flow field in the vortical-spiral regime. Note also that recently Huang et al. 2018 implemented

and used the variable bubble size models in modelling three-dimensional large diameter bubble columns operating under churn turbulent flow regime. They concluded that the model did not lead to any substantial improvement relative to the single size models and highlighted the need for improved breakup and coalescence closure descriptions.

The computational mesh was generated using the Gmsh finite element mesh generator. Fig. 3.2 illustrates the typical mesh structure used in the simulations. Hexahedral structured computational cells were employed, and the near wall was refined as we can see in the cross-sectional mesh. As pointed by Ma et al. 2015, the equations model is derived by volume averaging and the volume of each computational cell has to be substantially larger than the bubble diameter $(d_b/\Delta x \sim 1)$. In order to check that the computed results are grid-independent, different mesh refinements were tested with a superficial gas velocity 6 cm/s by increasing the number of computational cells in the axial direction and near the walls with a spatial resolution in the order of the bubble size. The simulation results of the time-averaged radial distribution of the gas holdup and axial liquid velocity are shown in Fig. 3.3(a) and (b). A grid number of 123700 on the domain with the minimum and maximum cell volume of $5 \times 5 \times 7 \, \text{mm}^3$ and $15 \times 15 \times 7 \, \text{mm}^3$, respectively, were employed in the rest of the simulations. The mesh is uniform in the axial direction and ensures good compromise between CPU time and accuracy at the column center and close near the walls. For low superficial gas velocities, the obtained results with this mesh resolution give non-physical oscillations and fail to capture the experimental data. Similar behavior was observed by Law et al. 2008 in their 2D simulations. Since the homogeneous flow regime is dominant, the coalescence and break up are not significant, suggesting a uniform grid size of nearly the bubble volume $\Delta x \times \Delta y \times \Delta z = 5 \times 5 \times 5 \, \text{mm}^3$. The resulting coarser mesh provides good resolution for low superficial gas velocities of $U_G = 1.4$ and 2.7 cm/s which closely fit the experimental data as we will see in the next section.

All transient calculations are started from static conditions with the liquid is at rest and the gas is injected with a mass flow rate corresponding to the experimental superficial gas velocity.

The bubble diameter is kept constant at 4 mm according to the experiments of Vial et al. 2001 (Fig.3.1).
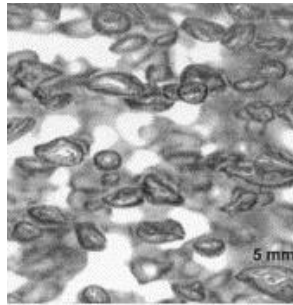
Fig 3.1 Photograph of bubbles in the bubble column reactor (Camarasa et al. 1999).

Bubble coalescence and breakup are not considered in this work. We start the calculations with a fixed small-time step of $\Delta t = 0.0005$ s for the first 20 s then we increase it to 0.001 s in order to account for the transient instabilities of bubbly turbulent flows. The flow was simulated for 200 s and before we start to collect statistics the solution has to been reasonably statistically stable. In Fig. 3.4 we plot time histories of the instantaneous and time-averaged gas holdup

$$\bar{\alpha}_G = \frac{1}{\tau} \int_t^{t+\tau} \alpha_G \, dt'$$

at the center of the reactor for $t = 50$ s, it is clear from these figures that after a lapse of 50 s fluctuations on the overall gas holdup are stabilized and by this time the influence of the initial field is negligible. Therefore, the averaged results from t = 50 s to t = 200 s are quantitively compared with experimental data. All the simulations were performed in a parallel mode on a PC cluster with 16 nodes, Intel Xeon, 2.8 GHz, 4GB RAM.

3.3 Results and discussions

The results obtained with the 3D two-phase CFD model will be presented and compared with experimental data. First, the hydrodynamics of the flow in terms of the local gas holdup and axial liquid velocity will be shown and compared with the predictions of some previous numerical

studies using the same reactor geometry and flow conditions. Subsequently, the flow structures based on the instantaneous data and averaged quantities are discussed and related to different flow regimes. We employ the model to compute global and local values of the mass transfer coefficient based upon the penetration and cell eddy models and compare them with the oxygen mass transfer experimental data.

3.3.1 Hydrodynamics and comparison with other simulations

Profiles of the radial distribution of axial liquid velocity and the gas holdup for different superficial gas velocities 1.4 - 8.4 cm/s are compared with experimental measurements at the mid-height of the column reactor and presented in Fig. 3.5, 3.6 and 3.7. In simulating the local gas holdup, all the cases are in very good agreement with the experimental data, whereas in predicting the local axial liquid velocity the present model provides reasonable accord with experiments for low $U_G \leq 4$ cm/s. For higher value of $U_G = 6$ and 8.4 cm/s, the model over predicts the measured values in the near-wall region by about 20-30% and 30-40%, respectively. This is probably due to small bubbles formed by the break-up phenomena which influence the hydrodynamic slightly in this range of superficial gas velocities and the fact that the $k - \varepsilon$ mixture model do not analyze the flow near the wall. A similar trend has already been observed numerically by Vial et al. 2001 using a 2D Euler-Euler simulations coupled with the population balance model for bubble size distribution and Olmos et al. 2001 using a 2D Euler-Euler based on a combination of a multi fluid approach and a population balance model for predominant bubble classes. Although the population balance or multi fluid models are expected to be more superior in this region, only the 3D time averaging transient predictions are in better agreement with the experimental data. Several simulation attempts were carried out to highlight the source of this numerical deviation. Some examples of this effort include the sensitivity of the model to grid resolution or interfacial forces as illustrated in Fig. 3.8 and will discussed later. Fig. 3.6 compares the averaged liquid velocity

over cross sectional area for different gas flow rates. In all cases the mixed $k - \varepsilon$ model shows good agreements with the experimental data.

Fig. 3.7 depicts the radial distribution of the local gas hold-up at the mid height of the bubble column. For all the inlet superficial gas velocities, once again, the 3D CFD model predicted local gas hold-up profiles are more close to the experiments as compared to other two-phase models. Although the profile was slightly under-predicted close near the wall for $U_G = 1.4$ cm/s due to the Neumann boundary condition and the coarser grid used. These findings are in accord with the results of Bhole et al. 2008 who observed low gas fraction near the wall with the MUSIG model. Although the local profile becomes parabolic for both high and low gas velocities, it is interesting to note that, for the purpose of comparison, the 2D two-phase flow based on a wide bubble size distribution give small amount of the gas near the wall and large bubbles with high velocities in the core region. For nearly the same inlet gas superficial velocity Besagni et al. 2017 observed a flat profile which overestimate their measurements using a multi fluid model. The contribution of the small bubbles traveling with the same velocity in those models increases the amount of the gas in the center and reduces the liquid circulation near the wall. The present mono modal model provides a stable diameter distribution ($d_B < d_S \approx 7.7$ mm) which essentially dominates the hydrodynamic in the core region. In the line of these results, the resultant dispersion forces including the drag and turbulent dispersion forces were sufficient to simulate the bubble migration toward the center of the column.

The simulations were carried out using several interfacial forces: drag, lift with different values of C_L (-0.5, 0.2, 0.5), virtual mass, and turbulence dispersion forces with different values of C_{TD} (0.2, 0.6, 0.8, 1.2). Fig. 3.8 compares the effect of different forces on the flow pattern at $U_G = 8.4$ cm/s. Here we show only the best profiles. In addition, the virtual mass force does not have any impact on the radial profiles as we move away from the distributor. When the lift force is added to the drag force the liquid profile shows an increase at the center and near the wall whereas the gas hold-up is under estimated. For D-VM or D-L-VM the profiles deviate largely from the experiments

in the core region where the gas holdup is relatively higher. The reason may come from the incomplete description of the coupling of two phases and the fact that the lift force causes an acceleration of the flow in the central region where the bubbles stay. The best results compared to experimental data were obtained with the drag force model of Schiller-Naumann and the turbulent dispersion of Lahey et al. (1993). The liquid flow is turbulent leading to intense fluctuations on the liquid phase which act on the bubbles and pushing them to the walls. The gas phase spreads more in the radial direction due to the higher turbulence diffusion. This indicates that the influence of the turbulence dispersion force could be much important than the lift force to move the higher size bubbles towards the column center and the small bubbles to the near wall.

To quantify the influence of the interfacial momentum forces, the magnitude of the instantaneous and time-averaged drag, virtual-mass and turbulent dispersion forces in bubble column are plotted and compared in Fig. 3.9. The instantaneous values are displayed at time 100 s. The drag force is dominant in the axial direction and at the center. The strength of the other interfacial forces appears small as compared to the drag force, but the virtual-mass have more influence near the sparger, meanwhile the turbulent dispersion force is more pronounced in the near wall region and seems to influence in the radial transverse direction.

From the above comparison with the experimental data, the following closure were identified and subsequently gets reflected in the predictions obtained for the different flow regimes and mass transfer in the bubble column reactor studied:

- 3D unsteady simulation with time averaging;
- high resolution in the axial direction and in the near wall region for $U_G \geq 3$ cm/s and nearly uniform mesh for $U_G < 3$ cm/s;
- the mixture $k - \varepsilon$ model;
- Schiller-Naumann correlation for the drag force;
- Lopez de Bortodano for the turbulence dispersion force with $C_{TD} = 0.8$;

36

- and neglect the lift force.

3.3.2 Instantaneous flow and regime transition

Besides the evaluation and validation of the flow field, the different flow regimes for the fully aerated column was analyzed. The variation of the global gas holdup with the superficial gas velocity are illustrated in Fig. 3.10 (a) against experimental measurement from the bottom to a sample located 1 m higher than the sparger. At lower ($U_G \leq 3.7$ cm/s) the overall gas holdup variation is linear and predicts well the homogeneous regime. At higher (3.7 cm/s $< U_G \leq 6$ cm/s) slightly lower $\langle \alpha_G \rangle$ values are obtained compared to experimental measurements and the transition regimes are numerically reproduced, while at higher ($U_G = 8.4$ cm/s) the deviation decreases and the stagnation of $\langle \alpha_G \rangle$ is predicted. Overall, the simulation and experiments are in good agreements with the same trend, and the homogenous and heterogeneous flow regimes are described quite well by the 3D CFD model and can be represented with a unique bubble size distribution as reported by Vial et al. 2001 and Olmos et al. 2003. The 3D CFD model based on mixed $k - \varepsilon$ model performs better than 2D model combined with population balance and two fluid models. Only at $U_G = 6$ cm/s the calculated global gas holdup deviates from experimental data. The reason of this deviation is probably the multiple orifice generates both higher and smaller bubble sizes, at the beginning of the transition to the heterogeneous regime, which may not be coalesced at intermediate inlet gas flow rates. To check this, we conducted part our simulations with smaller bubble diameter of $d_B = 2$ mm and we display simulation results in the same picture. Fig. 3.10 (a) shows that a narrow bubble size distribution would help to predict accurately the transition and heterogeneous flow regimes.

The averaged gas hold-up $\langle \alpha_G \rangle$ were measured between two wall sampling points located 0.5 and 1.5 m higher than the gas distributor, respectively, and compared with the mixture RANS model in Fig. 3.10(b). Simulation results with two bubble size distributions are shown. As expected,

a good agreement is obtained for low superficial gas velocities ($U_G \leq 4$ cm/s). In the transition and heterogeneous regimes, the CFD model performs much better and gives a linear trend with slower rate increase in the transition regime. This might be attributed to the inlet boundary conditions at the sparger modelled by a simple uniform inlet mass flow rate, where the bubbles are accelerated and traveling from the central part of the column to the near walls. It is clear that the flow regimes and transitions are a complex function of the kind of aeration, correct sparger modelling as well as the bubble size distribution.

To analyze more deeply the different flow regimes, we tracked the axial liquid velocity vectors at the central plane with respect to time and some key snapshots have been illustrated in Fig. 3.11. As can be seen, the flow field is not steady and is characterized by local liquid recirculation near the walls and different large-scale vortices at the core. Two vortices start to develop on both sides of the lower column corner in different ways. For low superficial gas velocity, the two vortices are developed in the near wall region and not in the center with an increase of local gas volume fraction. At high superficial gas velocity ($U_G = 6$ cm/s) a counter-rotating pair of vortices is observed at the column center near the distributor. All these flow structures were considered as hypothetical structures of the transition flow regimes T1 and T2 obtained by Olmos et al. 2003a by applying the wavelet transform to LDA signals. For high superficial gas velocity ($U_G = 8.4$ cm/s) the bubbles are rising at higher velocity in a uniform way filling the entire column diameter. As the gas is injected in the column, the liquid moves upward with a pronounced bubble plume structure started from the distributor zone up to the free surface. Several liquid circulation cells are then observed throughout the column height. The number of cells and their sizes are changed with the inlet superficial gas velocity. For instance, for ($U_G = 3.72$ cm/s) 2 to 3 cells outside the bubble plume fill the lower half part of the column, meantime the central part is more stable, and the bubble are uniformly distributed. These flow structure corresponds to the flow transition regime T1 where the flow becomes unstable and beyond some liquid height becomes homogeneous again. As we increase further the inlet superficial gas velocity ($U_G = 6$ cm/s), the

cells rise with high velocities along the column in a meandering way and the bubble plume reaches the wall column. At higher gas flow rate ($U_G = 8.4$ cm/s) the flow liquid becomes turbulence due to the bubble motion which becomes more dynamic and spiraling downward in the near wall region. These flow structures qualitatively agree with the experimental observations of Olmos et al. 2003a and characterize locally the transition T2 and heterogeneous regimes.

Fig. 3.12 shows instantaneous iso-surfaces of constant gas hold-up $\alpha_G = 0.2$ at time $T = 100$ s and different initial superficial gas velocities together with horizontal slices at different heights of the column. The iso-surfaces illustrate the spiral rotating movement of the bubble plume near the sparger with a more homogenous distribution from up to the center of the column for low U_G. For high U_G the bubble plume looks very similar to those observed in Lehr et al. 2002. The gas spreads spirally through the centerline of the column and exhibits a 3D oscillatory character with several vortices that extend over the half column diameter. This behavior shows the different characters of the flow regime T2 and the heterogeneous one obtained for fully aerated 3D bubble column. As highlighted by Olmos et al. 2003, in the heterogeneous regime the bubble plume is characterized by large bubbles which fill the entire column diameter. The instantaneous local gas holdup illustrates the typical flow patterns of the bubble column where large amount of the gas flow through the column core and small bubbles are dragged to the near wall region. However, for $U_G = 3.75$ cm/s significant gas volume fraction are predicted near the wall column for $H = 10$ cm. This is probably due to the vortices formed in the vicinity of the sparger typical for the transition regime T1, then the flow ascends in the core region.

3.3.3 Turbulence model

Fig. 3.13 shows the experimental and numerical radial profiles of the liquid velocity fluctuations in the axial direction (v_{rms}). The fluctuations are higher close to the wall column for low superficial gas velocities ($U_G \leq 6$ cm/s) and display a periodic trend for $U_G = 8.4$ cm/s. This

is due probably to the liquid movements from upward to downward at the center and close to the wall column. Furthermore, the averaged anisotropic velocity fluctuations of the liquid are not well predicted with the mixture $k - \varepsilon$ model with the bubble induced turbulence effects as source terms, especially for superficial gas velocities lower than 6 cm/s. For $U_G = 8.4$ cm/s, it slightly over estimates the axial fluctuations. The profiles show a slight increase near the wall followed by a smooth decrease toward the center. A likely cause for this slight increase is the existence of a large fraction of the gas and the fact that we neglect the bubble deformation due to their contact with the wall by the monodisperse model. The bubbles swarms accumulated at the center also cause high velocity fluctuations due mainly to the large bubbles. The present Euler-Euler mixture $k - \varepsilon$ model was able to predict the overall behavior of the profiles and shows better agreement with experiments as compared with other 2D model based on population balance and two-fluid models.

Unfortunately, experimental data on kinetic turbulent energy of the liquid phase are not available. In fact, Vial et al. 2001 only measured the *rms* in the axial and orthoradial directions. From the work of Franz et al. 1984, the turbulent kinetic energy can be estimated as

$$k_L = \frac{1}{2}\left(\overline{u_L'^2} + \overline{v_L'^2} + \overline{w_L'^2}\right) \approx \frac{1}{2}\left(2\frac{2}{3}\overline{v_L'^2} + \overline{v_L'^2}\right) \approx \frac{7}{6}\overline{v_L'^2}$$

The predictions of the liquid-phase kinetic energy profiles k_L are shown in Fig. 3.13 at the U_G values of 3.72, 6 and 8.4 cm/s. The simulated profiles are seen to be flatter and lower in magnitude as compared with the estimated turbulent kinetic energy. This poor representation can be attributed to the assumption of isotropic turbulence model which is not valid for turbulent flow in bubble column reactors. Similar behaviors were obtained by other authors, see for instance Tabib et al. 2008. The simulations give good prediction in churn-turbulence regime ($U_G = 8.4$ cm/s) and for all other cases the calculated *rms* has a maximum value around the cross-over point as experiments. Additional comparison was made between the sectional averaged axial velocity fluctuation of the liquid at the height $y/H = 0.8$ in Fig. 3.14. The numerical results underestimate

the measurements in homogeneous regime and overestimate them in the heterogeneous regimes and give nearly constant values and sharp increase at the incipient heterogeneous regime. This behavior is opposite to that of the mean axial liquid velocities which over estimate experiments, see Fig. 3.5 and 3.6. The turbulent intensities vary between 64% and 85 % in the bubbly and churn-turbulence regimes.

3.3.4 Mass transfer analysis

The volumetric mass transfer coefficient $K_L a_L$ were modelled based on different mass transfer models given by Eqs. (17)-(20) to test and better understand the gas-liquid mass transfer mechanisms in the present bubble column reactor. The overall volumetric mass transfer coefficient data measured by Gourich et al. 2008, using the dynamic gassing-in and gassing-out method and fitting the predicted oxygen concentration at the probe level, were used to validate the numerical simulations. The increase of oxygen concentration was measured until the water became saturated with dissolved oxygen. Assuming a well-mixed liquid phase, the mass balance of oxygen is given by the following equations

- In the bulk of the liquid phase

$$\frac{dC_L}{dt} = K_L a_L (C^* - C_L) \tag{21}$$

- Near the electrode

$$\frac{dC_P}{dt} = k_P (C_L - C_G) \tag{22}$$

where C_L and C_G are the oxygen concentration in the liquid and gas phases, respectively, C_P is the dissolved oxygen concentration in the batch liquid phase, C^* is the saturated given by Henry's law

$$C_G = mC^* \qquad \text{with} \quad m = \frac{He_{20}}{RT} \tag{23}$$

The tabulated Henry's constant at 20 ºC is $He_{20} = 10.16 \times 10^4$ Pa m³/mol. Integrating of Eqs. (21) and (22) with $C_L = C_P = 0$ at $t = 0$ gives

$$\frac{C_L}{C^*} = 1 - \frac{1}{k_P - K_L a_L}\left(k_P e^{-K_L a_L t} - K_L a_L e^{-k_P t}\right) \tag{24}$$

Gourich et al. 2008 analyzed the oxygen concentration curves and showed that cutting the oxygen response curve along with the assumption of perfectly mixed reactor must be avoided. The above model may be applied only after an integral time t_0.

We compare our numerical data with experimental measurements corresponding to two different models: perfectly mixed reactor with transient hydrodynamic effects (M2), and axial dispersion model for the liquid phase with plug flow model for gas phase (M4). Fig. 3.15 displays the predicted and measured overall volumetric transfer coefficient at different inlet superficial gas velocities. The models give reasonable predictions for the whole range of superficial gas velocities, though the slip penetration seems to do somewhat better than the eddy cell models with $K = 0.27$. Mass transfer coefficient computed with the laminar boundary layer model, not presented here, behaves poorly since the flow conditions don't satisfy the laminar boundary layer model assumptions. In the homogeneous regime ($U_G < 4$ cm/s), both experimental and numerical models increase linearly with increasing gas flow rate and gave nearly the same results. The penetration model agrees well with model M2, and the predicted values by cell eddy model under estimate both model data M2 and M4. This due probably to the fact that the mixture $k - \varepsilon$ model was used to estimate the turbulent dissipation rate even though the bubble induced turbulence has been considered as a source term. The predicted mass transfer coefficient K_L is nearly 0.000215 m/s. In the homogeneous and transition regimes, the CFD models under estimate the liquid velocity as we

have observed in Fig. 3.6, thus decreasing the liquid circulations has a tendency to slow down the bubble in the core region which reduces the residence time and therefore the gas holdup and mass transfer coefficient.

Fig. 3.16 shows the evolution of instantaneous and time averaged values of $K_L a_L$ at different cross sections along the height of the column reactor obtained by the penetration model for $U_G = 8.4$ cm/s. We note that the local time averaged volumetric mass transfer coefficient spreads from the center to the near wall. The instantaneous results show a non-uniform radial distribution of the mass transfer with an increase of $K_L a_L$ at the top center of the column where most of the gas is located. This variation is in accordance with the radial fraction distribution displayed in Fig. 3.8. The mixture two-flow model based on the penetration model predicts well the $K_L a_L$ measurements from the dynamic gassing-in and gassing-out method assuming both perfectly mixed liquid phase or axial dispersion.

3.4 Conclusions

CFD simulations of gas-liquid flow in the 3D cylindrical bubble column of high aspect ratio with a multiple orifice nozzle have been performed to study air-water system based on Open-FOAM software package. A Euler-Euler two-phase flow model with a mixture $k - \varepsilon$ turbulence model has been used to compute the global and local gas hold-up, axial mean and *rms* liquid velocity fluctuations values and validate with experimental data of Vial et al. 2001 and Gourich et al. 2006. Different models of mass transfer coefficient, namely the slip penetration model and the eddy cell model, were tested and evaluated against the experimental measurements by Gourich et al. 2008. After identifying appropriate interfacial force closures and correlations for the CFD model, it was used further to examine the effects of the uniformity of the gas aeration, turbulent dispersion forces, and bubble-induced turbulence on the liquid circulation and turbulence inside the reactor. Main conclusions from the present work are as follows:

- A computational two-phase flow CFD model was identified to predict successfully 3D unsteady air-water flow in a high aspect ratio cylindrical bubble column. The model uses the mixture $k - \varepsilon$ model with bubble induced turbulence, the Schiller-Naumann correlation for the drag force, and Lopez de Bortodano for the turbulence with $C_{TD} = 0.8$ dispersion force, while neglects the lift force.

- The results show that finer grid resolution was possible only for high superficial gas velocities cases ($U_G > 2.6$ cm/s) and are dependent on the bubble diameter in the center and mesh refinements in the near wall region.

- The CFD model was more successful in calculating the local gas holdup, the axial velocity profile for the liquid and the *rms* of their fluctuations, and the global gas holdup in comparison to 2D calculations based on other models and shown good agreements with the experiments. However, it over predicts the liquid recirculation in the near wall regions.

- The calculated flow fields are characterized by different structures near the sparger corresponding to different transition flow regimes T_1 and T_2 with different pair vortices and several large flow structures along the column.

- The predicted overall mass transfer coefficient $K_L a_L$ agrees well with experimental measurements from the dynamic gassing-in and gassing-out method assuming both perfectly mixed liquid phase or axial dispersion for both homogeneous and heterogeneous regimes, though the slip penetration seems to do somewhat better than the eddy cell models with $K = 0.27$.

The study indicated that the CFD model reasonably predicted the hydrodynamics, regime transitions and mass transfer in the bubble column reactor. Proper treatment for the wall region such as population balance, wall function and large eddy simulations are needed to better capture the liquid recirculation in such reactors.

	U_G	p	α_G	k	ε
Inlet	Inlet value	zeroGradient	1	fixedValue	fixedValue
Outlet	zeroGradient	fixedValue	inletOutlet	zeroGradient	zeroGradient
Walls	No slip	zeroGradient	fixedValue	Wall function	Wall function

Table 3.1 Boundary conditions for both phases

(a) (b)
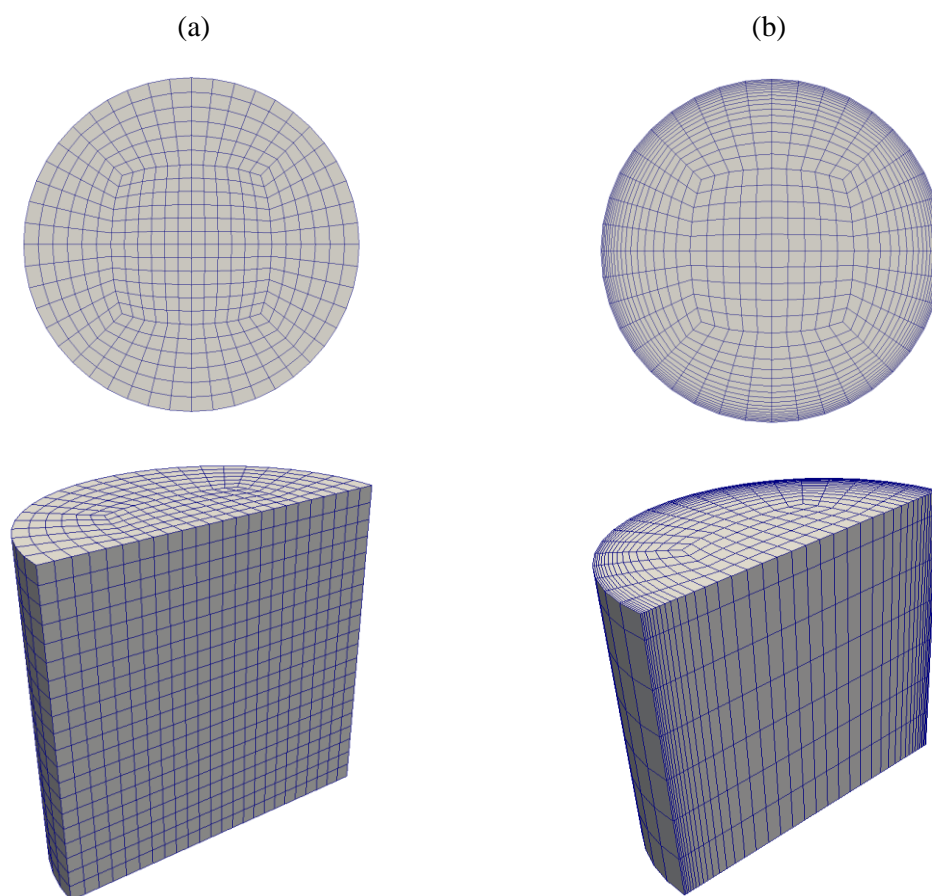
Fig 3.2 Typical mesh structure used in numerical simulation (a) for low U_G, and (b) for high U_G.

(a)

(b)
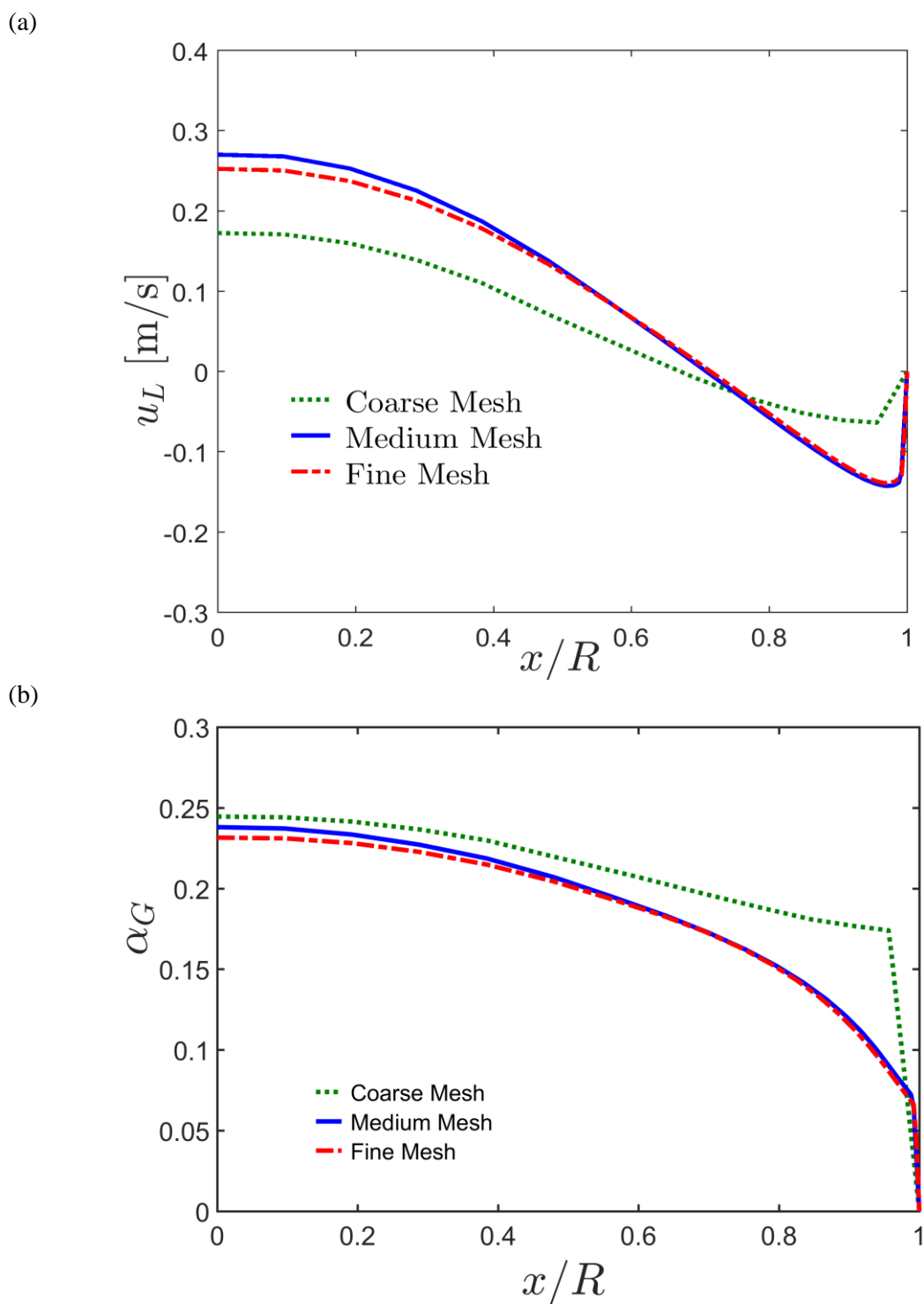
Fig 3.3 Radial profile of axial liquid velocity (a) and gas holdup (b) for different meshes.
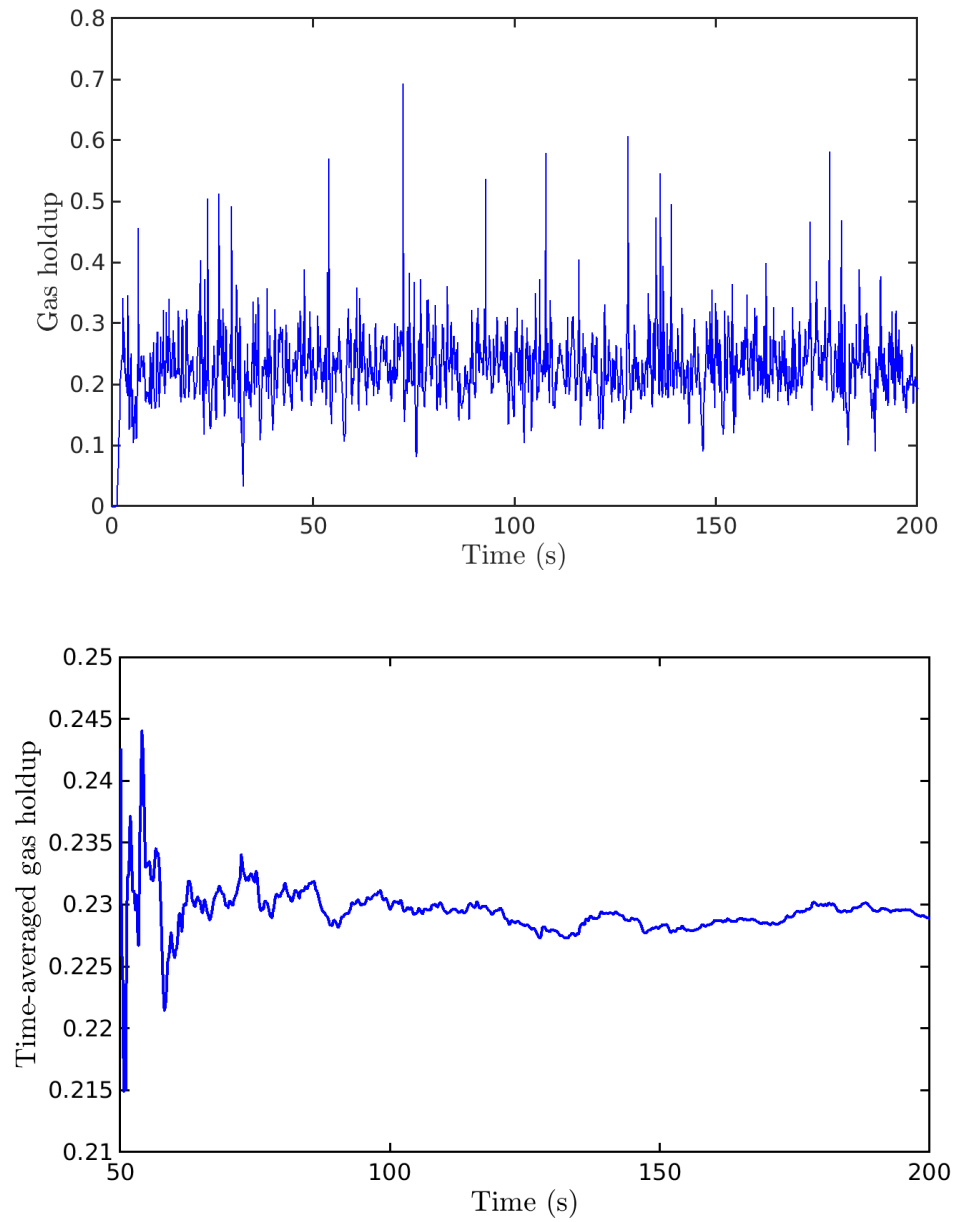
Fig 3.4 Time history of instantaneous gas holdup (top) and time-averaged gas holdup (bottom). The averaging is started at time 50 s.
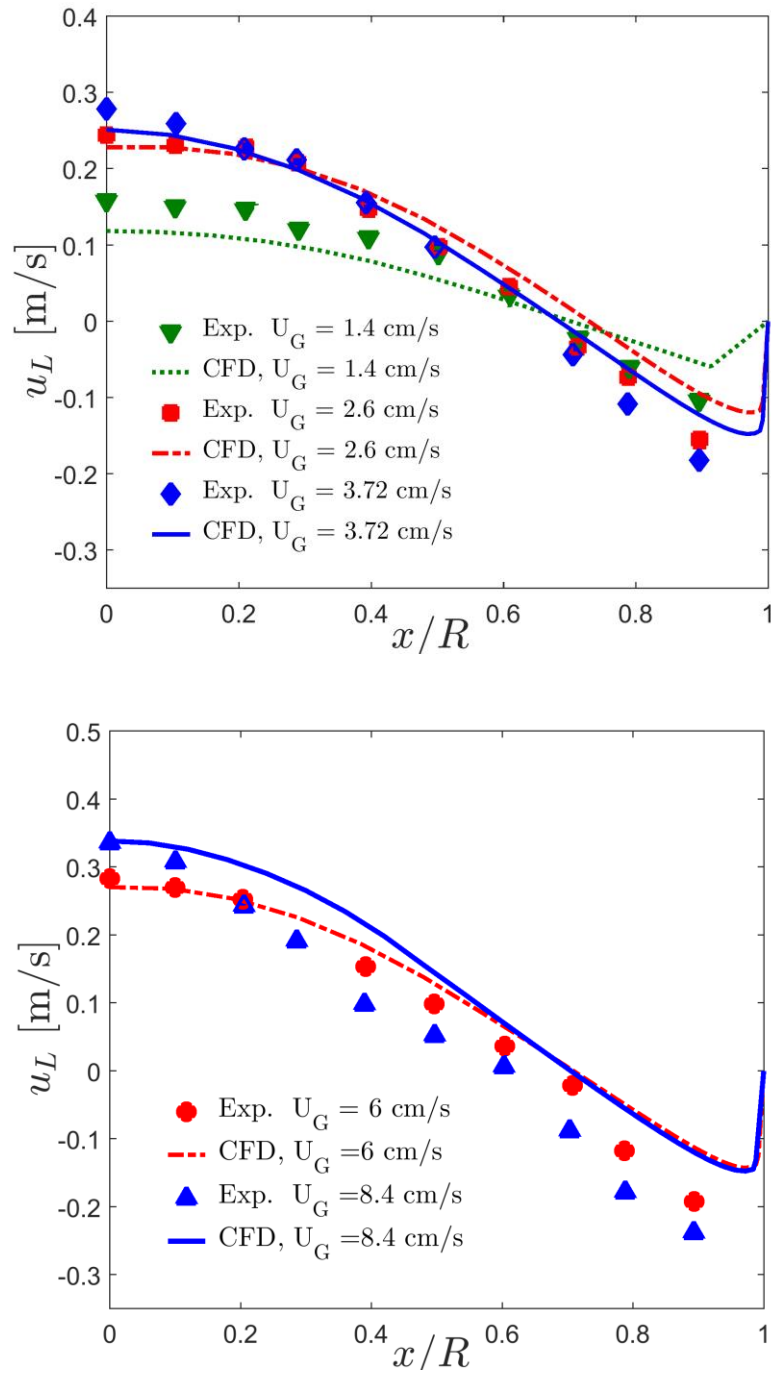
Fig 3.5 Comparison of superficial gas velocities obtained by the present 3D CFD calculations and experimental data.
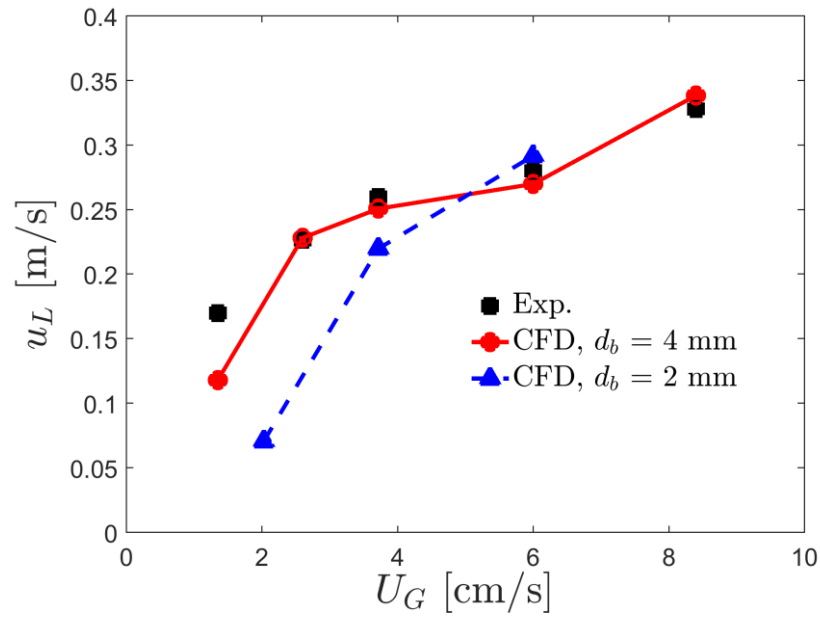
Fig 3.6 Comparison of the time averaged liquid centerline velocity at height of 0.7 m versus superficial gas velocity.
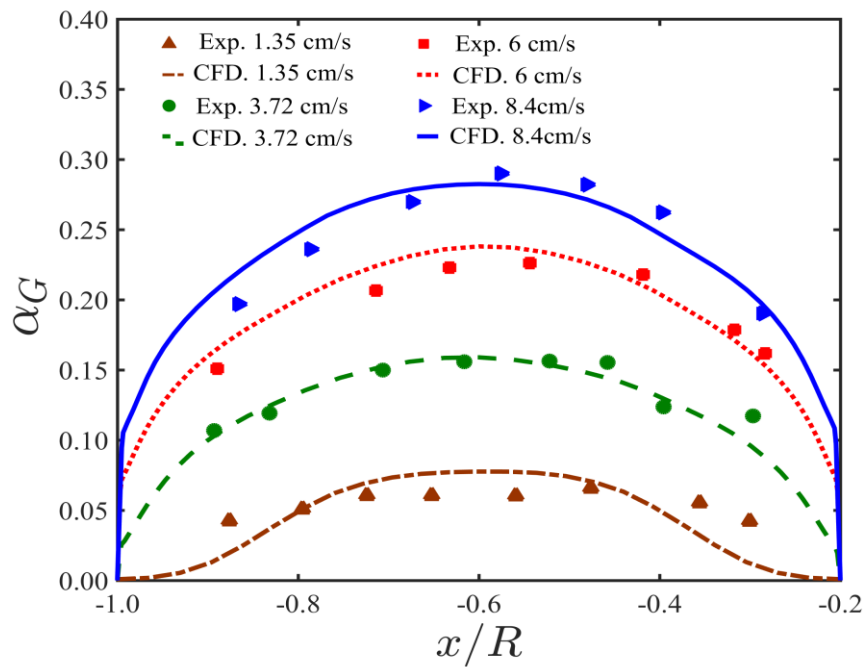
Fig 3.7 Comparison of the local gas holdup for simulations compare to experimental data.
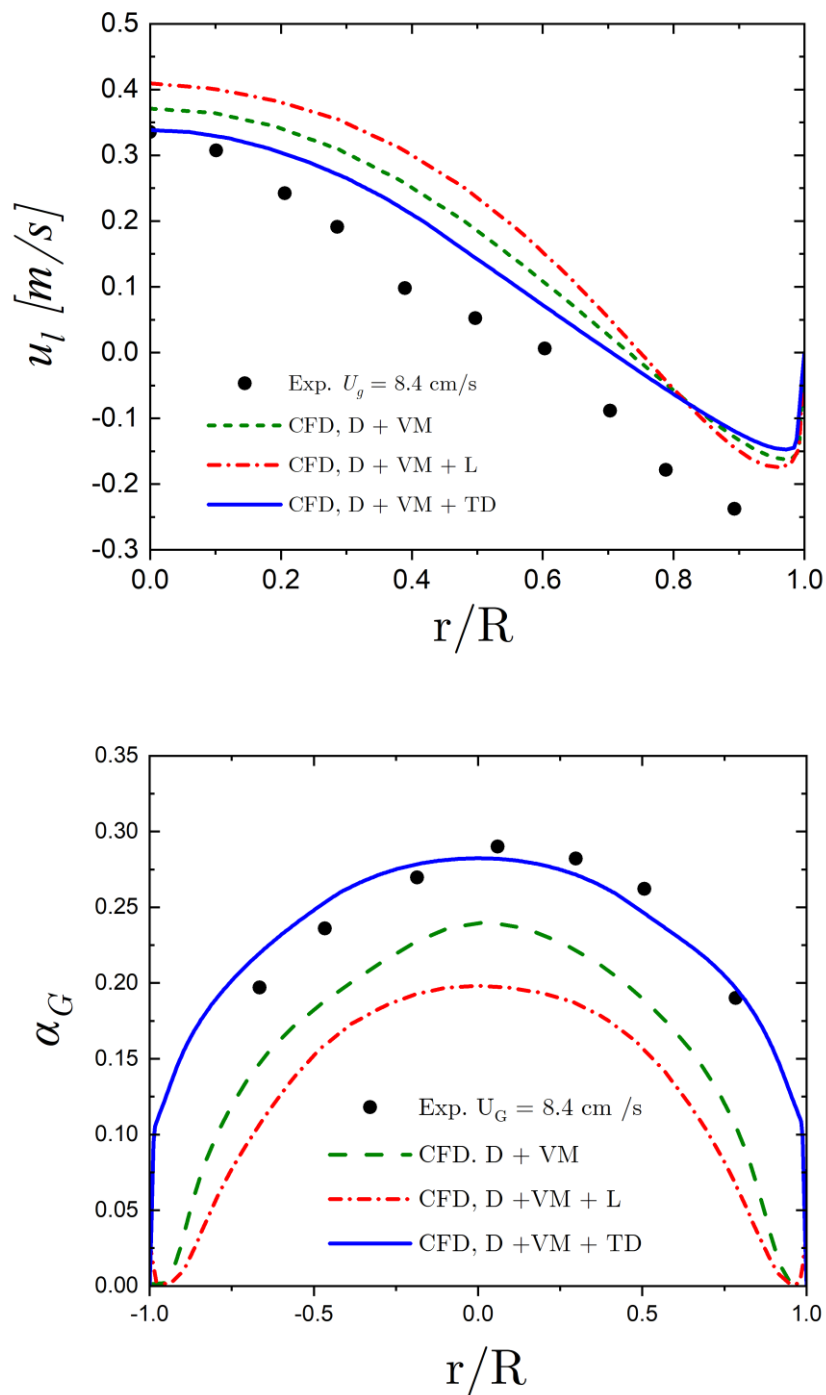
Fig 3.8 Effect of interfacial forces on the liquid axial velocity and gas hold-up for $U_G = 8.4$ cm/s.
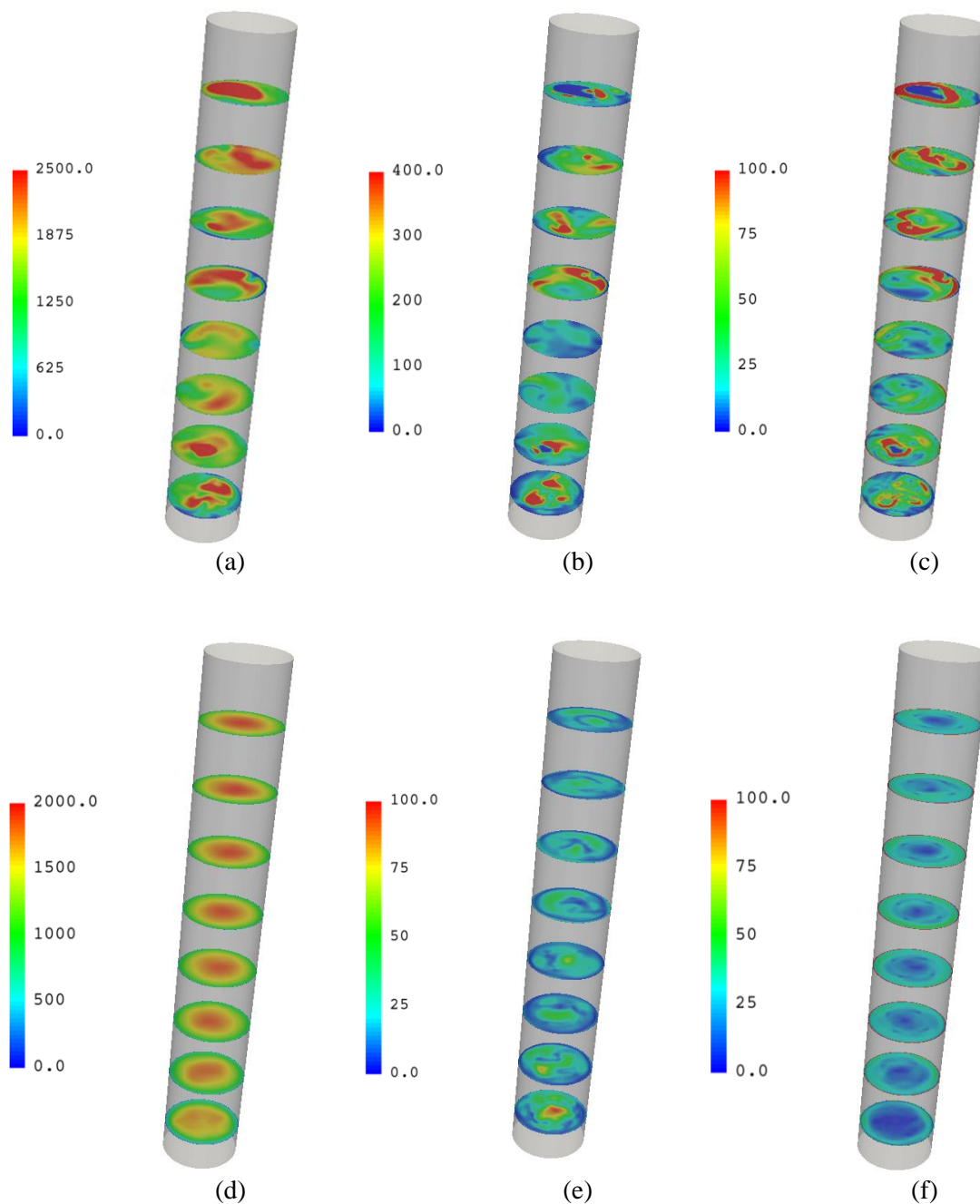
Fig 3.9 Quantification of interfacial forces at $U_G = 8.4$ cm/s: (a, d): drag force; (b, e): virtual mass force; (c, f): turbulent dispersion force; (top) instantaneous contours at 100 s simulation time; (bottom) time-averaged contours.

(a)

(b)
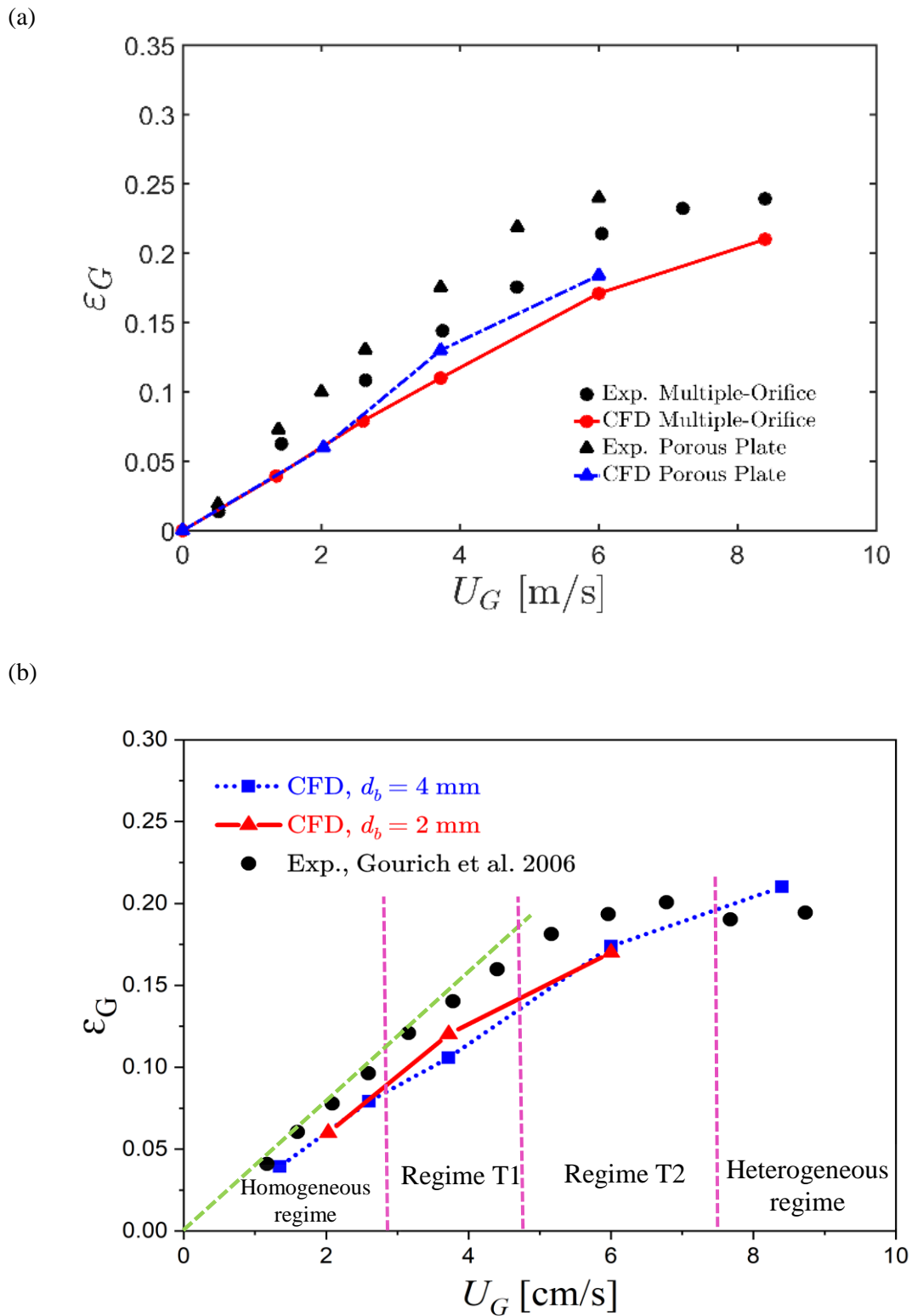
Fig 3.10 Comparison of the global gas holdup versus superficial gas velocity obtained by the present 3D CFD calculations and experimental data.
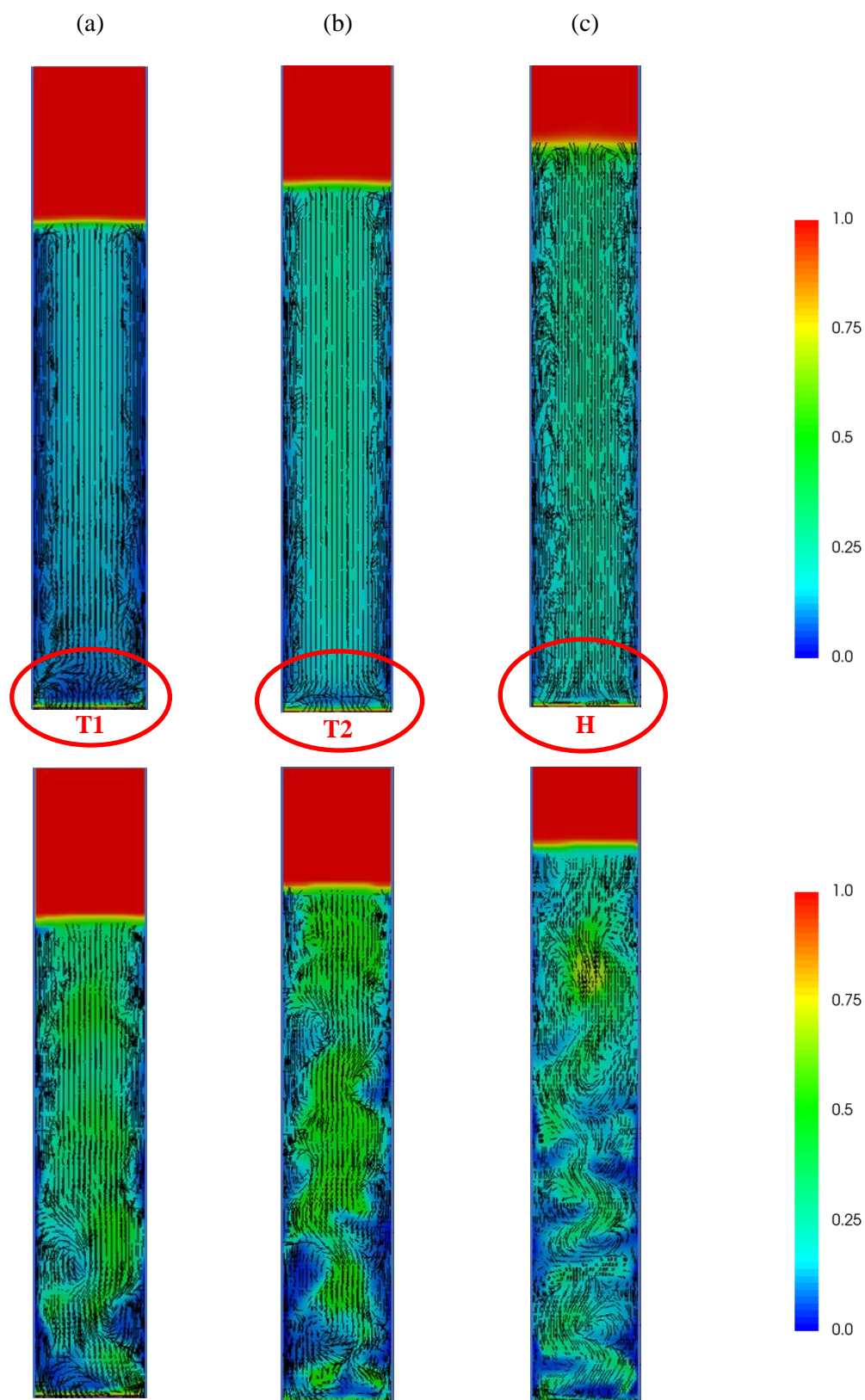
Fig 3.11 Snapshots of time averaged (top) and instantaneous (bottom) gas hold-up and liquid velocity field for (a) $U_G = 3.72$ cm/s, (b) $U_G = 6$ cm/s, and (c) $U_G = 8.4$ cm/s.
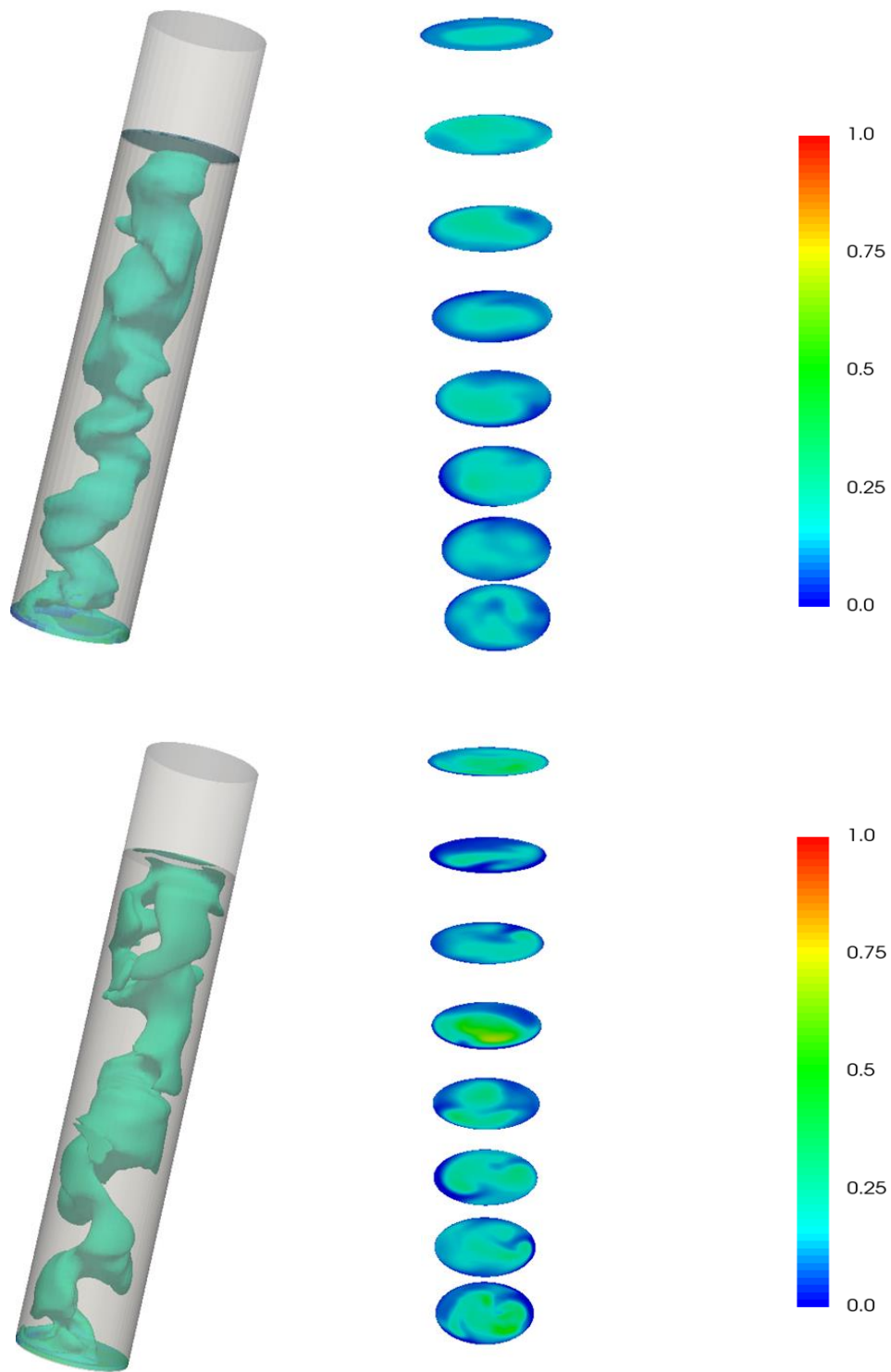
Fig 3.12 Iso-surface distribution of the gas holdup in the column at $t = 100$ s (left) and at different heights (right) for superficial gas velocity of 6 cm/s (top) and 8.4 cm/s (bottom).
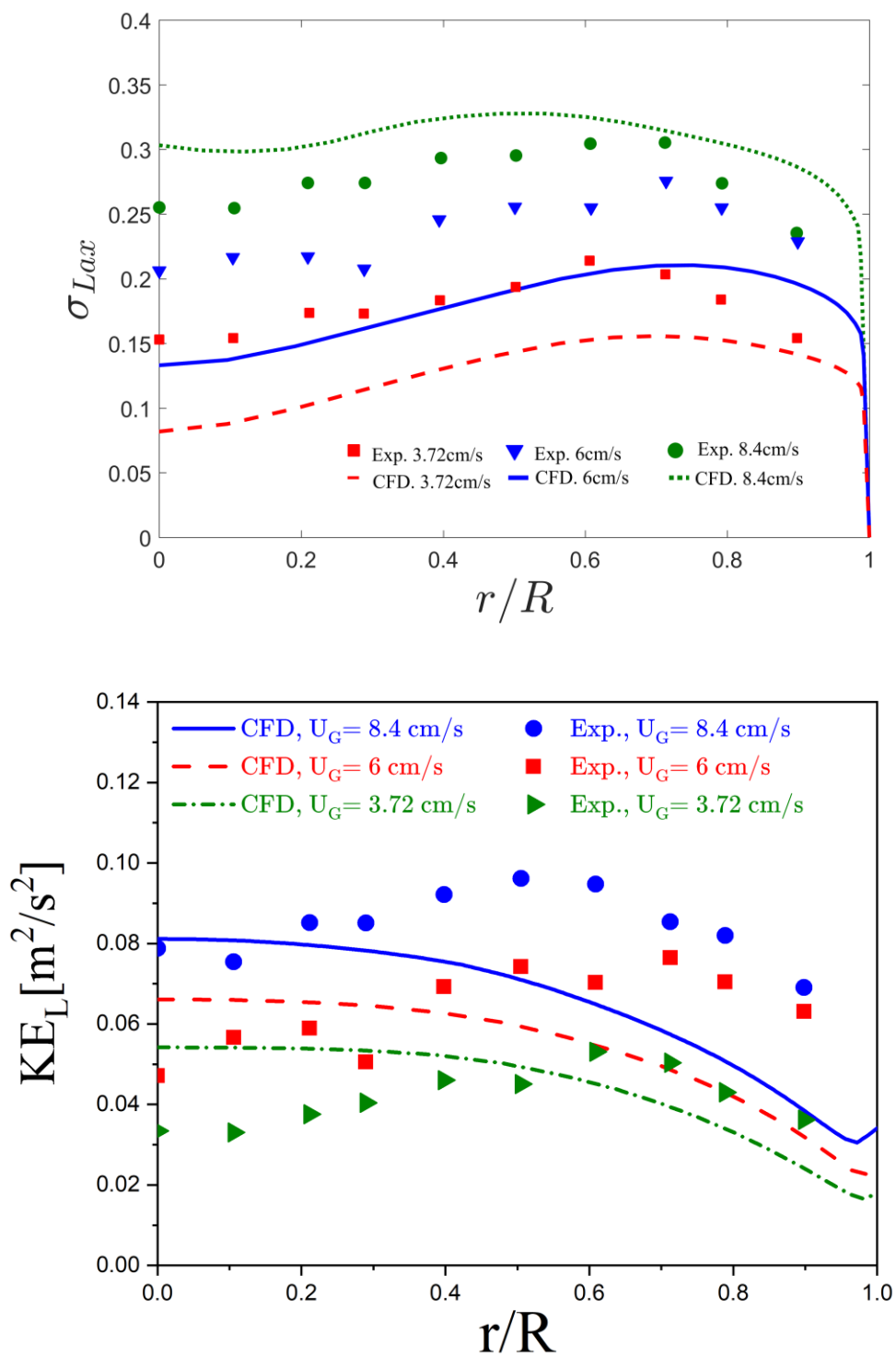
Fig 3.13 Radial profiles of axial *rms* of liquid velocity fluctuations (top) and liquid turbulent kinetic energy (bottom) for different U_G.
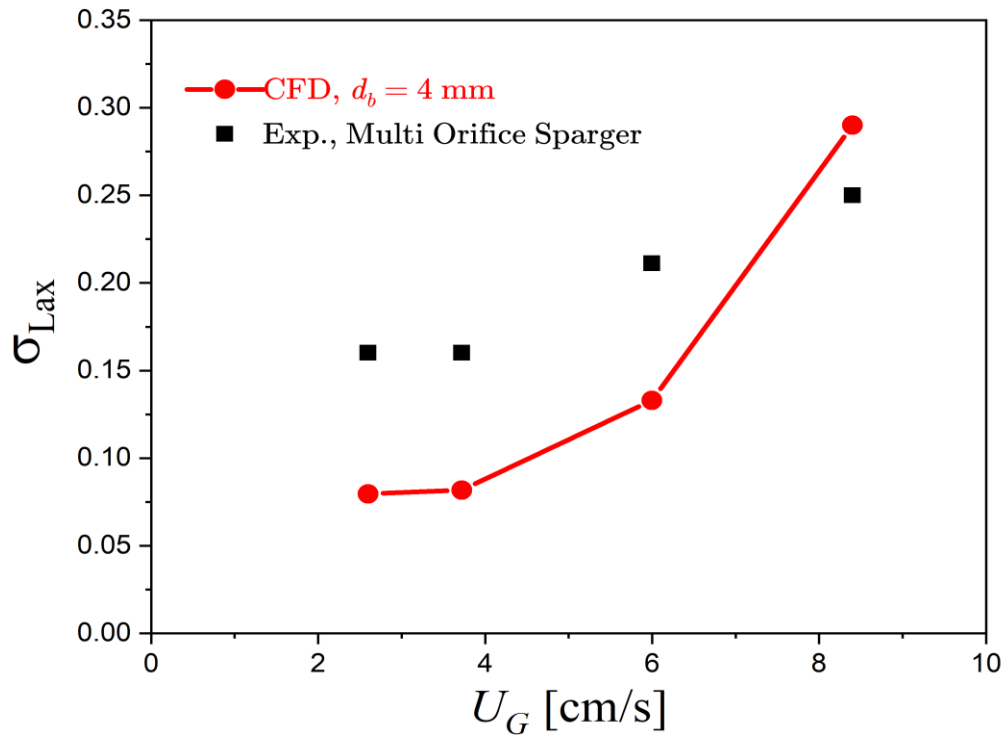
Fig 3.14 Sectional averaged axial *rms* of liquid velocity fluctuations at height of 0.7 m for different U_G.
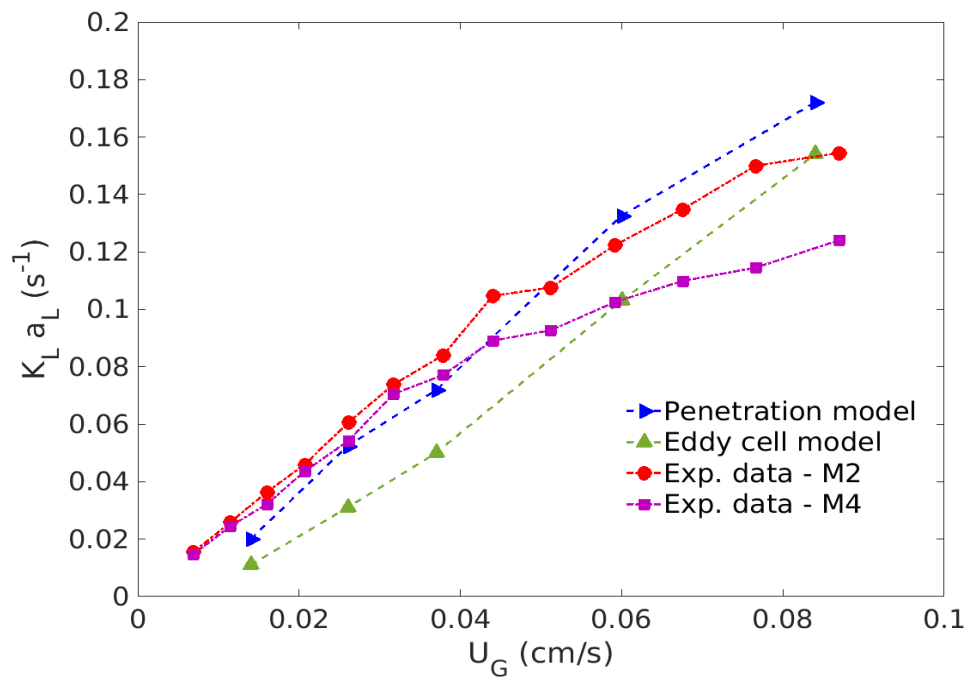
Fig 3.15 Comparison of numerically estimated $K_L a_L$ values with experimental predictions based on models 2 and 4 with probe dynamics.
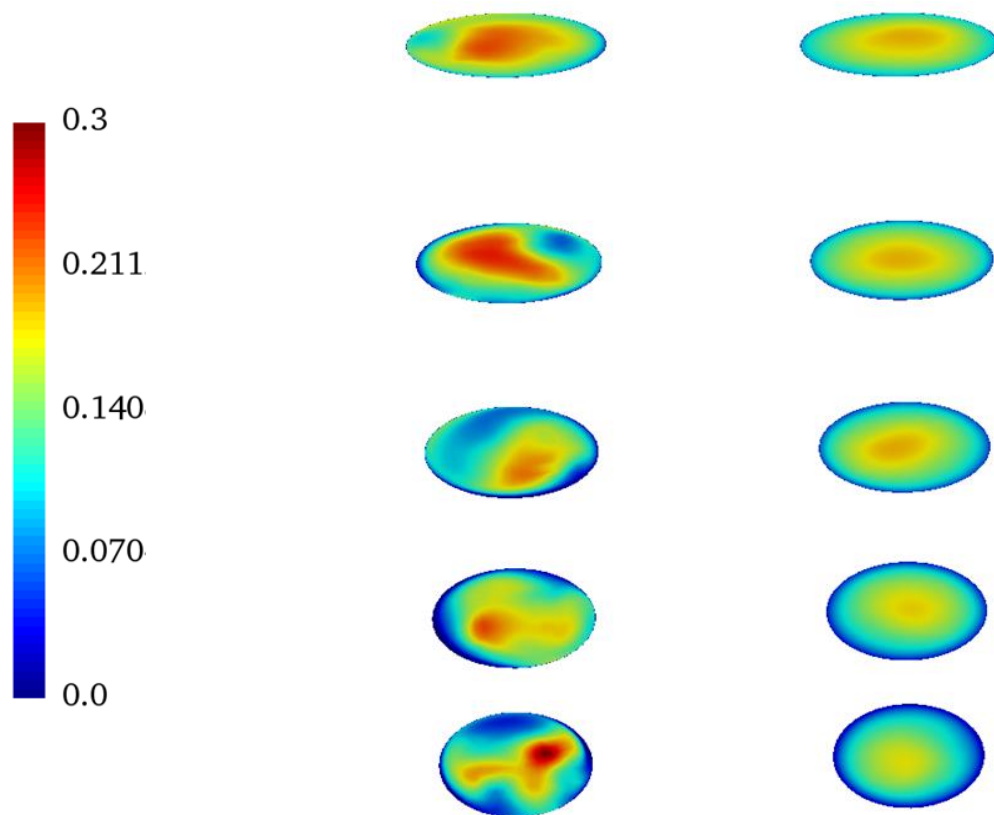
Fig 3.16 Predicted instantaneous (left) and time-averaged (right) distribution of the volumetric mass transfer coefficient by the penetration model at different cross-sections.

Chapter 4

Euler-Euler large eddy simulations of the gas-liquid flow in a cylindrical bubble column

In this section, Euler-Euler Large Eddy Simulations (LES) of dispersed turbulent gas-liquid flows in a cylindrical bubble column are presented. Besides, predictions are compared with experimental data from Vial et al. 2000 using laser Doppler velocimetry (LDV). Two test cases are considered where vortical-spiral and turbulent flow regimes occur. The sub-grid scale (SGS) modelling is based on the Smagorinsky kernel with model constant $C_s = 0.08$ and the one-equation model for SGS kinetic energy. The emphasis of this work is to analyze the performance of the one-equation SGS model for the prediction of bubbly flow in a three-dimensional high aspect ratio bubble column (H/D) of 20 and investigate the influence of the superficial gas velocity using the Open-FOAM package. The model is compared with the Smagorinsky SGS model and the mixture $k - \varepsilon$ model in terms of the axial liquid velocity, the gas hold-up and liquid velocity fluctuations. The bubble induced turbulence and various interfacial forces including the drag, virtual mass and turbulent dispersion were incorporated in the current model. Overall, the predictions of the liquid velocities are in good agreement with experimental measurement using the one-equation SGS model and the Smagorinsky model which improve the mixture $k - \varepsilon$ model in the core and near-wall regions. However, small discrepancies in the gas hold-up are observed in the bubble plume region and the mixture $k - \varepsilon$ model performs much better. The numerical simulations confirm that the energy spectra of the resolved liquid velocities in churn-turbulent regime follows the classical -5/3 law for low frequency regions and are close to -3 for high frequencies. More details of the instantaneous local flow structure have been obtained by the Euler-Euler LES model including large-scale structures and vortices developed in the bubble plume edge.

4.1 Introduction

Bubbly gas-liquid flows in multiphase reactors are important for many industrial processes, for instance in the chemical, biochemical, or environmental industries and have advantageous characteristics in mass and heat transfers. In bubble column reactors, the gas phase is dispersed in the form of tiny bubbles in a continuous liquid phase using a gas distribution device. The complex interplay between operating conditions, the gas-liquid interfacial area, bubble size, bubble rise velocity, turbulence in the liquid phase, and bubble-bubble interactions lead to extensive range of flow regimes and complex flow structures. Furthermore, as the bubbles rise in the column, they induce pseudo-turbulence in the liquid phase. Several numerical studies of these types of flows have been carried out by incorporating the turbulence of the liquid phase through the Reynold-Averaged Navier-Stokes (RANS) model (Mudde and Simonin, 1999; Plfeger and Becker, 2001; Tabib et al., 2008; Olmos et al., 2001; Selma et al., 2010; Stiriba et al., 2017; Kouzbour et al., 2020). The RANS approach, typically the $k - \varepsilon$ model, models the effect of liquid turbulence on the mean flow scale and uses isotropic closures, but fails to reproduce relevant flow physics since bubbles induce significant turbulence of anisotropic nature. It has provided valuable results and insights on the turbulence in bubble column reactors with reasonable computational costs.

Bubbly flow is characterized by the development of distinct flow structures of different length scales, especially for transition and heterogeneous flow regimes. Turbulent scales varied from those of the characteristic length of the mean flow to those of the microscopic ones. For instance, the largest turbulence scales are comparable in size to those of the mean flow and depend on the reactor geometry and flow conditions, whereas the smallest scales depend on the bubble dynamics and are proportional to the bubble size. The large-scale turbulent motions interact with the bubbles and thereby affect their motions, whereas the small scales not only dissipate the kinetic energy but can generate energy to the largest scales and tend to be more isotropic as well (Dhotre et al., 2013; Ma et al., 2015a, and 2015b). The energy spectra of the liquid fluctuations exhibits the broad range of

frequency and gives a power law scaling with the slope of -5/3 for low frequency regions which is progressively replaced by -25/3 in Lui et al. 2018 and over than -8/3 in the works of Ma et al. (2015a, and 2015b) and Lance and Bataille (1991) for high frequency regions.

To reproduce relevant flow physics and give comprehensive insights into two-phase flow turbulence, the LES approach has attracted great attention in the simulation of dispersed two-phase turbulent flows. It has been used in several investigations and simulations to predict multiphase flow dominated by large coherent structures or eddies in bubble columns, stirred tanks and many other reactors (Tabib et al., 2011; Dhotre et al., 2008). As in single phase flows, LES model resolves directly the interaction of the large-scale motions with bubbles, whereas the less energetic smallest motions including the interaction of the bubbles with the surrounding turbulence are represented in terms of sub-grid scale closure models. The Euler-Euler LES model predicts more accurately flows dominated by large coherent structures or eddies in bubble columns which carry most of the flow energy (typically 90%) than the traditional RANS models and represents more details of the flow structure (Ma et al., 2015a, 2015b; Dhotre et al. 2008). Furthermore, the $k - \varepsilon$ models consider isotropic turbulence and do not analyse the flow near the walls. Table 4.1 gives a summary of previous works of gas-liquid flows in bubble column reactors in a chronological manner. For instance, Zhang et al. (2006) investigated the Smagorinsky model with different values of the constant C_s and the dynamic Smagorinsky model. Niceno et al. 2008 applied the one-equation SGS turbulent kinetic energy LES and suggested that the sub-grid scale kinetic energy obtained from the model can be used to assess the SGS dispersion turbulent force. Tabib et al. (2011) employed the commercial CFD package ANSYS CFX to analyze the inclusion of SGS turbulent dispersion (TD) force and concluded that the results of a coarser mesh can be improved by using a lower magnitude of SGS-TD force. Liu et al. (2018) studied the scale adaptive of LES ANSYS CFX code using a small $\Delta/d_B \leq 1$. These works have made several assumptions in the CFD modelling, reactor geometry and operating conditions. Indeed, their bubble columns are operating at low superficial gas velocities with non-uniform aerations or use flat bubble column reactors. At high

gas flow rates, the flow field is unsteady and characterized by local recirculation near the sparger and different scale vortices in the core region.

In view of this, it is desirable to carry out LES in a three-dimensional bubble column at high inlet superficial gas velocity. The purpose of this work is therefore to employ Euler-Euler LES approach to simulate dispersed turbulent two-phase flows in a three-dimensional cylindrical bubble column of high aspect ratio (H/D) of 20 with special emphasis on the performance of the one-equation SGS model and the influence of the superficial gas velocity. A multiple nozzle gas distributor is used for uniform aeration. The inlet superficial gas velocities, used in this work, are $U_G = 6.0$ and 8.4 cm/s where vortical-spiral and turbulent flow regimes occur, respectively. The simulations are set up according to experimental works of Camarasa et al. (2000) and Vial et al. (2001) using LDA as well as they have been performed by using the twoPhaseEulerFoam solver implemented in the Open-FOAM v.4.0.0 software package. The results achieved from the one-equation model SGS are compared with the Smagorinsky model with constant $C_s = 0.08$ and the mixture $k - \varepsilon$ model. The accuracy of the results in comparison to experimental data are evaluated. Comprehensive simulations were conducted to examine the instantaneous flow structure and Reynolds stresses. Furthermore, the analysis of the energy spectra of resolved velocity and the vorticity distribution have been addressed.

4.2 Two fluid model and numerical setup

4.2.1   The flow equations

The two-fluid model is built up on the spatial filtering for LES or conditional averaging for RANS of the conservation equations of mass and momentum. In this approach, both phases, the continuous liquid phase and the dispersed gas phases, are modelled as two interpenetrating continua. In LES cases, it is assumed that the filtered equations are used to compute the large-scale lengths while the effect of unresolved turbulent scales are modelled using a sub-grid model. In the

61

present work, the flow is assumed to be adiabatic, without considering the interfacial mass transfer between the air and the water phases.

The present formulation closely follows the procedure outlined by Weller 2005, where the mass and momentum equations for the phase φ are given by

$$\frac{\partial(\rho_\varphi \alpha_\varphi)}{\partial t} + \nabla \cdot (\rho_\varphi \alpha_\varphi \mathbf{U}_\varphi) = 0 \tag{1}$$

$$\frac{\partial(\rho_\varphi \alpha_\varphi \mathbf{U}_\varphi)}{\partial t} + \nabla \cdot (\rho_\varphi \alpha_\varphi \mathbf{U}_\varphi \mathbf{U}_\varphi) = -\alpha_\varphi \nabla p_\varphi + \alpha_\varphi \rho_\varphi \mathbf{g} - \nabla \cdot (\alpha_\varphi \rho_\varphi \boldsymbol{\tau}_\varphi^{\text{eff}}) + \mathbf{M}_\varphi \tag{2}$$

Here α_φ is the volume fraction of each phase, $\mathbf{U}_\varphi$ is the phase resolved velocity, and $\tau_\varphi^{\text{eff}}$ represents the effective stress tensor usually decomposed into a mean viscous stress and turbulent stress tensor for the phase φ as

$$\boldsymbol{\tau}_\varphi^{\text{eff}} = -\nu_\varphi^{\text{eff}} \left[\nabla \mathbf{U}_\varphi + (\nabla \mathbf{U}_\varphi)^T - \frac{2}{3}(\nabla \cdot \mathbf{U}_\varphi)\mathbf{I} \right] + \frac{2}{3} k_\varphi \mathbf{I} \tag{3}$$

where k_φ is the turbulent kinetic energy of phase φ, $\mathbf{I}$ is the identity tensor, and ν_φ^{eff} is the effective viscosity of phase φ. The effective viscosity of the liquid phase is obtained through the summation of the molecular viscosity, the shear-induced turbulent viscosity, and the bubble-induced turbulent viscosity

$$\nu_\varphi^{\text{eff}} = \nu_{L,L} + \nu_{L,\text{Tur}} + \nu_{L,\text{BIT}} \tag{4}$$

and is formulated in the present study using two models: (a) the Smagorinsky model proposed by Zhang et al. (2006), (b) and the one-equation sub-grid-scale model proposed by Niceno et al. (2008).

The Smagorinsky model is a zero-equation turbulent LES model and the liquid phase shear-induced turbulent viscosity is formulated as follows

$$\nu_{L,\text{Tur}} = (C_S \Delta)^2 |S| \tag{5}$$

Here C_S is a model constant, S is the characteristic filtered rate of the strain and $\Delta = Vol^{1/3}$ is the filtered width, where Vol is the volume of the computational cell. The model constant seems to be different for different flow situation and was chosen to be $C_S \approx 0.08$ according to the work of Zhang et al. 2006. The turbulence model corrects the SGS turbulent viscosity by a contribution due to the bubble induced turbulence (Zhang et al., 2006) and the model proposed by Sato and Sekoguchi (Sato and Sekoguchi, 1975) was employed

$$\mu_{L,\text{BIT}} = \rho_L C_{\mu,\text{BIT}} \alpha_G |\mathbf{U}_G - \mathbf{U}_L| \tag{6}$$

with its constant $C_{\mu,\text{BIT}}$ set to 0.6.

The one-equation sub-grid-scale model by Niceno et al. (2008) solves a transport equation for the unresolved kinetic energy k_{SGS}. The model is able to account for the effects of bubble induced turbulence through an additional source term in the transport equation for k_{SGS} in the continuous phase and uses the modelled SGS energy to estimate the SGS turbulent dispersion force (Niceno et al., 2008). The sub-grid kinetic energy equation is given by

$$\frac{\partial k_{SGS}}{\partial t} + \nabla \cdot (k_{SGS}\mathbf{U}) - \nabla \cdot \left[(\nu_{L,L} + \nu_{SGS})\nabla k_{SGS}\right] = G - C_\varepsilon \frac{k_{SGS}^{3/2}}{\Delta} \tag{7}$$

where G is the production term, defined as

$$G = v_{SGS}|\bar{S}_{ij}| \tag{8}$$

and the sub-grid viscosity is

$$v_{SGS} = C_k \Delta k_{SGS}^{1/2} \tag{9}$$

The model constants are $C_\varepsilon = 1.05$ and $C_k = 0.07$ (Niceno et al., 2008).

In Eq. (2), $\mathbf{M}_\varphi$ represents the inter-phase momentum exchange between phase φ and the other phase due to various interphase forces. The interfacial forces are decomposed into four contributions

$$\mathbf{M}_\varphi = \mathbf{M}_\varphi^D + \mathbf{M}_\varphi^L + \mathbf{M}_\varphi^{VM} + \mathbf{M}_\varphi^{TD} \tag{10}$$

where the forces on the right-hand side of equality are the drag force denoted by $\mathbf{M}_\varphi^D$, the lift force represented by $\mathbf{M}_\varphi^L$, the virtual mass force by $\mathbf{M}_\varphi^{VM}$, and the turbulent dispersion force by $\mathbf{M}_\varphi^{TD}$. There are many models for each of these forces depending on their applicability, the flow regime and the operating conditions as discussed by (Joshi, 2001; Vial and Stiriba, 2013; and Ziegenhein et al., 2015). There is still no complete agreement on the closures or the combination to be used at best. The drag force (per volume) for the liquid phase is estimated as

$$\mathbf{M}_L^D = \frac{3}{4}\alpha_G \rho_L \frac{C_D}{d_B}|\mathbf{U}_r|\mathbf{U}_r \tag{11}$$

where C_D refers to the drag force coefficient and is calculated according to the Schiller-Naumann correlation and $\mathbf{U}_r$ is the relative velocity. Many drag model have been proposed and compared in

the literature (Pourtousi et al., 2014; Tabib et al., 2008; Zhang et al., 2006; and Silva et al., 2012). But Tabib et al. 2008 found that Schiller-Naumann, Ishii-Zuber, Tomiyama, and Grace et al. using different turbulence closure ($k - \varepsilon$, RNG, LES) models give the same results in a cylindrical bubble column similar to our reactor. Furthermore, the Schiller-Naumann drag model works quite well for bubbly flow in industrial systems since bubbles are contaminated by surfactants at the interface and behaves like a rigid sphere (Clift et al. 1979).

The lift force results from the movement of bubbles through a non-uniform flow field due to shear or vorticity effects. The force (per volume) is modelled as

$$\mathbf{M}_L^L = \alpha_G \rho_L C_L \mathbf{U}_r \times (\nabla \times \mathbf{U}_r) \tag{12}$$

where C_L is a constant lift force. We conducted the same simulation with different lift coefficients and the model of Tomiyama et al. (2002), but no noticeable improvements in the results were observed, from which we conclude that the lift force plays a minor role in our test cases. Furthermore, the steady simulations of a bubble column reactor (Vial and Stiriba, 2013) show that the lift force was overshadowed by the turbulent dispersion force which better predicted the radial dispersion of the gas phase along the axial direction of the bubble column and the experimental gas hold-up at the column center using a single-orifice nozzle.

Liquid acceleration in the wake of the bubble is taking into account through the virtual mass force, which is modelled as

$$\mathbf{M}_L^{VM} = \alpha_G \rho_L C_{VM} \left(\frac{D\mathbf{U}_L}{Dt} - \frac{D\mathbf{U}_G}{Dt} \right) \tag{13}$$

where C_{VM} is the virtual mass coefficient and is taken to be 0.5 for individual spherical bubbles (Zhang et al., 2006; Dhotre et al., 2008).

The SGS component of those forces will be neglected except the turbulent dispersion force which can be estimated using the modelled SGS energy in the one-equation model. The turbulent dispersion force proposed by Lopez de Bertodano et al. (1994) is adopted. It is modelled as

$$\mathbf{M}_L^{TD} = C_{TD}\rho_L k\nabla\alpha_G \tag{14}$$

Several turbulent dispersion coefficients C_{TD}, required to obtain good agreement with experimental measurements, were tested. For the one-equation and mixture $k - \varepsilon$ models we use $C_{TD} = 0.8$.

4.2.2   Numerical simulation set-up

The numerical simulations were carried out in a cylindrical bubble column with uniform aeration. The geometry of the current bubble column reactor is the same as used by Vial et al. (2001) and Camarasa et al. (2000) in their experiments. The height of the column is $H = 2$ m, the diameter is $D = 0.10$ m, and the static liquid height is 1.5 m. The reactor is operated with the water and air as the continuous and dispersed phases at the room temperature and atmospheric pressure, respectively, at two superficial gas velocities 6.0 cm/s and 8.4 cm/s corresponding to transition and heterogeneous flow regimes. The gas is injected from the bottom of the column through a multiple-orifice nozzle for uniform aeration and it allows us to study the flow regime transition. The gas distributor is treated as a uniform mass flow rate through the bottom boundary calculated from superficial gas velocities for mass conservation with gas volume fraction of 1.0. The pressure at the inlet is set to zeroGradient and specified by zero gradient. At the outlet, the pressure is specified as the atmospheric pressure, and the gas hold up is set to inletOutlet with zero gradient for outflow and fixed value for backward flow. The no-slip condition is applied at the walls for the velocities and Dirichlet condition for the gas hold-up. Moreover, for the one-equation model we apply wall functions.

The numerical simulations were carried out with the open source CFD package Open-FOAM library (Weller et al., 1998). The governing equations of continuity and momentum as well as the transport equation for k_{SGS} are solved by the two-phase flow solver twoPhaseEulerFoam available in Open-FOAM v4.0.0. The solver is based on a finite volume formulation to discretize the model equations which has shown to be stable for transient calculations (Weller, 2005). The first-order bounded implicit Euler scheme is adopted for the time integration, the gradient terms are approximated with a linear interpolation, the convective terms are discretized with second-order upwind scheme, and the diffusive terms are interpolated with the Gauss linear orthogonal scheme. We employ the PIMPLE algorithm to solve the pressure-velocity coupling where the pressure equation is solved, and the predicted velocities are corrected by the pressure change. The preconditioned conjugate gradient (PCG) is used for solving the discretized pressure equation and the incomplete-Cholesky preconditioned bi-conjugate gradient (BICCG) for the other set of linear equations. For more detailed discussions of all steps mentioned above (Rusche, 2002; Weller, 2005).

Prior to the description of the computational mesh and presenting the results, we emphasis the implications of bubble size distribution on the model. In the present work, we assume a spherical bubble size distribution of 4.5 mm according to bubble size measurements of Camarasa et al. (2000). The same simplification was successfully used by Khan et al. (2017) to simulate their bubble column using $k - \varepsilon$, RSM, and Smagorinsky turbulence model at high superficial gas velocities. Perhaps the incorporation of bubble coalescence and break up in the LES may help in predicting the flow field in the vortical-spiral regime (Khan et al., 2017). But note also that, recently, Huang et al. (2018) implemented and used variable bubble size models in modelling three-dimensional large diameter bubble columns operating under churn turbulent flow regime; they concluded that the model did not lead to any substantial improvement relative to the single size models and highlighted the need for improved breakup and coalescence closure descriptions.

67

The computational mesh was generated using the Gmsh finite element mesh generator. In order to check that the computed results are grid-independent, different grids with $d_B/\Delta = 0.75, 1.1, 1.4$ and 1.875 have been analysed by increasing the number of computational cells in the center of the column and the axial direction from 3 mm to 5 mm and stretching the mesh near the walls (Table 4.2). Milelli et al. (2001) established the criterion of the ratio of the bubble diameter to cut-off filter size: $\Delta/d_B \geq 1.5$, that is to say that the mesh size must be at least 50% larger than the bubble diameter for Eulerian-Eulerian simulations. Fig. 4.1 shows a comparison of the axial liquid velocity. All the meshes show very similar results and mesh 3 and 4 perform better in the near-wall region. In this work, we have employed a medium mesh with a filter width $\Delta = 5$ mm ($\Delta/d_B = 1.1$), which quantitively seems to give better agreements and ensures a good compromise between the CPU time and accuracy at the column center and close near the walls. As can be seen from Fig. 4.1, we have checked the non-dimensional spacing x+, y+, and z+ desirable to make a large eddy simulation setup convincing. Note that for comparison, Niceno et al. (2008) used the criterion $\Delta/d_B = 1.2$ and found no significant difference with the coarser one satisfying Milelli condition, Dhotre et al. (2008) found a good agreement with experimental data using both conditions $\Delta/d_B = 1.2$ and $\Delta/d_B = 2.5$, and Liu et al. 2018 used the criterion $\Delta/d_B \leq 1.0$ and concluded that the grid size does not have to be larger than a single bubble. All transient calculations are started from static conditions with the liquid at rest and the gas is injected with a mass flow rate corresponding to the experimental superficial gas velocity. We start calculations with a fixed small-time step of $\Delta t = 0.0005$ s for the first 20 s then we increase it to 0.001 s to account for the transient instabilities of bubbly turbulent flows. The flow was simulated for 200 s and the averaged results from t = 50 s to t = 200 s were quantitively compared with experimental data. All the simulations were performed in parallel mode on a PC cluster with 16 nodes, Intel Xeon, 2.8 GHz, 4 GB RAM. The different time-averaged profiles displayed in section 3 are given at the mid height of the bubble column ($H = 1$ m).

4.3 Numerical results

4.3.1 The one-equation SGS and Smagorinsky model

The resolved axial liquid velocity is presented in Fig. 4.1(a), it can be seen that there is no significant change in the prediction between the medium and the fine mesh. In order to understand that how the LES model resolves well the fluid flow in the column numerically, Pope (2011) suggested to measure and check when the ratio of resolved kinetic energy to the total turbulent kinetic energy is greater than 80%, i.e.,

$$\gamma = \frac{k_{res}}{k_{SGS} + k_{res}} > 0.8, \qquad k_{res} = \frac{1}{2}\overline{u'_L u'_L} \tag{15}$$

This ratio is plotted in Fig.4.1(b) at height $h = 0.7$ m. We get the same results for different height positions in a plane normal to the axial flow direction. The ratio is around 80% with the medium grid used and the LES resolves more flow in the core regions. Hence, the resolution of the LES with the present mesh can be considered acceptable for analysis.

The surface bubble diameter, d_B, was measured by Camarasa et al. (1999) for different inlet superficial gas velocities (Fig. 4.2(b)). For heterogeneous hydrodynamic regimes ($U_G > 5$ cm/s), d_B is nearly equals to 4.5 mm and in reasonable agreement with our assumption. The measured bubble size distribution is also given by Camarasa et al. (1999), where spherical bubbles were observed in the new-wall region and large bubbles of different shapes in the core region, and exhibit a relatively narrow distribution around 4.5 mm. Numerically, three different bubble sizes 3.5, 4.5, and 5.5 mm were employed to test the bubble size effect on the simulation results, see Fig. 4.2(a). The calculated axial liquid velocities are very similar and the results for 4.5 mm are closest to the experimental data, this value will be used for the rest of this work.

The axial liquid velocity profiles predicted by the mixture $k - \varepsilon$ model (Behzadi et al., 2004) and the one-equation SGS have been compared with experiments, so as to realize the relative behavior of different turbulence models, and the results are shown in Fig. 4.3. It can be seen that both models provide good agreements with experiments and that RANS model over-predicts the liquid velocity for the near-wall region. The reason for this over estimation may come from the fact that a bubble plume moves upward in a spiral rotating manner in the center with the liquid flow meantime small spherical bubbles spirally move downward close near to the wall column, accelerating the water flow; the mixture $k - \varepsilon$ model does not analyse this flow near the wall due to the inappropriateness of standard wall functions developed basically for single phase flow. The one-equation SGS model predicts the overall behavior of the axial liquid velocity profile better than the RANS model and gives good agreement with experimental measurement. For the gas hold-up (Fig. 4.4), the two turbulence models capture the experimental profiles reasonably well. It can be however observed that the LES model under predicts the gas hold-up at the center of the column for $-0.5 \leq x/R \leq 0.5$, where the flow is dominated by large-scale structures, whereas the RANS model performs much better. In the near wall region where the flow is dominated by small-scale structures, the situation is different, and the gas hold up predicted by LES is much closer to the experimental data. The inclusion of the turbulent dispersion force in the RANS model decreases the axial liquid velocity in the core region and results in a comparatively flatter gas hold-up profile, which can predict the profile closer to the experimental data in the core region. Similar RANS results were reported by Tabib et al. (2008).

Fig. 4.5 displays radial distribution of the time-averaged axial bubble velocity at the mid height of the bubble column ($H = 1$ m). Unfortunately, experimental measurements are not available for comparison. The results show similar trends as those reported in Zhang et al. (2006) and Dhotre et al. (2008); the bubble plume spreading in the center and a relatively steep gas velocity profile for high superficial gas velocity which leads to less dispersed bubble plume.

Fig. 4.6 shows profiles of the fluctuations of the liquid velocity at height 0.7 m. All the profiles are based on the resolved part of liquid velocities. Unfortunately, experimental data on kinetic turbulent energy of the liquid phase are not available. In fact, Vial et al. (2001) only measured the *rms* in the axial and radial directions. Fig. 4.6(a), (b) displays a comparison of liquid fluctuations in the other directions. Clearly, the velocity fluctuations in the present bubble column reactor are anisotropic. The time-averaged span-wise component $\langle v'v' \rangle^{1/2}$ increases smoothly away from the wall and attains a maximum at the center of the column, whereas the streamwise fluctuations $\langle u'u' \rangle^{1/2}$ display a periodic trend with a lower value in the core region which attains its highest value close near to the wall in a similar way to the axial fluctuations displayed in Fig. 4.6(a). This is probably due to the liquid movements from upward to downward and laterally at the center and close to the wall column in which $\langle u'u' \rangle$ peaks with high magnitude near the wall. Ma et al. (2015b) observed the same trend in their quasi-2D bubble column and Deen et al. (2001) in a 3D bubble column reactor with a non-uniform aeration faced the same scenario. As shown above, the high inlet gas flow rate induces substantial turbulence both in the core and in the wall regions which changes the trend of liquid fluctuations. Furthermore, it is worth noting that values of axial liquid fluctuations are higher than the other components and dominate in both the core region and near the walls.

The liquid Reynolds shear stresses $\langle u'v' \rangle$ and $\langle v'w' \rangle$ are far smaller than the normal stresses and increase with the gas flow rate as shown in Fig. 4.6(d). As mentioned in Mudde et al. (1997), the large vortical flow structures significantly influence the Reynolds stresses since the vortices span the entire width of the column. The large contribution to the Reynolds shear stresses become larger in the vortical flow region since the fluctuations in the vertical component dominate close to the center region of the column where the liquid moves in a wavy manner, whereas $\langle u'v' \rangle$ peaks in the central plume and in the near wall region. The Reynolds shear stresses experience fluctuations due to the swinging motion of the bubble plume. At higher superficial gas velocity $U_G = 8.4$ cm/s

the intensity of the large-scale turbulence is much higher due to the bubble motion which accelerates the liquid flow and causes an overestimation of the liquid velocity in the central plume region.

Fig. 4.6(a) also shows comparisons between experiments and numerically predicted vertical liquid velocity fluctuations where it can be seen that the one-equation SGS model can reproduce the experimental data much better than the RANS model. The time-averaged axial liquid velocity averaged through the cross-sectional area normal to the axial direction at height $h = 0.7$ m is given in Table 4.3. One can see the good agreement for both gas flow rates. The effect of the turbulent dispersion was added by incorporating the sub-grid scale turbulent dispersion force using the SGS kinetic energy obtained from the one-equation LES model using mesh sizes coarser than the bubble size (4.5 mm). The axial liquid velocity profiles are practically the same near the wall and agree best with experimental data as we increase C_{TD}. With coefficients (C_{TD}) larger than 0.8 the profiles do not improve anymore. We found that such interfacial force improves the liquid velocity profile as in Tabib et al. (2011) who have shown that even a small magnitude of turbulent dispersion SGS is enough to affect the flow profile.

Fig. 4.7 shows a comparison between the Smagorinsky and one-equation SGS models for the axial liquid velocity at $U_G = 8.4$ cm/s. The resolved part by the one-equation model shows better agreement for the liquid velocity, whereas the Smagorinsky model over-predicts the experimental data in the center and captures the trend of the down-flow circulation in the near-wall region. However, the gas hold-up is under-estimated and becomes flatter in the core region. Zhang et al. (2006) and Dhorte et al. (2008) compared different LES models. Their results over-predicted experimental profiles and became steeper for high values of C_S than 0.15 since the turbulent viscosity increases and damps the bubble plume. With $C_S = 0.08$ the CFD model provides a good solution for the time-averaged axial liquid velocity. The axial liquid velocity fluctuations predicted by both models are very similar to each other. For the rest of this work we use the one-equation model to analyze the instantaneous flow as well as the energy spectra.

4.3.2   *Instantaneous flow*

The instantaneous flow structure in 3D bubble columns was classified, based on visual study of (Chen et al., 1994; Lin et al., 1996; Goraki Fard et al., 2020), into four distinct regions: an oscillating plume accompanied with two staggered rows of vortices, fast bubble region, vortical flow region, and descending flow region close near the walls. A two-phase flow computational model has to capture all these features observed in the experiments. Snapshots of instantaneous liquid velocities vector field together with the gas hold-up contour plot are shown in Fig. 4.8 and 4.9 for the simulations using RANS and LES models in the plane of symmetry and several cross-sections at different superficial gas velocities, respectively. The time-averaged results are also displayed in Fig. 4.8. The gas injected from the bottom forms clusters of bubbles that move upward in a wavy manner along the region of the central plume. Multiple smaller and larger vortex cells are continuously generated in the vortical-spiral region and along the side of the bubble plume, which stagger on each other and change their size and position in time. The behavior of the bubble plume and the undulation shape of the bubble swarm simulated by LES are more dynamic than those obtained by RANS at the recorded instant, exhibiting more appreciable swinging motion and result in more complicated bubble-induced flow structures. The transient liquid field seems to be more uniform near the free surface at $U_G = 6.0$ cm/s for RANS; as a result, we see recirculating zones that push bubbles to disappear from the liquid phase. From the present LES, the time-averaged global gas from the injector to the free-surface is found to be nearly 20%. In the cross-section the flow moves in a spiral way forth and back. In the core region, higher values of the gas hold-up are obtained meaning the existence of the central bubble region. Both the instantaneous and time-averaged snapshot show the vortical-spiral flow region close to the wall. The instantaneous profile highlights that the Euler LES model has been able to capture the four flow regions and can be used for education of coherent flow structures.

There are many vorticity criteria used to identify and visualize vorticity regions and characteristic three-dimensional eddy structures, for instance, the $Q-$ criterion, $\lambda 2-$ criterion, and $\Delta-$ criterion (see Chen et al., 2015). In this work, we chose $\lambda-2$ method to visualize the iso-surface of vortical structures coloured by the vertical liquid velocity in the column (Fig. 4.10). The color shows the magnitude of the liquid axial velocity, $\lambda-2=-2$, where the large-scale structures consist mainly of plume structures meandering and oscillating. Complex vortical rings are formed in the central plume and vortical regions, adjacent to the descending flow region, where high velocity and velocity fluctuations are noticed, so the liquid particles tend to spin around itself forming vortices. There are more vortex loops near the sparger and at $U_G = 8.4$ cm/s, suggesting that more turbulence is generated. Unlike RANS, it can be seen the high degree of randomness exhibited by LES near the center and along the sidewalls. As noticed by other authors (Hu et al., 2008), it is believed that the estimated flow behavior based on LES model, is to be closer to the real flow situation and that LES resolves many more transient details of the flow (Fig. 4.8).

Overall, the instantaneous results and the liquid velocity fluctuations profiles reveal the generation of large-scale structures moving upward in a meandering way in the bubble plume region and spiraling downward in the near-wall region, as shown in Fig. 4.8 and 4.9, by the formation and motion of cluster of bubbles and the subsequent bubble wake interaction. Strong vortices of different sizes are developed in the plume edge. The turbulence is anisotropic, and the liquid axial fluctuations are significantly larger than in the stream-wise or span-wise directions dominating the turbulent kinetic energy. The one-equation SGS model predicts accurately the axial liquid fluctuations and fails to capture the gas hold-up in the core plume region.

4.3.3   Energy spectra

Fig. 4.11 and 4.13 show a 200 s time history plot of the resolved axial and stream-wise liquid velocity at one point $(x/R = y/R = 0$ m, $z = 0.7$ m) in the column corresponding to nearly

20,000 sample points and the corresponding energy spectra at $U_G = 6.0$ cm/s, while Fig. 4.13 and 4.14 display the same information at $U_G = 8.4$ cm/s. In Fig. 4.11 and 4.13, the transient behavior is well reflected in the high-frequency oscillations of liquid velocity components around time averaged values, depicted in red lines, due to the turbulent fluctuations. The amplitude of fluctuations increases with the inlet gas flow rate where axial component contains more frequencies.

The energy spectrum densities (PSD) obtained from LES with data extracted from Fig. 4.11 and 4.13 and cover the time from 50 s to 200 s are shown in Fig. 4.12 and 4.14. As can be seen, each spectrum displays a broad range of frequencies with slopes of about -5/3 in the frequency region between 1 and 10 Hz. For high frequency region (> 10 Hz) the decay becomes faster with a slope steeper than -3 power law. Several authors analyzed the power spectrum based on Euler-Euler LES data and obtained different slope decay in the inertial subrange region. For instance, Dhotre et al. (2008) and Ma et al. (2015a) used the BIT model of Sato et al. (1981) and the obtained slope was partly over than -10/3, while Lin et al. (2018) obtained a -25/3 power laws. By comparing both predicted spectra for higher frequencies, large inlet gas flow rate gives more dissipation and the bubbles alter the PSD significantly (Fig. 4.12 and 4.14). Two lines with slopes -5/3 and -3 are shown in the figures. For $U_G = 6.0$ cm/s, the PSD curve exhibits a slope close to -10/3 for the radial liquid velocity and close to –11/3 for the axial liquid velocity, whereas for $U_G = 8.4$ cm/s the curve clearly follows the k^{-3} line in the high frequency inertial and dissipation region as observed experimentally in grid turbulence configurations in Lance and Bataille (1991); Riboux et al. (2010); Martinez Mercado et al. (2010) and Prakash et al. (2016). The PSD of the span-wise velocity component, not presented here, exhibits the same behavior for both superficial gas velocities.

Several works investigated the fast decay in the dissipation range of the energy spectrum and attributed it to buoyancy-generated inertia force and bubble-induced viscosity effects. Ma et al. (2015a, 2015b) compared their LES energy spectrum with the experimental spectrum of Akbar et al. (2012) and found that their resolved and reliable angular bubble frequencies are far away, and

that the frequency information related to the bubble wake is lost. The origin of the -3 slope was explained by Prakash et al. (2016), wherein the authors examined a frequency that is representative of the bubbles and its impact on the resulting spectra. In the present case, the representative bubble frequency may be estimated as $f_B = |\mathbf{U}_r|/(2\pi d_B) \approx 9$ Hz, where $|\mathbf{U}_r| \approx 25$ cm/s being the bubble velocity and $d_B \approx 4.5$ mm the averaged bubble diameter, so that above this value the PSD changes the characteristic slope -5/3 to -3, which implies that there an energy input on the scale of bubble diameter (d_B) and frequency of bubble motion.

4.4 Conclusions

Euler-Euler large eddy simulations of dispersed turbulent gas-liquid flow in a three-dimensional cylindrical bubble column, with high aspect ratio (H/D) of 20 and multiple orifice gas nozzle, have been presented. Effects of all drag forces, non-drag forces, sub-grid turbulent dispersion and bubble induced turbulence are all accounted for. For the time-averaged axial liquid velocity and gas hold-up, it is found that the present model based on the one-equation SGS shows good agreement with experimental measurement data from Vial et al. 2000, and improves the axial liquid velocity of the mixture $k - \varepsilon$ model in the near wall regions and the bubble plume but small discrepancies in the gas hold-up are observed in the core region. The mixture $k - \varepsilon$ model accurately predicts the radial distribution of the gas hold-up. For the time-averaged axial liquid velocity and gas hold-up, it is found that the present model based on the one-equation SGS shows good agreement with experimental measurement data from Vial et al. 2000, and improves the axial liquid velocity of the mixture $k - \varepsilon$ model in the near wall regions and the bubble plume but small discrepancies in the gas hold-up are observed in the core region. The one-equation model performs much better than the Smagorinsky model with $C_S = 0.08$ in the central plume and vortical flow regions. The Smagorinsky model improves the resolved axial liquid velocity profile in the near-wall region.

The effect of inlet superficial gas velocities was investigated. Two inlet superficial gas velocities, corresponding to transient and turbulent flow regimes, were chosen for simulations. It is found that the present model agrees well with experimental data for $U_G = 6.0$ cm/s and small discrepancies are obtained for $U_G = 8.4$ cm/s. The classical -5/3 law of power spectral density of the resolved liquid velocities is obtained for low frequency regions and -10/3 (-3) for high frequencies at $U_G = 6.0$ cm/s ($U_G = 8.4$ cm/s). The normal Reynolds stress of the resolved part gives very good agreement with experiment and the shear stresses $\langle u'w' \rangle$ are similar to those obtained by Ma et al. (2015a) using a flat rectangular bubble column reactor. Finally, the present study indicates that a CFD model based on Euler-Euler One-equation SGS LES reasonably predicts the hydrodynamics of two-phase flow in bubble column reactors in turbulent-churn flow regime when a multiple-orifice nozzle is used for gas distribution.

Reference	Bubble column dimensions	Gas distributor	Bubble diameter	Superficial gas velocity	SGS model
Deen et al., 2001	Rectangular column, $W = 0.15$ m, $D = 0.15$ m, $H = 1$ m	Perforated plate, 49 holes of $D = 1$ mm	4 mm	0.49 cm/s	Smagorinsky, $C_S = 0.1$
Bove et al., 2004	Rectangular column, $W = 0.05$ m, $D = 0.2$ m, $H = 0.45$ m	Perforated plate, 49 holes of $D = 1$ mm	4 mm	0.5 cm/s	VLES, $C_S = 0.12$
van den Hengel et al., 2005	Rectangular column, $W = 0.15$ m, $D = 0.15$ m, $H = 1$ m	Perforated plate, 49 holes of $D = 1$ mm	3 mm	0.5 cm/s	Smagorinsky with DBM
Zhang et al., 2006	Rectangular column, $W = 0.15$ m, $D = 0.15$ m, $H = 1$ m	Perforated plate, 49 holes of $D = 1$ mm	4 mm	0.49 cm/s	Smagorinsky, $C_S = 0.08 - 0.2$
Niceno et al., 2008	Rectangular column, $W = 0.15$ m, $D = 0.15$ m, $H = 1$ m	Perforated plate, 49 holes of $D = 1$ mm	4 mm	0.5 cm/s	One-equation SGS
Dhotre et al., 2008	Rectangular column, $W = 0.15$ m, $D = 0.15$ m, $H = 1$ m	Perforated plate, 49 holes of $D = 1$ mm	4 mm	0.5 cm/s	Smagorinsky $C_S = 0.12$, and dynamic Smagorinsky
Hu and Celik, 2008	Rectangular column, $W = 0.08$ m, $D = 0.15$ m, $H = 2$ m	Flush mounted, 5 porous dicks of $D = 40$ mm	1.6 mm	0.66 cm/s	Smagorinsky, $C_S = 0.032$
Darmana et al., 2009	Rectangular column, $W = 0.24$ m, $D = 0.072$ m, $H = 0.8$ m	Multiple gas injection of 95 needles of $D = 0.51$ mm	4 mm	0.7 cm/s	SGS of Vreman , $C_S = 0.1$
Ekambara et al. 2010	Cylindrical column, $D = 0.15$ m, $H = 0.9$ m	Multipoint perforated plate, 25 holes of $D = 2$ mm	6 mm	0.2 cm/s	Smagorinsky, $C_S = 0.12$
Tabib and Schwarz, 2011	Cylindrical column, $D = 0.15$ m, $H = 1$ m	Multipoint perforated plate, 25 holes of $D = 2$ mm	3-5 mm	2 cm/s	One-equation SGS
Ma et al., 2015a	Rectangular column, $W = 0.243$ m, $D = 0.04$ m, $H = 1$ m	Multiple gas injection of 35 needles	iMUSIG, 2 groups	0.3 and 1.3 cm/s	Smagorinsky, $C_S = 0.15$
Ma et al., 2015b	Rectangular column, $W = 0.2$ m, $D = 0.05$ m, $H = 0.45$ m	Set of 8 holes in a rectangular configuration: 0.02 m $\times$ 0.0125 m	2 mm	0.17 cm/s	Dynamic Smagorinsky
Khan et al., 2017	Cylindrical column, $D = 0.15$ m, $H = 1$ m	Multipoint perforated plate, 25 holes of $D = 2$ mm	5 mm	2 – 10 cm/s	Smagorinsky, $C_S = 0.5$
Liu and Li, 2018	Rectangular column, $W = 0.15$ m, $D = 0.15$ m, $H = 1$ m	Perforated plate, 49 holes of $D = 1$ mm	4 mm	0.5 cm/s	Dynamic Smagorinsky
Present work	Cylindrical column, $D = 0.1$ m, $H = 2$ m	Multiple orifice plate, 62 orifices of $D = 1$ mm	4.5 mm	6 and 8.4 cm/s	Smagorinsky with $C_S = 0.08$, and one-equation SGS

Table 4.1. Summary of previous numerical simulations of gas-liquid flow in bubble columns using LES turbulence models

Mesh	$\Delta x \times \Delta y \times \Delta z$ $(\mathrm{mm^3})$	Δ/d_B	Turbulence model	Interfacial forces
Mesh 1	$7.5 \times 7.5 \times 7.5$	1.875	LES	$F_D + F_{VM} + F_{TD}$
Mesh 2	$5 \times 5 \times 7$	1.24	LES	$F_D + F_{VM} + F_{TD}$
Mesh 3	$5 \times 5 \times 5$	1.1	LES	$F_D + F_{VM} + F_{TD}$
Mesh 4	$3 \times 3 \times 3$	0.8	LES	$F_D + F_{VM} + F_{TD}$
Mesh 5	$5 \times 5 \times 7$	1.24	RANS	$F_D + F_{VM} + F_{TD}$

Table 4.2. The computational mesh and grid spacing investigated

Superficial gas velocity (cm/s)	6	8.4
Experimental (m/s)	0.2	0.25
CFD (m/s)	0.211	0.257

Table 4.3. Experimental and numerical centerline axial fluctuations of the liquid velocity
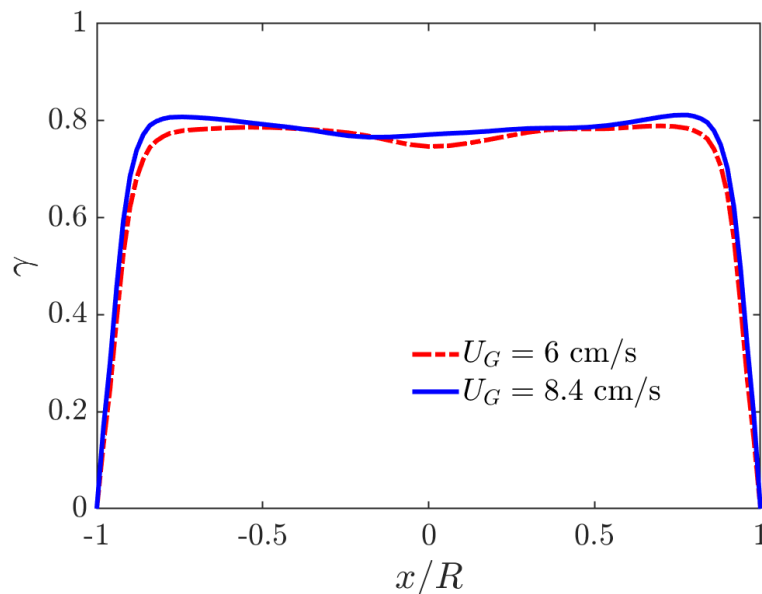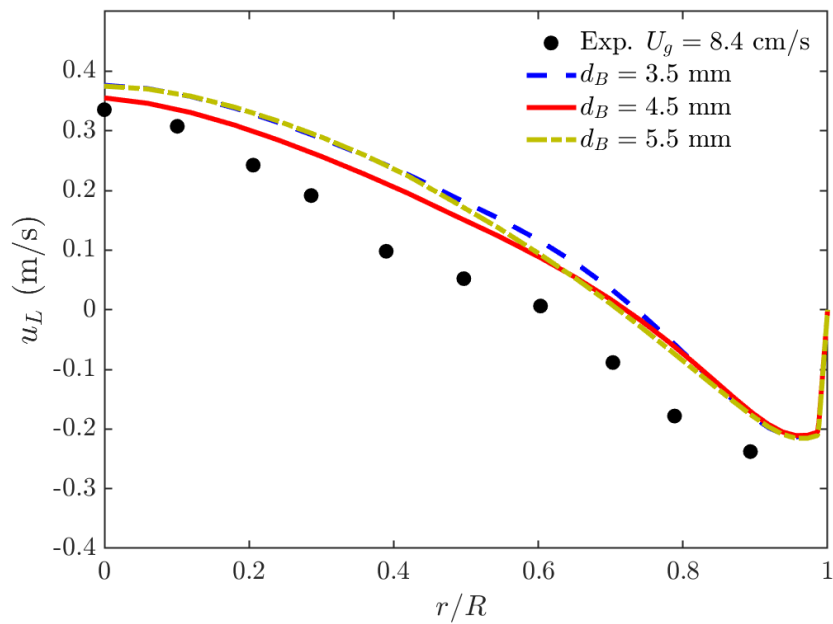
79

(a)
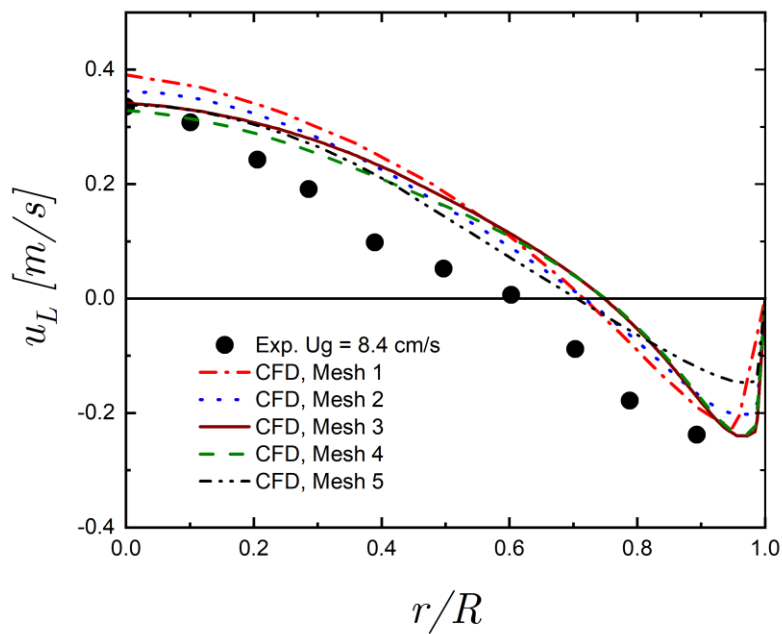
(b)

Fig. 4.1 Mesh independence analysis; comparison of the time-averaged results for the axial liquid velocity and the different meshes investigated at $U_G = 8.4$ cm/s (a); the ratio, γ, resolved kinetic energy to total kinetic energy (b).
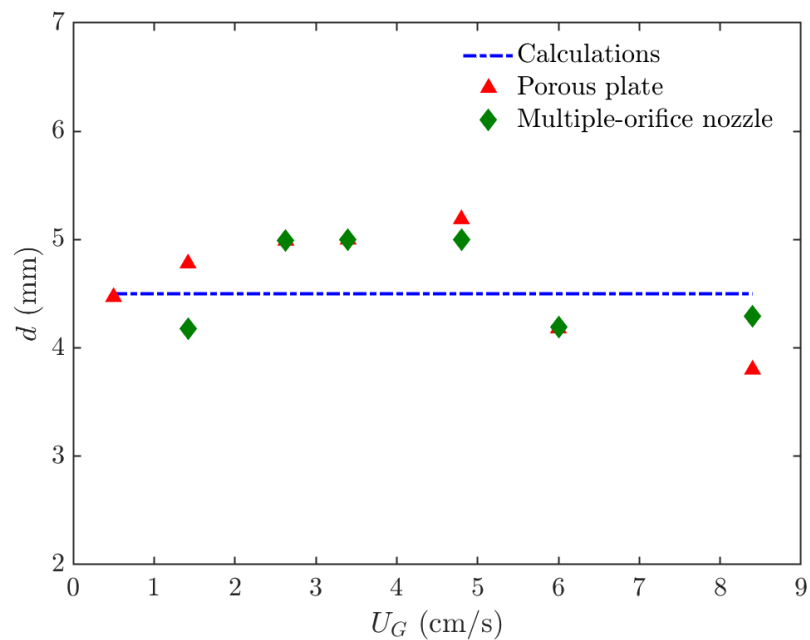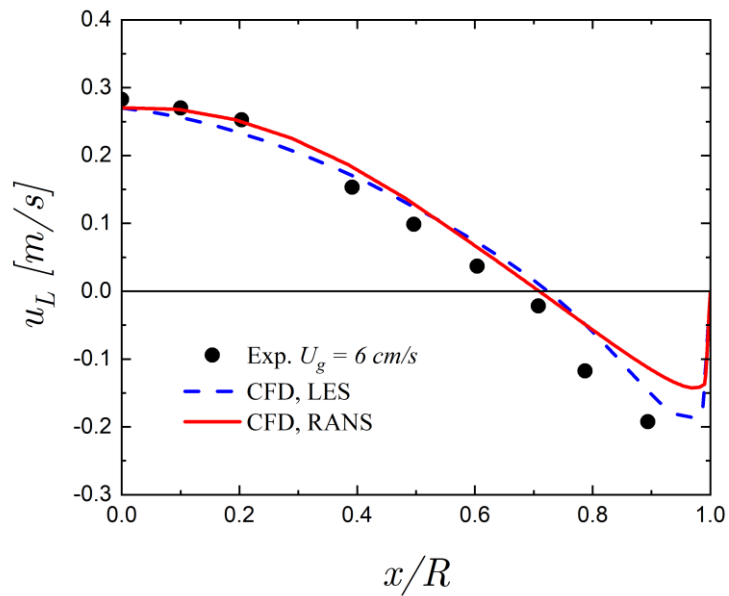
(a)

(b)

Fig. 4.2 Comparison between the simulated and experimental profiles of the axial liquid velocity using different bubble sizes at $U_G = 8.4$ cm/s (a), and comparison between experimental and numerical mean bubble diameter with U_G (b).

(a)

(b)

Fig. 4.3 Comparison between the simulated and experimental profiles of the axial liquid velocity at superficial gas velocity $U_G = 6.0$ cm/s (a) and $U_G = 8.4$ cm/s (b).
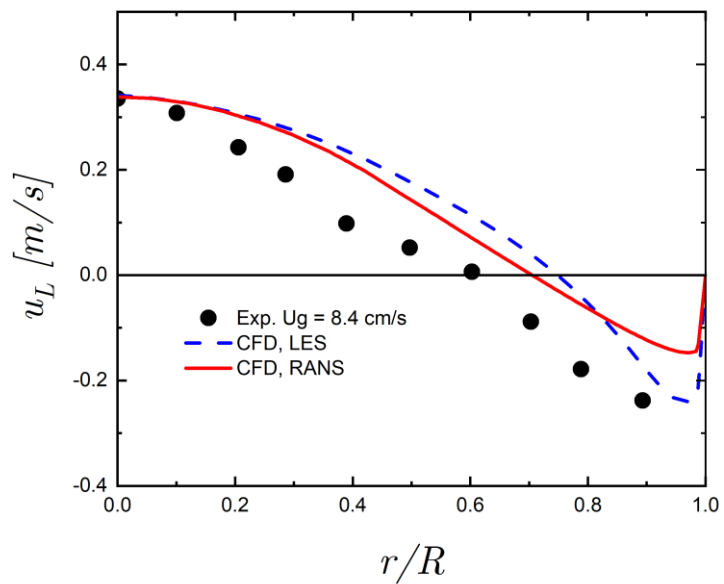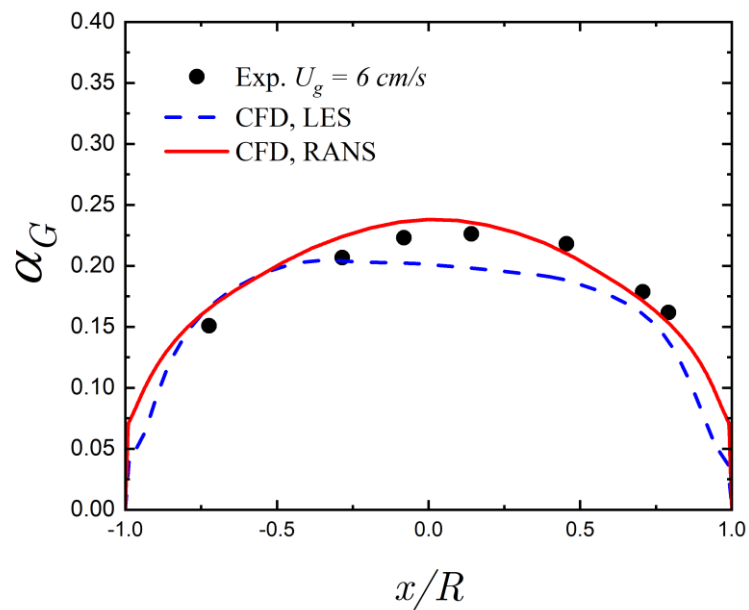
(a)

(b)
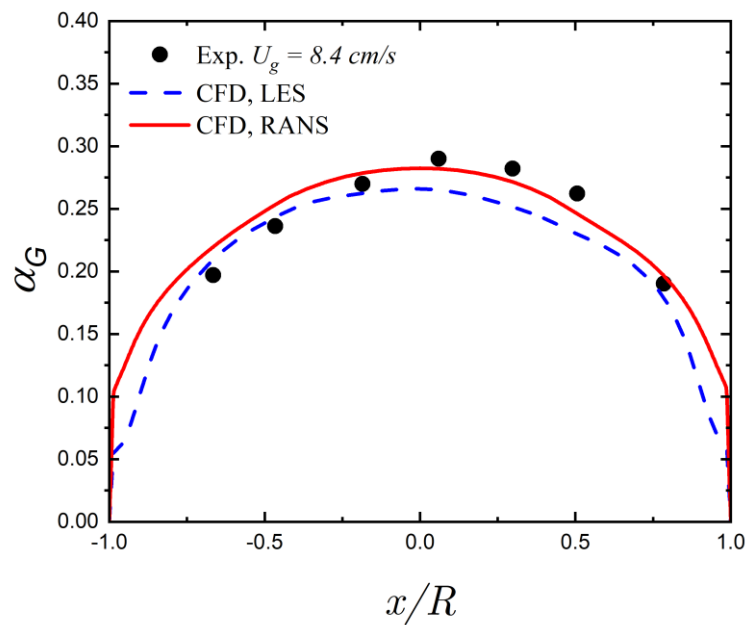
Fig. 4.4 Comparison between the simulated and experimental profiles of the local gas hold-up at superficial gas velocity $U_G = 6.0$ cm/s (a) and $U_G = 8.4$ cm/s (b).
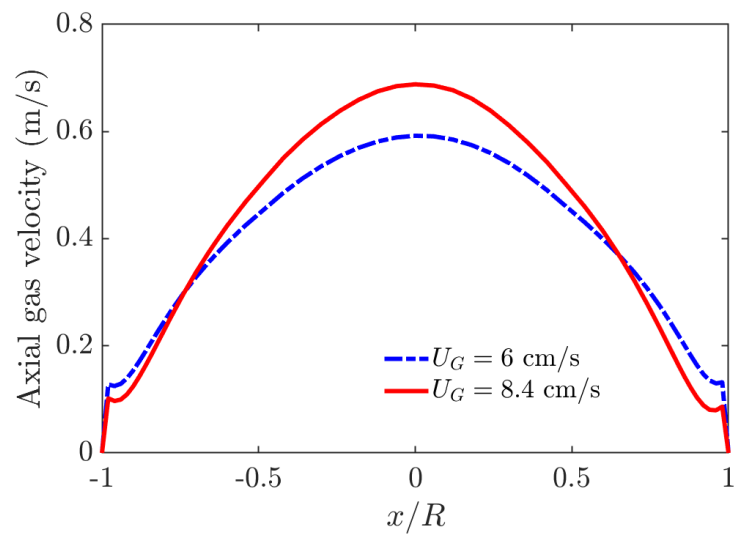
Fig. 4.5 Time averaged axial gas velocity at superficial gas velocity $U_G = 6.0$ cm/s and $U_G = 8.4$ cm/s.

(a)
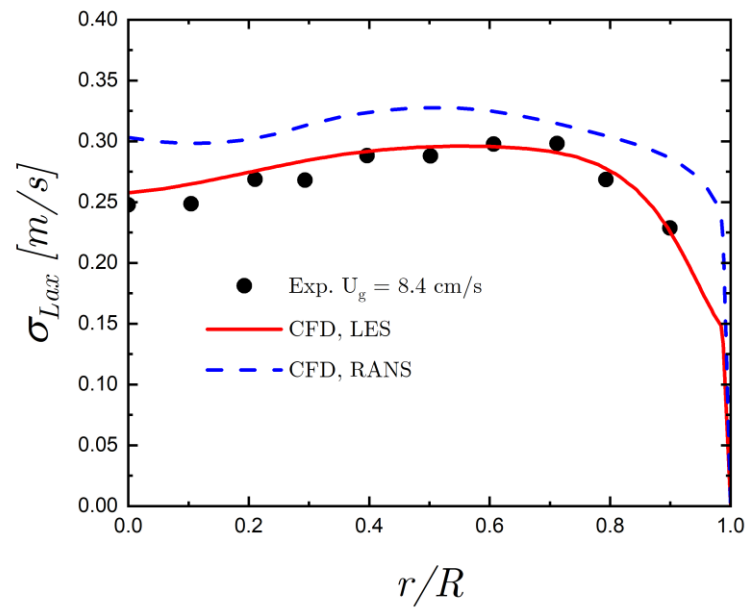
(b)
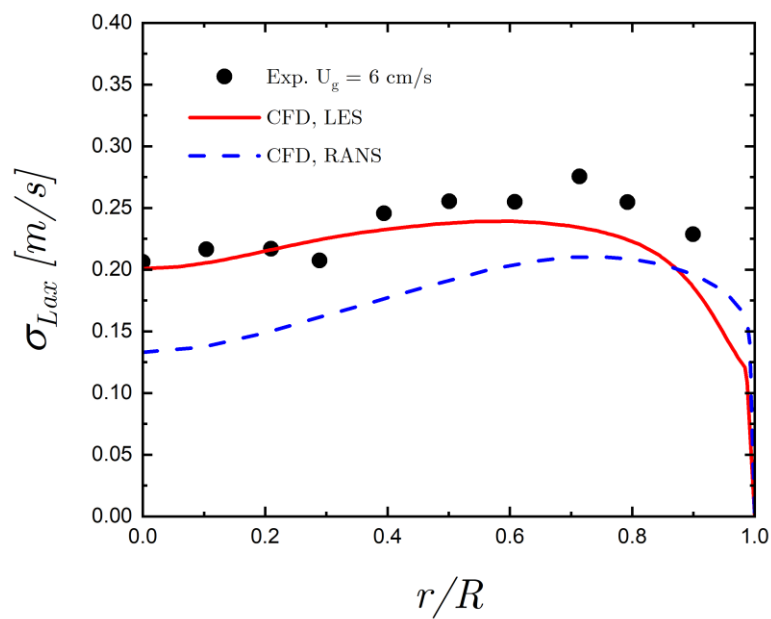
(c)
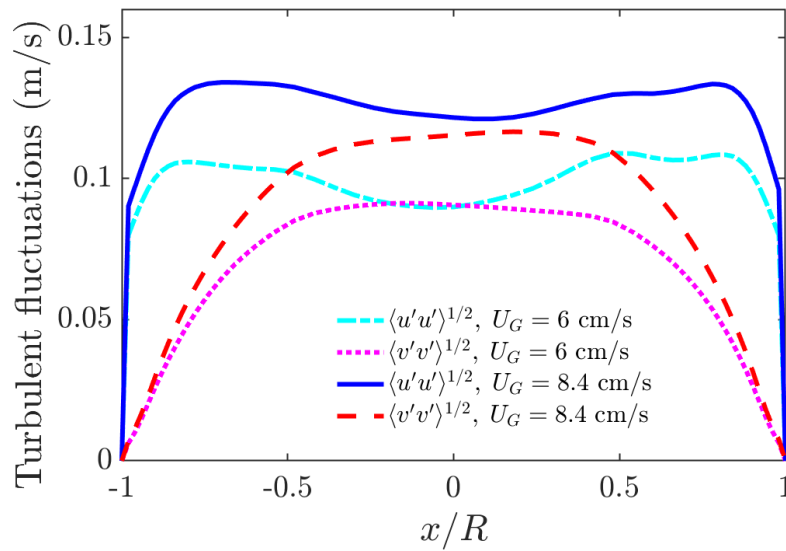
(d)
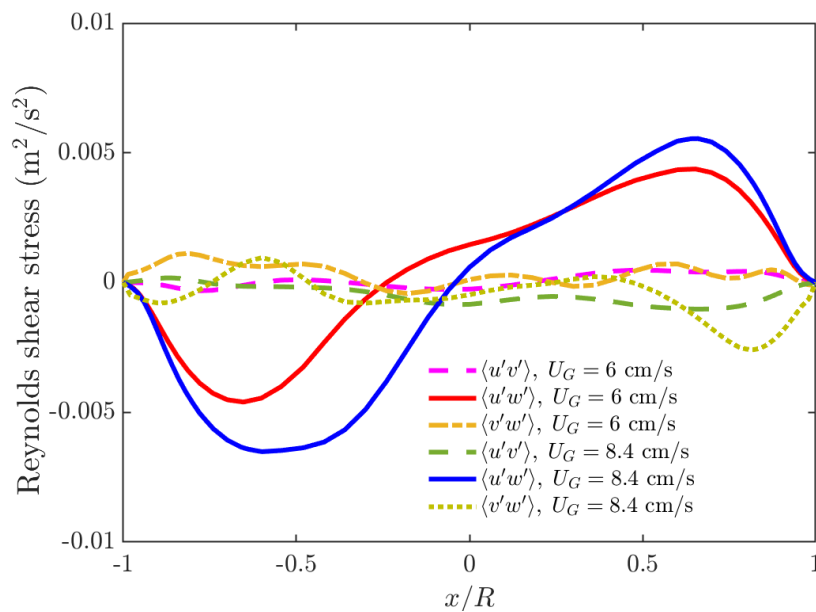
Fig. 4.6 Comparison between the simulated and experimental profiles of the axial *rms* liquid velocity fluctuations (a) and (b), turbulent fluctuations (c), and Reynolds shear stress (d).
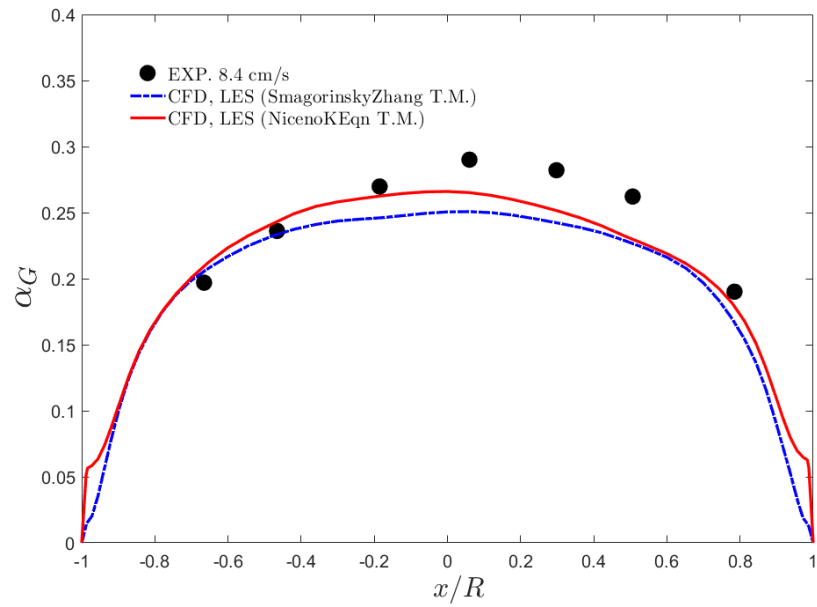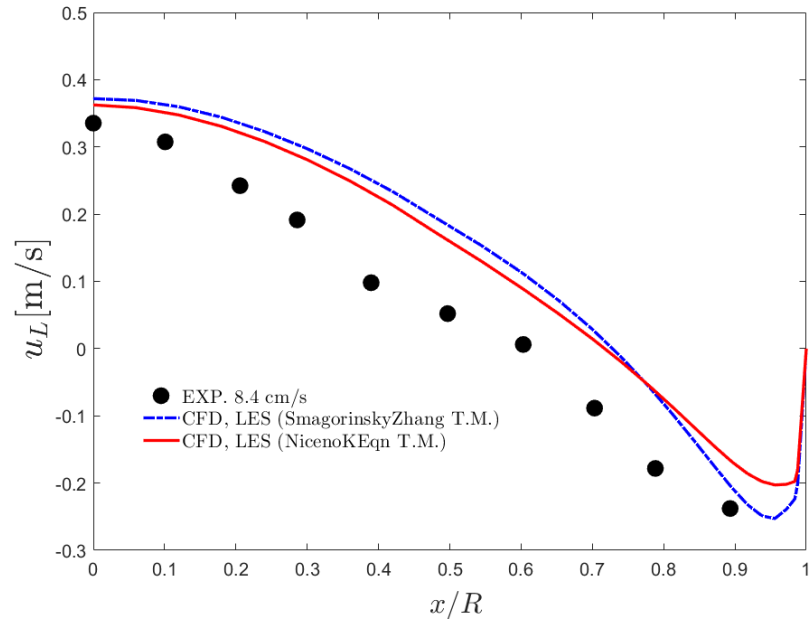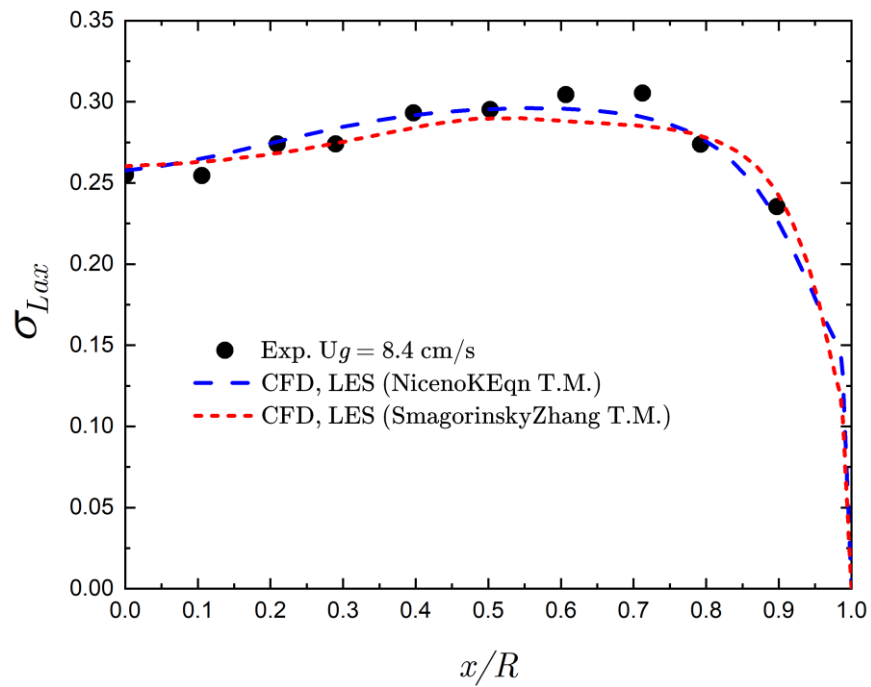
Fig. 4.7 Comparison between the simulated axial liquid velocity (top), the gas hold-up (center) and *rms* axial liquid velocity fluctuation results obtained using Smagorinsky and one-equation SGS models (bottom).
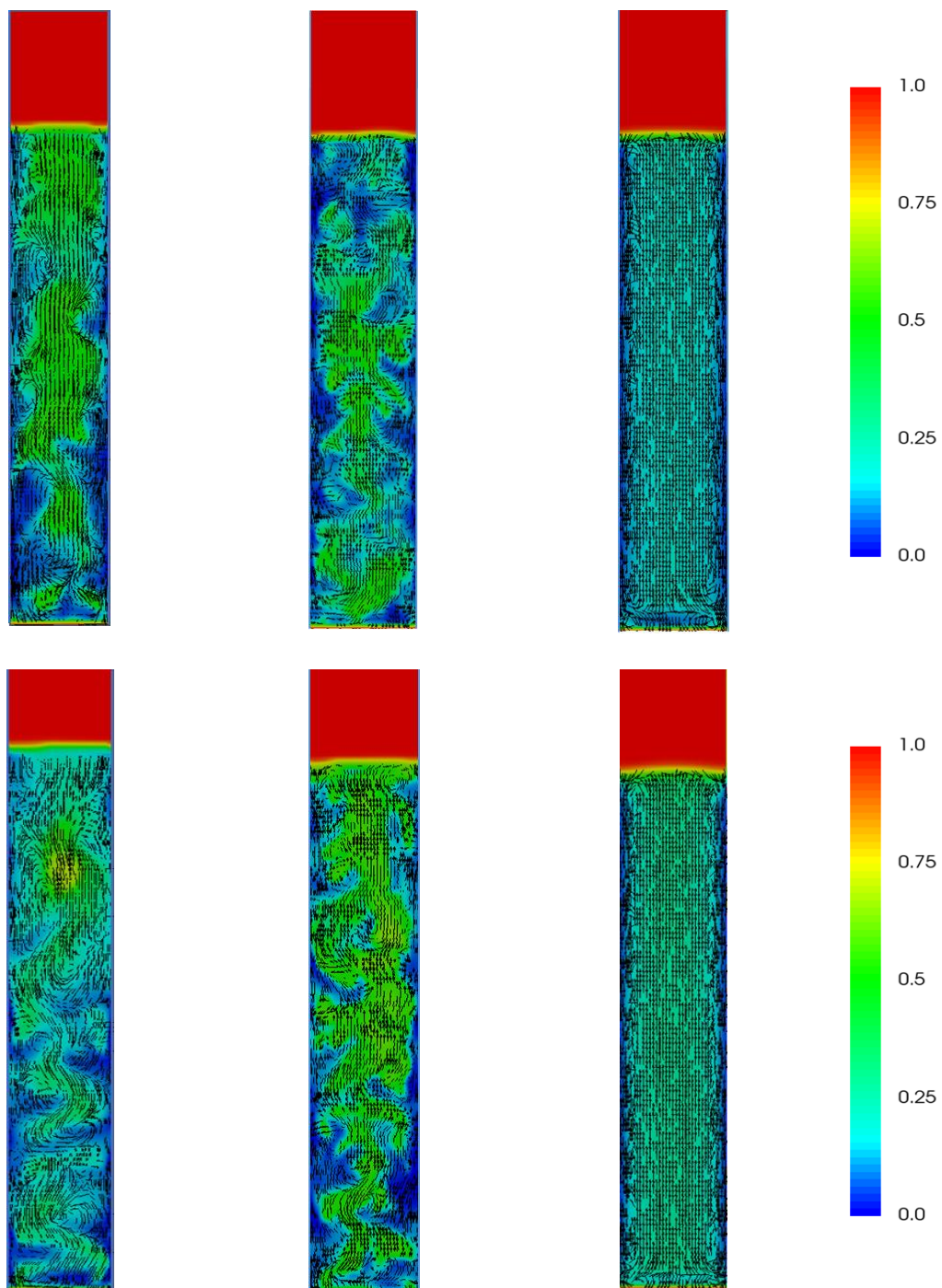
Fig. 4.8 Snapshots of instantaneous gas hold-up and liquid velocity field with RANS model (left) and LES model (center) and time averaged LES (right) at $U_G = 6.0$ cm/s (top), and $U_G = 8.4$ cm/s (bottom).
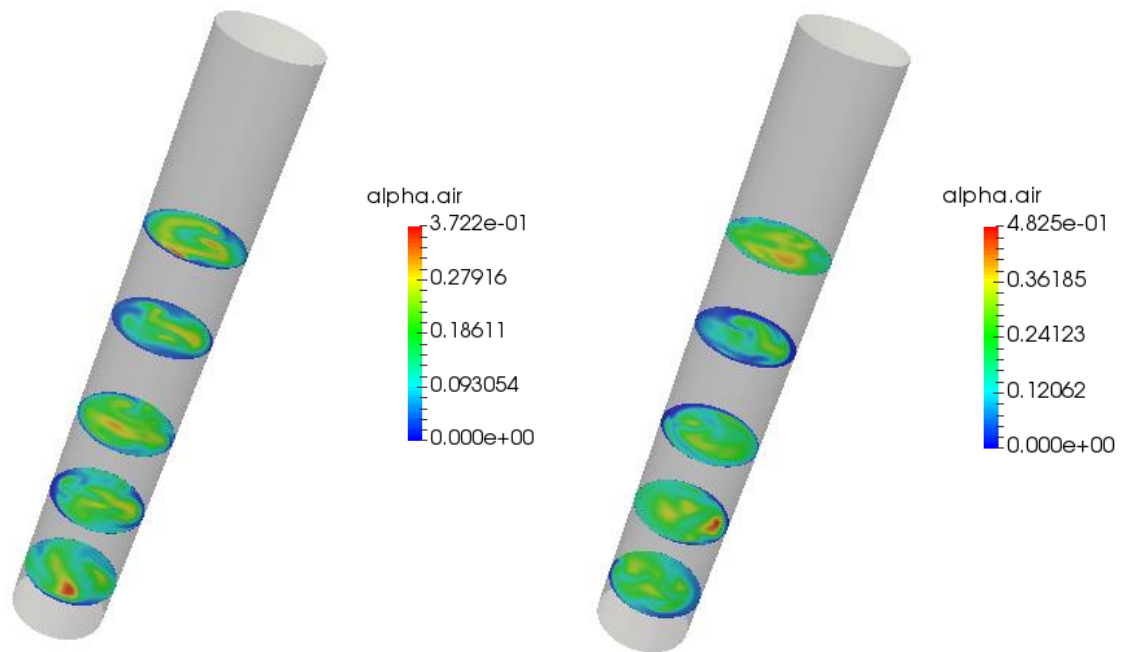
Fig. 4.9 Snapshots of instantaneous gas hold-up with LES model at $U_G = 8.4$ cm/s (right), and $U_G = 6.0$ cm/s (left).
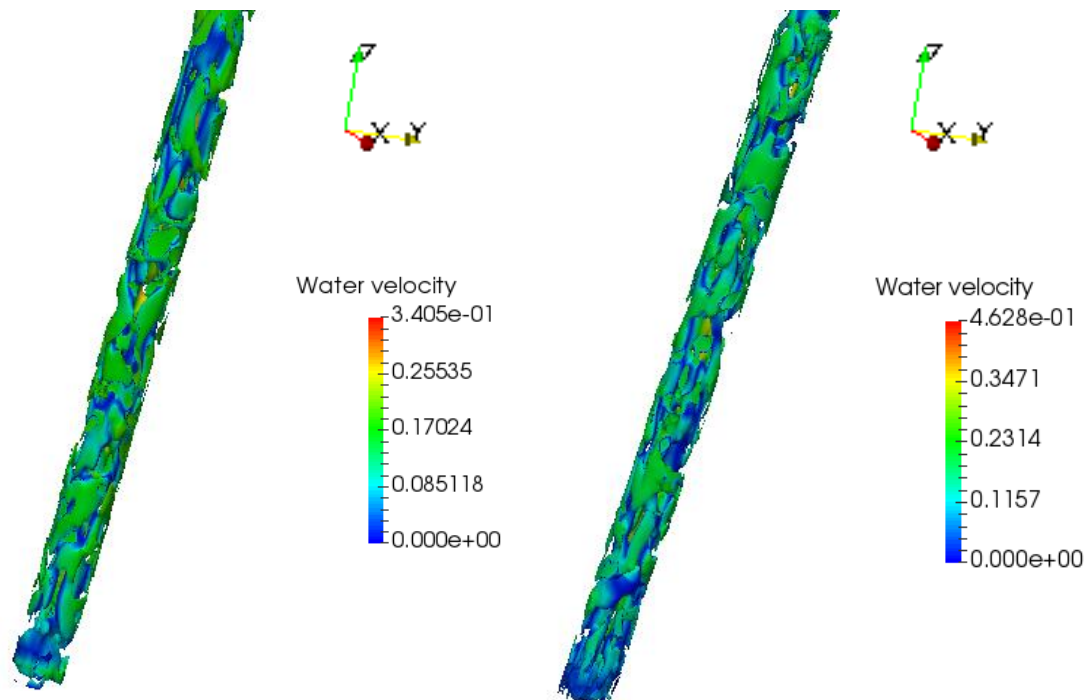
Fig. 4.10 Instantaneous vortical structure at time $T = 200$ s by $\lambda - 2$ method coloured by the magnitude of the liquid velocity, $\lambda - 2 = -2.0$; at $U_G = 6.0$ cm/s (left), and $U_G = 8.4$ cm/s (right).

(a)

(b)
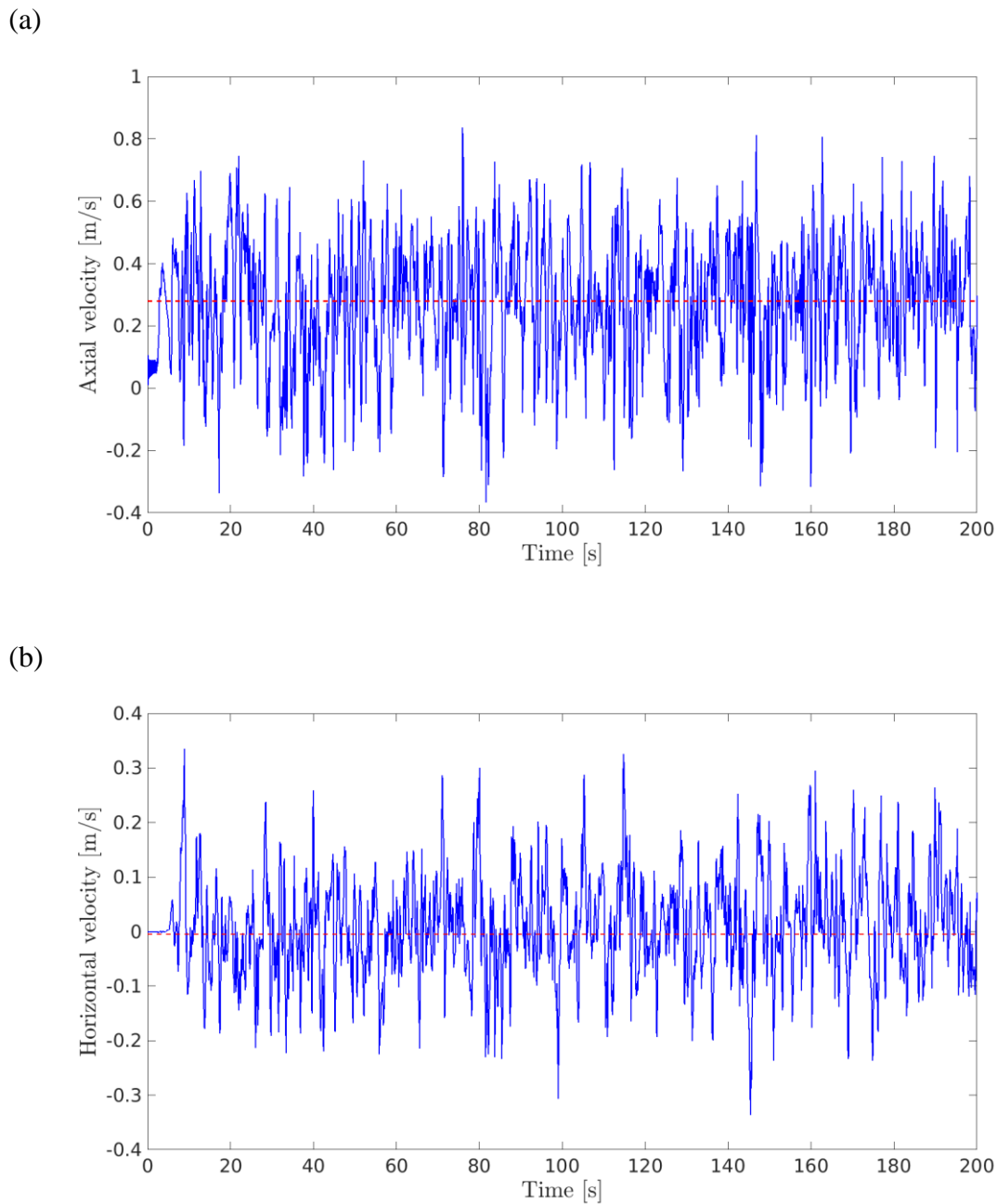
Fig. 4.11 Time history of the axial liquid velocity (a) and radial liquid velocity (b) with one-equation SGS model at the centerline of the column, at a height of $z = 0.7$ m and $U_G = 6.0$ cm/s.

(a)
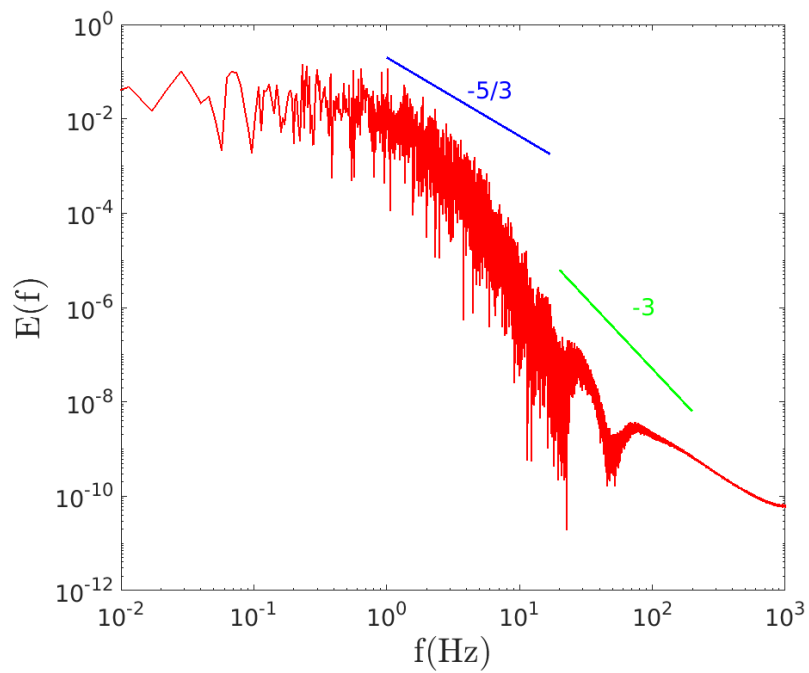
(b)
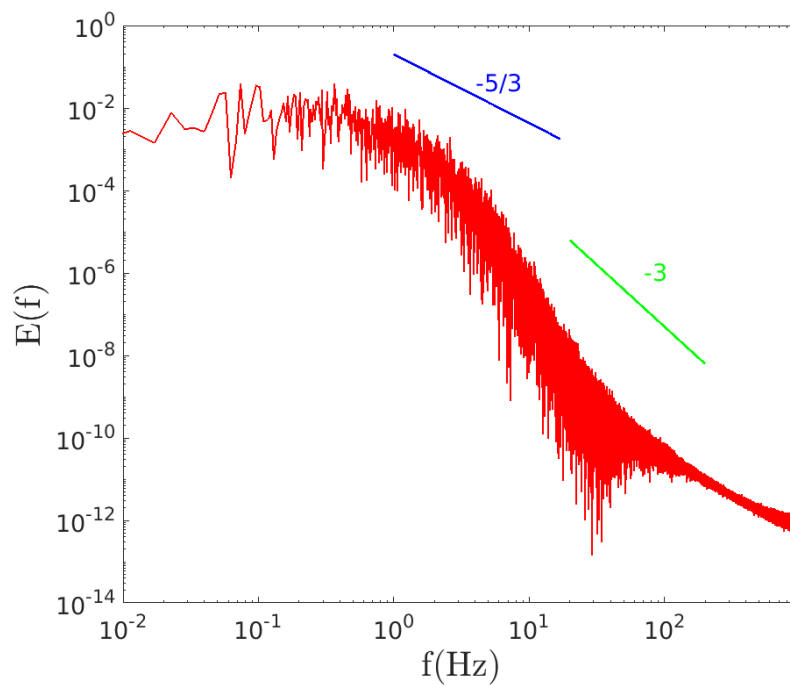
Fig. 4.12 Power spectrum density of radial liquid velocity (a) and axial liquid velocity (b) at $U_G = 6.0$ cm/s.

(a)

(b)
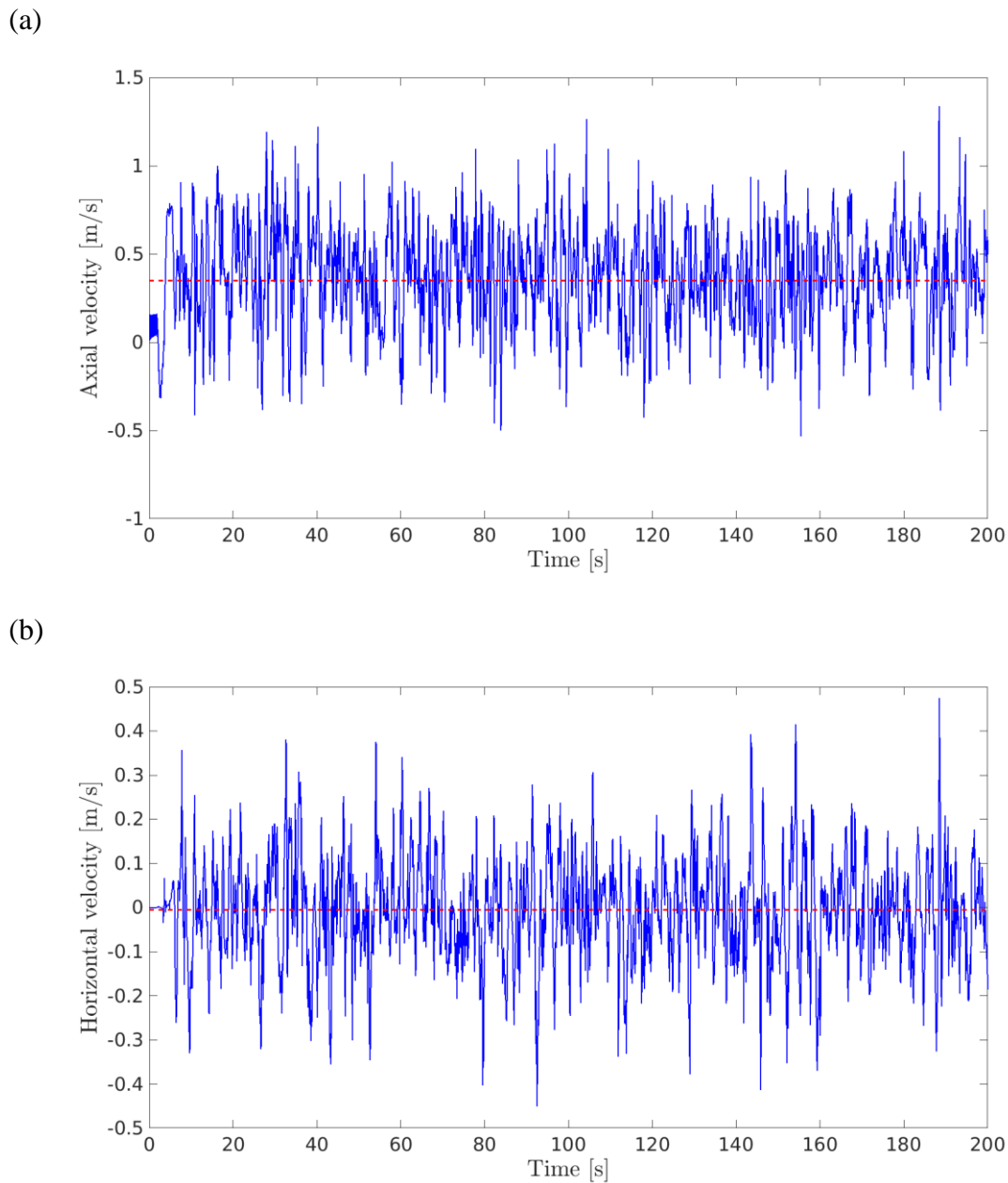
Fig. 4.13 Time history of the axial liquid velocity (a) and radial liquid velocity (b) with one-equation SGS model at the centerline of the column, at a height of $z = 0.7$ m $U_G = 8.4$ cm/s.

94

(a)
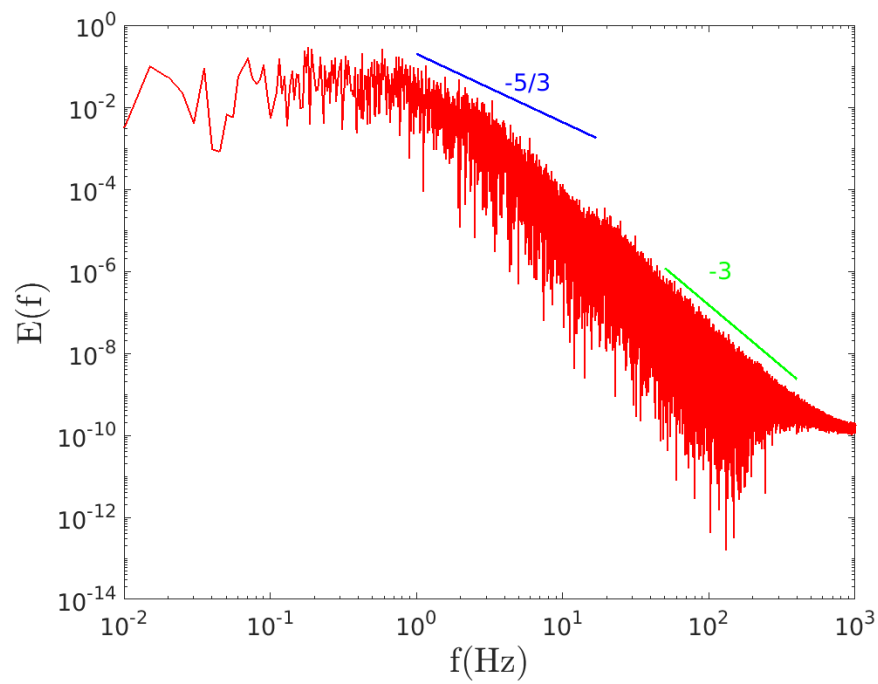
(b)
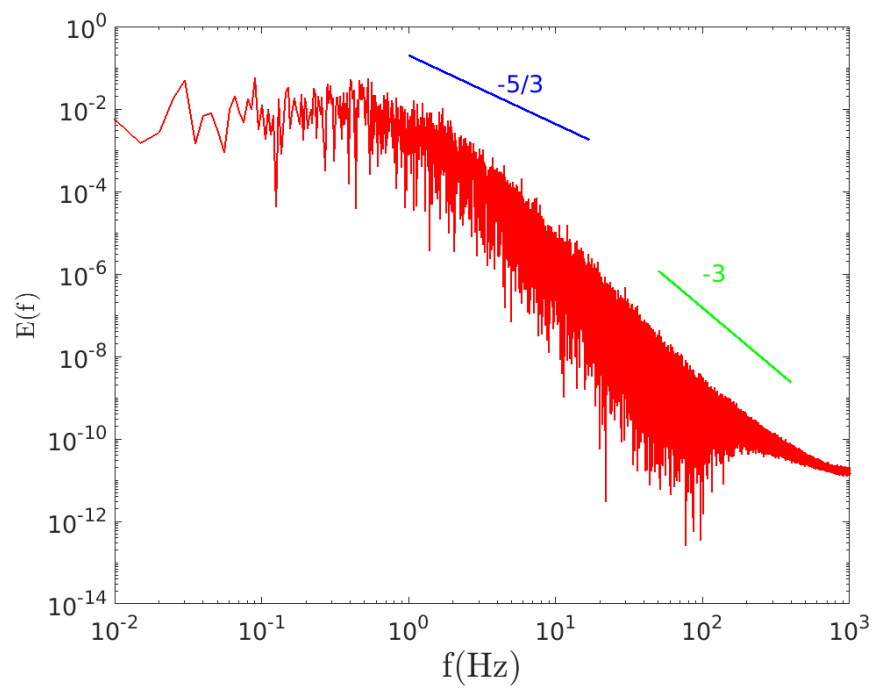
Fig. 4.14 Power spectrum density of the axial liquid velocity (a) and the radial liquid velocity (b) at $U_G = 8.4$ cm/s.

Chapter 5

Transient large-scale two-phase flow structures in a 3D bubble column reactor

This section analyses the local and time-dependent behavior of large-scale structures responsible for liquid circulation in gas-water flow of a 3-D cylindrical bubble column of high aspect ratio with a multiple orifice for uniform aeration. The large-scale flow structures play an important role in the mixing and the mass transfer while coherent structures dominate hydrodynamic characteristics of the turbulent flow field. A three-dimensional Euler-Euler large eddy simulation (LES) model was used to calculate large-scale structures and their interaction with bubbles at inlet superficial gas velocities of $U_G = 6$ and 8.4 cm/s where vortical-spiral and turbulent flow regimes occur. The two-phase model gives good agreements with experimental measurements. We use a conditional sampling procedure of liquid velocity and gas hold-up time series to identify and educe the development of coherent flow structures which consists in a pair of counter-rotating vortices convected in a staggered pattern along the column in both the vortical-spiral and central plume regions. On average, the detected instantaneous events for each template account for about 12-15 % of the data recorded and may appear simultaneously. These events produce important fluctuations in the axial liquid velocity and gas void fraction. The sampling procedure yielded the averaged topology of the three-dimensional large-scale structures which was visualized using iso-surfaces of the vorticity for different gas flow rates. The structures have spiral tube-shaped topology rotating along the column near the walls with a pair of counter-rotating cells sustained through the flow. This work provides deep insights into turbulent flow field in gas-liquid bubble column by LES and pattern recognition.

5.1 Introduction

Bubble columns are gas-liquid and gas-liquid-solid reactors used in many chemical, biotechnological and pharmaceutical industries, and other multiphase processes due to their effective mixing as well as mass and heat transfer characteristics between different phases at comparable energy consumptions relative to stirred-tanks vessels (Joshi 2001, Sokolochin et al. 2004, Mudde 2005, Jakobsen et al. 2005, and Vial and Stiriba 2013). In bubble column reactors, the gas phase is dispersed in the form of tiny bubbles in a continuous liquid phase using a gas distribution device. The flow pattern depends on many operating conditions such as the geometry, the gas distributors that control how the gas is spatially distributed and determines the primary bubble size distribution, and the gas flow rate that governs the flow regime. Furthermore, the complex interplay between operating conditions, the presence of turbulence and bubble-bubble interactions lead to extensive range of flow regimes and complex flow structures which dominate the hydrodynamic characteristics of the flow. Therefore, it is important to get a thorough understanding of the instantaneous flow structures.

Modelling of multiphase flows has been the subject of many research works and generally builds on two-fluid model, see Ishii and Hibiki 2006. It can be numerically investigated by various methods. For practically complete knowledge of the flow parameters, it is desirable to implement the DNS approach which would provide the highest resolution of the flow field around bubbles and has no dependence on modelling. However, the computational cost scales with the Reynolds number and the DNS places a large demand on computational resources (memory requirements and CPU time) on modelling large bubble column reactors. Therefore, one of the possible alternatives is to use the Euler-Euler two-fluid model coupled with the Reynolds-averaged Navier-Stokes (RANS) models or the Large Eddy Simulation (LES) models. The RANS models have performed satisfactory in many flow problems and can predict average flow field reasonably well

(Mudde and Simonin 1999, Deen et al. 2001, Selma et al. 2010, Ekambara and Dhotre 2010, Masood et al. 2014), but their applicability is limited since the flow in the bubble column is anisotropic and exhibits large scale vortical structures. The LES models can be regarded as valuable and successful tools to predict flows dominated by large transient structures and permit the bubble to interact with eddies of at least the same size (Deen et al. 2001, Milelli 2002, Tabib et al. 2008, Dhotre et al. 2008, Liu and Li 2018). They offer the possibility to resolve the large scales of motion which carry most of the flow energy, while the small scales are modelled with a subgrid-scale (SGS) model. Furthermore, the LES approach is less dependent on modelling and can capture more dynamics compared to RANS models, see Dhotre et al. 2013, Zhang et al. 2006, Tabib et al. 2011.

The aim of this work is to use a conditional sampling technique based on database of LES in a 3D cylindrical bubble column reactor to extract the topology of different flow structures. The LES approach has a drawback, since the largest interface details should be smaller than the grid size for the sake of consistency. This means that the grid cell size must be larger than the bubble size and a lot of details move to SGS level in particular the bubble-induced turbulence (BIT). The effect of sub-grid scale eddies on the turbulent dispersion force is another issue that has to be incorporated in interfacial force modelling. The Smagorinsky model and the dynamic Samgorinsky model were used in many works, see for instance Zhang et al. 2008, and Ma et al. 2015, but are not able to provide explicit information of the modelled sub-grid scale. Niceno et al. 2008 proposed to employ the one-equation SGS kinetic energy LES (Davidson, 1997) to gas-liquid flows, and obtained superior results to Smagorinsky model and the dynamic model. They added a source term to the transport equation for the SGS turbulent kinetic energy to model the BIT more accurately. Furthermore, they pointed out the possibility to use information on SGS kinetic energy to quantify the SGS turbulent dispersion force. Tabib et al. 2011 use the one-equation SGS model to analyse such force on different particle systems, namely the gas-liquid bubble column and the liquid-liquid pump mixer. Therefore, the one-equation model was adopted in this work and has shown to be accurate and computationally less demanding than the RANS model.

The flow structures in bubble column reactors are characterized by the development of a spectrum of structures for transition and heterogeneous flow regimes and have been extensively studied in the published literature. For instance, Chen et al. 1994 reported that as we increase the inlet gas flow rate clusters of bubbles travel through the column center carrying the liquid in almost a spiral rotating movement and small bubbles spirally downward in the near-wall region. The general macroscopic flow structure in vortical-spiral flow regime for 3D bubble column is shown in Fig. 5.1 based on measurements and observations of Chen et al. 1994. As we increase the inlet superficial gas velocity the intensity of turbulence destroys the vortical and spiral structures leading to turbulent flow structures. In Joshi et al. 2002, an overview over different resolving simulations of various flow patterns is provided with a classification of different circulation cell representations as schematically shown in Fig. 5.2. For instance, the averaged flow pattern can be represented as a single cell liquid recirculation, see Fig. 5.2(a). Here we observe that the instantaneous macroscopic structures were lost when the information was time averaged. Joshi and Sharma 1979 and Joshi 1992 pointed out different instantaneous flow structures of non-interacting cells and interacting cells with considerable inter-circulation as depicted in Fig. 5.2(b)-(c) and Fig. 5.2(f) respectively. The later occur for high bubble column diameters and superficial gas velocities in the range of 19-92 mm/s. Another model of multiple circulation cells which span the entire column was considered and observed by several authors, see for instance Zehner 1992 and Chen et al. 1989, or staggered circulation cells by Jamilahmadi et al. 1989 when the aspect ratio H/D exceeds some limit, see also Fig. 5.2 (d)-(e).

The large-scale liquid circulation, vortical structures and their behavior are complex. Their range of existence depends mainly on the bubble column aspect ratio H/D, where H is the height and D is the width, the gas distribution type, the initial gas flow rate and the liquid properties. These flow patterns were found at different superficial gas velocities in Mudde et al. 1997, Mudde and van den Akker 1999, Chen et al. 1994, Harteveld et al. 2003, Sathe et al. 2011 and Sun et al. 2012. Furthermore, the significant amount of computational work has been done to reproduce numerically

the liquid circulation and coherent structures that were found experimentally, see the works of Lapin and Lübbert 1994, Harry Van Den Akker 1998, Sokolichin et al. 1997, Bauer and Eigenberger 1999, and Simiano and Lakehal 2012. The largest flow structure (large eddy in the column) has a maximum size of the order of the column diameter, affects the local turbulence and can enhance the local transport phenomena, see Sathe et al. 2011. However, the role of uniform aeration in the dynamics of large-scale structure at high superficial gas velocities is still poorly understood.

As pointed by Simiano and Lakehal 2012, the large-scale events (the bubble plume and plume meandering) are not necessary part of turbulence but they are part of the fluctuation velocity components. Therefore, the time series of the liquid velocity and the gas hold-up were employed to identify and educe the development of coherent flow structures. The contribution of each event was determined by analyzing the cross-correlation coefficient map. These events produce important fluctuations in the axial liquid velocity and gas void fraction. The procedure yielded the averaged topology of the three-dimensional large-scale structure events and was visualized using iso-surfaces of the vorticity for different gas flow rates. The structures have spiral tube-shaped topology rotating along the column near the walls with a pair of counter-rotating cells sustained through the flow. This work indicates that LES with the present pattern recognition can provide deep insights into developments of dynamics large-scale flow structures in turbulent flow field in gas-liquid bubble columns.

5.2 Two fluid model and numerical setup

5.2.1   *The flow equations*

The two-fluid model is based on the spatial filtering for LES or conditional averaging for RANS of the conservation equations of mass and momentum, where both phases, the continuous liquid phase and the dispersed gas phases, are modelled as two interpenetrating continua, see Ishii

and Hibiki 2006. The filtered equations are used to compute the large-scale lengths while the unresolved turbulent scales are modelled using a sub-grid model.

The present formulation closely follows the procedure outlined by Weller et al. 1998 and Weller 2005, where the mass and momentum equations for the phase φ are given by

$$\frac{\partial\left(\rho_\varphi \alpha_\varphi\right)}{\partial t} + \nabla \cdot \left(\rho_\varphi \alpha_\varphi \mathbf{U}_\varphi\right) = 0 \tag{1}$$

$$\frac{\partial\left(\rho_\varphi \alpha_\varphi \mathbf{U}_\varphi\right)}{\partial t} + \nabla \cdot \left(\rho_\varphi \alpha_\varphi \mathbf{U}_\varphi \mathbf{U}_\varphi\right) = -\alpha_\varphi \nabla p_\varphi + \alpha_\varphi \rho_\varphi \mathbf{g} - \nabla \cdot \left(\alpha_\varphi \rho_\varphi \boldsymbol{\tau}_\varphi^{\mathrm{eff}}\right) + \mathbf{M}_\varphi \tag{2}$$

Here α_φ is the volume fraction of each phase, $\mathbf{U}_\varphi$ is the phase grid-scale velocity, and $\tau_\varphi^{\mathrm{eff}}$ represents the combined mean viscous stress and turbulent stress tensor of phase φ

$$\boldsymbol{\tau}_\varphi^{\mathrm{eff}} = -\nu_\varphi^{\mathrm{eff}}\left[\nabla\mathbf{U}_\varphi + \left(\nabla\mathbf{U}_\varphi\right)^T - \frac{2}{3}(\nabla \cdot \mathbf{U}_\varphi)\mathbf{I}\right] + \frac{2}{3}k_\varphi\mathbf{I} \tag{3}$$

where k_φ is the turbulent kinetic energy of phase φ, $\mathbf{I}$ is the identity tensor, and ν_φ^{eff} is the effective viscosity of phase φ. The effective viscosity of the liquid phase is the sum of the molecular viscosity and the sub-grid viscosity

$$\nu_\varphi^{\mathrm{eff}} = \nu_{L,\varphi} + \nu_{SGS} \tag{4}$$

and is formulated in the present study using the one-equation sub-grid-scale model by Niceno et al. 2008. The SGS model solves an additional transport equation for the unresolved kinetic energy k_{SGS}. The model of Niceno et al. 2008 accounts for effects of bubble induced turbulence through an additional source term in the transport equation for k_{SGS} in the continuous phase. The sub-grid kinetic energy equation reads

$$\frac{\partial k_{SGS}}{\partial t} + \nabla \cdot (k_{SGS}\mathbf{U}) - \nabla \cdot [(\nu + \nu_{SGS})\nabla k_{SGS}] = G - C_\varepsilon \frac{k_{SGS}^{3/2}}{\Delta} \tag{5}$$

where G is the production term, defined as follows

$$G = \nu_{SGS}|\bar{S}_{ij}| \tag{6}$$

and the sub-grid viscosity is

$$\nu_{SGS} = C_k \Delta k_{SGS}^{1/2} \tag{7}$$

The model constants are $C_\varepsilon = 1.05$ and $C_k = 0.07$, see Davidson 1997.

In Eq. (2), $\mathbf{M}_\varphi$ represents the inter-phase momentum exchange between phase φ and the other phase due to various interphase forces. In this study, the interfacial forces are decomposed into contributions from the drag, lift, virtual mass and turbulent drag which accounts for additional drag due to fluctuations in the dispersed phase. The total interfacial force acting between the two phases is given as

$$\mathbf{M}_\varphi = \mathbf{M}_\varphi^D + \mathbf{M}_\varphi^D + \mathbf{M}_\varphi^{VM} + \mathbf{M}_\varphi^{TD} \tag{8}$$

The terms on the right-hand side of Eq. (8) are

$$\mathbf{M}_\varphi^D = \frac{3}{4}\alpha_\varphi \rho_L \frac{C_D}{d_b}|\mathbf{U}_r|\mathbf{U}_r \tag{9}$$

$$\mathbf{M}_\varphi^L = \alpha_\varphi \rho_L C_L \mathbf{U}_r \times (\nabla \times \mathbf{U}_r) \tag{10}$$

$$\mathbf{M}_{\varphi}^{VM} = \alpha_{\varphi}\rho_L C_{VM}\left(\frac{D\mathbf{U}_c}{Dt} - \frac{D\mathbf{U}_d}{Dt}\right) \tag{11}$$

$$\mathbf{M}_{\varphi}^{TD} = -C_{TD}\rho_L k_L \nabla\alpha_G \tag{12}$$

Here $\mathbf{U}_r = \mathbf{U}_L - \mathbf{U}_G$ is the relative velocity between the continuous and the dispersed phases. The interfacial coefficients C_D, C_L, C_{VM} and C_{TD} are the drag, lift, virtual mass, and turbulent dispersion coefficients, respectively, which must be obtained from empirical correlations or analytical models. There are many models for each of these forces or coefficients depending on their applicability, the flow regime and operating conditions as discussed by Joshi, 2001 and Vial and Stiriba, 2013. The SGS component of those forces will be neglected except in the turbulent dispersion force which can be estimated using the modelled SGS energy. The drag coefficient was determined according to Schiller-Naumann correlation, the added mass coefficient C_{VM} is fixed to 0.5. The lift force which has been found to reproduce the radial dispersion of bubbles, as already pointed out by several authors, is justified for single bubble but for bubble swarm the uncertainty still remains. It is found that the simulations without considering the lift force best matches the experimental data. The sub-grid-scale turbulent dispersion force is adopted for the coarser and medium meshes since the grid sizes are relatively larger than the bubble size, see Lopez de Bertodano et al. 1994, Niceno et al. 2008 and Tabib et al. 2011.

5.2.2   Numerical simulation set-up

The numerical simulations were carried out in a cylindrical bubble column with uniform aeration. The bubble column reactor is the same as used by Vial et al. 2000 and Vial et al. 2001(a)-(b) in their experiments. The height of the column is $H = 2$ m, the diameter is $D = 0.10$ m, and the static liquid height is 1.5 m. The reactor is operated with the water and air as the continuous and dispersed phases, at room temperature and atmospheric pressure, respectively, at two large

superficial gas velocities 6 cm/s and 8.4 cm/s corresponding to transition and heterogeneous flow regimes.

The numerical simulations were carried out with the open source CFD package Open-FOAM library (Weller et al. 1998 and Open-FOAM user guide). The governing equations of continuity and momentum as well as the transport equation for k_{SGS} are solved by the two-phase flow solver twoPhaseEulerFoam available in Open-FOAM v.4.0.0. The solver is based on a finite volume formulation to discretize the model equations which has shown to be stable for transient calculations, see Weller 2005. The first-order bounded implicit Euler scheme is adopted for the time integration, the gradient terms are discretized with a linear interpolation, the first-order upwind scheme for convective terms, and the diffusive terms are interpolated with the Gauss linear orthogonal scheme. we employ the PIMPLE algorithm to solve the pressure-velocity coupling where the pressure equation is solved, and the predicted velocities are corrected by the pressure change. The preconditioned conjugate gradient (PCG) is used for solving the discretized pressure equation and the incomplete-Cholesky preconditioned bi-conjugate gradient (BICCG) is used for other set of linear equations. For a more detailed discussion of all steps mentioned above, see Rusche 2002, Selma et al. 2010, and Weller 2005. The gas distributor is treated as a uniform mass flow rate inlet calculated from superficial gas velocities for mass conservation with a gas volume fraction of 1.0. The pressure at the inlet is set to zeroGradient and specified by zero gradient. At the outlet, the pressure is specified as atmospheric pressure, and the gas hold up is set to inletOutlet where zero gradient for outflow and fixed value for backward flow. Along the walls, no-slip conditions were applied.

For the present Euler-Euler LES approach, we have to consider the resolution requirement of both LES and the Euler-Euler approach simultaneously in order to choose a satisfactory grid. For the Euler-Euler model, the cell size should be larger enough than the largest interphase details of dispersed phase. In LES, the mesh has to be fine to resolve as much of the flow field as possible. According to Dhotre et al. 2013 and Zhang et al. 2008, a successful LES must have a filter width

104

in the initial subrange region, and all scales of motion larger than that must be resolved on the numerical grid. They indicated that the bubble diameter must be smaller than the cell size. Milelli et al. 2001 reported a systematic posterior analysis of the ratio of the bubble diameter to cut-off filter size: $\Delta/d_B \geq 1.5$, that is the mesh size must be at least 50% larger than the bubble diameter for Eulerian-Eulerian simulations. In the present case, the computational mesh was generated using the Gmsh finite element mesh generator. In order to check that the computed results are grid-independent, four different grids with $d_B/\Delta = 0.75, 1.1, 1.4$ and 1.875 (see Table 5.1), have been analyzed by stretching the computational cell size near the walls. The coarser and medium mesh satisfy the Milelli condition, while the fine mesh does not. Fig. 5.4 shows the comparison of the axial liquid velocity and the gas hold-up. All the meshes show very similar results. In this work, we have employed the medium mesh with a filter width $\Delta = 5$ mm ($\Delta/d_B = 1.1$) which quantitively seems to give better agreements and ensures a good compromise between the CPU time and accuracy at the column center and close near the walls.

Note that for comparison, Niceno et al. 2008 used the criterion $\Delta/d_B = 1.2$ and found no significant different with different meshes, and the coarser one satisfying Milelli condition give a better agreement, Dhotre et al. 2008 found good agreement with experimental data using both conditions $\Delta/d_B = 1.2$ and $\Delta/d_B = 2.5$, and Liu et al. 2018 used the criterion $\Delta/d_B \leq 1.0$ and concluded that the grid size doesn't have to be larger than a single bubble size.

All transient calculations are started from static conditions with the liquid at rest and the gas is injected with a mass flow rate corresponding to the experimental superficial gas velocity. The bubble diameter is kept constant at 4 mm according to the experiments of Vial et al. 2001. Bubble coalescence and breakup are not considered in this work. We start with a fixed small-time step of $\Delta t = 0.0005$ s for the first 20 s then we increase it to 0.001 s in order to account for the transient instabilities of bubbly turbulent flows and satisfy the CFL condition $Co = \Delta t |\mathbf{U}|/\Delta x < 1$, where $|\mathbf{U}|$ is the magnitude of the velocity through a computational cell and Δx is the cell size in the

direction of the velocity. The flow was simulated for 200 s and the averaged results from t = 50 s to t = 200 s are quantitively compared with experimental data. All the simulations were performed in parallel mode on a PC cluster with 16 nodes, Intel Xeon, 2.8 GHz, 4GH RAM.

5.3 Data processing and conditional sampling

LES and DNS methods provide fluid dynamics with data bases that use extended time series to give more details about the high intensity turbulent flows. Different methods to analyze those larger data efficiently and identify coherent structures were developed. For instance, the proper orthogonal decomposition (POD), the dynamic mode decomposition (DMD), the coherent structure simulation (CVS), the fuzzy clustering technique, or the pattern recognition technique (PR). The second author gave a summary of different techniques used by different authors in references Usera et al. 2006 and Vernet et al. 1999.

The conditional sampling of the imprints on the plane of symmetry due to large flow structures, responsible of the circulation flow pattern in the bubble column, is performed by recording when the flow was statistically fully developed the time evolution of the instantaneous liquid velocity and gas hold-up in the computational domain during 0.5 s. The large-scale events (the bubble plume and plume meandering) are not necessary part of turbulence but they are part of the fluctuation velocity components (Simiano and Lakehal 2012). Therefore, time series of the liquid velocity and gas hold-up are needed to detect the flow structures responsible of their extreme values. The conditional sampling involves cross-correlating an initial template $\mathbf{U}_L(\mathbf{x}, t)$ with the liquid velocity data $\mathbf{U}_L(\mathbf{x}, t + \tau)$ sampled during the simulation. The cross-correlation is given by

$$R(\tau) = \frac{\overline{\mathbf{U}_L(\mathbf{x}, t) \, \mathbf{U}_L(\mathbf{x}, t + \tau)}}{\overline{\mathbf{U}_L(\mathbf{x}, t)^2}} \tag{13}$$

The overbar indicates an average over $\mathbf{x}$ and t.

The conditional pattern recognition technique used is based on the detection of extreme values of the correlation coefficients in the plane of symmetry of the column. Fig. 5.3 shows the main steps of the conditional sampling technique procedure. As indicated in step 2 of Fig. 5.3, the cross-correlation coefficients of an initial template of the liquid velocity are stored in a three-dimensional matrix (i.e., two-dimensional matrix for each time step). The different templates used to detect the coherent structures consists of different multiple circulation cells and their selection will be discussed in the next section. Values of the cross-correlation coefficient larger than a threshold level (selected here to be the 1.5 times the *rms* value of the cross-correlation) identify the occurrence of individual events similar to the template. These events are ensemble averaged with the current ensemble average being used as the template for the next iteration. This procedure is repeated until the new template (i.e. ensemble average) is equal to the penultimate template. The time evolution of the spatial distribution of the liquid velocity produces that regions where the maximum of the correlation coefficient appears. The positions and the time at which the selected events occur are stored in a file, and then we use this information to obtain the conditional ensemble averaging of the flow at the plane of symmetry in the reactor.

The regions where the maximum of the correlation coefficients occur are selected as elongated volumes since the extreme values move along the stream-wise and span-wise directions. In these volumes, only region of the plane corresponding to time where the absolute maximum of the correlation occurs is chosen to obtain the ensemble average of the liquid velocity event. In this way, the procedure will prevent selecting different stages of the same event at different times. The present technique resembles that applied by Pallares et al. 2010 in natural convection vertical channel flow. Similar pattern recognition procedure was used by Vernet et al. 1999 to analyze three-dimensional structures in a turbulent cylinder weak. The information obtained is employed to calculate the vorticity when and where the selected event occurs.

5.4 Results and discussions

Fig. 5.5 and 5.6 show a comparison between numerical simulations using both the $k - \varepsilon$ model and the LES against experimental measurement of Vial et al. 2001 for the mean axial liquid profile and axial fluctuating liquid velocity, respectively. It can be seen that the models capture experimental data reasonably well in both flow transition regime ($U_G = 6$ cm/s) and heterogeneous flow regime ($U_G = 8.4$ cm/s). In the core region, $x/R \leq 0.9$, both models give nearly the same results. For the initial superficial gas velocity $U_G = 6$ cm/s, the Euler-Euler LES approach gives a better agreement with experimental data both in the core region and close near the wall. In Fig. 5.6 we display the time averaged *rms* axial liquid velocity calculated by LES and RANS model. We can see clearly that LES performs better than RANS. Unfortunately, experimental data on kinetic turbulent energy of the liquid phase are not available. In fact, Vial et al. 2001 only measured the *rms* in the axial and orthoradial directions. For $U_G = 8.4$ cm/s, however, the liquid velocity is over-predicted at high superficial gas velocity between the central plume region and the vortical flow region. The reason of this deviation as the performance of LES with respect to RANS are not clarified and may be attributed to the single bubble size distribution of 4 mm using in our two-phase flow model and the interfacial forces employed. In this region the flow is characterized by cluster of bubbles at relatively low velocities and coalesced bubbles moving at high velocities, see Chen et al. 1994. Furthermore, we found that the RANS model performs better with inclusion of the turbulent dispersion force which spreads the bubble plume. While the trend in LES calculations is to neglect the unresolved sub-grid scale, we found that such interfacial sub-grid-scale force improves the liquid velocity profile as Tabib et al. 2011 who quantified the SGS-TDT and found that, for the bubble column reactor, its magnitude is small as compared to the momentum advection, the drag and resolved turbulent dispersion forces. They pointed the need of research works towards finding suitable SGS-TD force model.

Note that for comparison, Zhang et al. 2008, simulated different bubble column reactors with different aspect ratios employing a sub-grid scale model and the $k - \varepsilon$ model and different interfacial closure correlations. They found that both models can produce a good solution for the time-averaged vertical velocity and there is not yet a universal interfacial closure model available for the simulation of the bubble column flow.

Typical time series of the axial liquid velocity components at height of 0.7 m are depicted in Fig. 5.7 and show the transient behavior and statistically stationary with constant mean velocity. The energy spectrum density obtained from LES calculations is shown in Fig. 5.8. It can be seen the classical -5/3 law holds at the initial superficial gas velocity of $U_G = 8.4$ cm/s and deviates slightly at $U_G = 6$ cm/s in the initial subrange. Previous experimental and numerical studies attributed this fast decay and the more dissipative spectrum to buoyancy-generated inertia forces and the bubble-induced viscosity effects, see Dhotre et al. 2008 and Lance and Bataille 1991. Both spectra consist on numerous dominant peaks in the 0-120 Hz frequency band and exhibit several peaks, for example 15 and 35 Hz at $U_G = 8.4$ cm/s and 40 and 60 Hz at $U_G = 6$ cm/s which indicate the transient behavior of the system. Indeed, the low frequencies are never observed. Both flow regimes are characterized by existence of liquid flow circulation pattern and thus macro-structures in both phases that move alternatively upwards and downwards as observed numerically in this work and experimentally by several authors, see Vial et al. 2001 and Olmos et al. 2003. This corresponds to quasi-periodic phenomena that induces high velocities fluctuations and new frequencies.

In Fig. 5.9, the time-averaged and selected instantaneous snapshots of liquid velocity fields with the corresponding gas hold-up are displayed at times 70, 80 and 90 s, respectively. The LES resolves the flow with much more details as reported by Deen et al. 2001 and Dhotre et al. 2008. Large vortices can be observed in the column center and some circulations in the near-wall region. The flow pattern changes with time and large amount of the gas moves through the central plume region and deviates from the flow characteristics obtained by time-averaging. As can be seen a

bubble plume structure starts from the distributor zone up to the free surface and becomes much pronounced with high inlet gas flow rate. Several liquid circulation cells are continuously generated and convected throughout the column height. Their number and size are changes with time and the inlet superficial gas velocity. The same vortices were observed by Chen el al. 2004 through flow visualization using laser sheeting and PIV system for the gas velocity between 2.1 and 4.2 cm/s. They found the general flow pattern displayed in Fig. 5.1(a). They reported existence of different large flow structures under different flow regimes, see for example Fig. 5.1(b). For the vortical-spiral flow regime, clusters of bubbles form in the central bubble stream moving in a spiral manner with the liquid moving spiraling downward close to the wall column, see Fig. 5.2. Here we observe the existence of four instantaneous regions. Joshi et al. 2002 pointed out existence low-frequency circulation cells in both 2D and 3D bubble column reactors and the potential of LES to simulate and explore the coherent structures. The onset, size, location and numbers of the circulation cells change instantaneously in the column.

By combining the information from the above discussion with visual observations on instantaneous liquid circulation patterns depicted in Fig. 5.9, a pair of non-symmetric circulation cells were identified and have been used as the initial templates to analyze the liquid velocity field recorded simultaneously with the gas hold-up and to detect where correlation coefficient attains extreme values, see Fig. 5.10. It consists of two staggered lobes of different positions observed at the plane of symmetry of the bubble column. Fig. 5.11 displays the autocorrelation function of axial liquid velocity at mid height of the column reactor for $U_G = 6$ cm/s and 8.4 cm/s, respectively. In both cases, the correlation coefficients present an exponentially decreasing shape and go to 0 for a delay of 5 s and then it starts to fluctuate above and beyond 0. Time evolution of 450 individual samples of the liquid velocity and gas hold-up at the plane of symmetry during a period of 200 s were used to educe the flow structures.

The number and position in the axial direction where the maximum of the correlation coefficient between the template and the detected event occurs are displayed in Fig. 5.12. At

superficial gas velocity $U_G = 6$ cm/s, an average of 79 and 66 events were selected for templates 1 and 2, respectively, with a correlation coefficient of 0.65. The flow structure of both templates is characterized by a fast bubble flow region including cluster of bubbles moving in a wavy spiral motion through the column with gross scale liquid circulation carried upward in the bubble stream and downward motions of liquid pockets in the vortical spiral flow region which still may include bubbles. This structure corresponds to churn-turbulent flow regime and was obtained experimentally through the PIV techniques in other 2D and 3D bubble column reactors by other authors. One can see that those macroscopic structures appear near the sparger and at different heights between 0.2 and 1 m. At superficial gas velocity $U_G = 8.4$ cm/s, the flow regime turns from vortical-spiral to turbulent and an average of 79 and 82 events were selected for templates 1 and 2, respectively, with a correlation coefficient of 0.65. The bubble velocities and turbulence intensity are enhanced along the column in both the fast bubble and the central plume regions and the vortexes are more stretched. Note that the structure number in this flow regime is much higher close to the sparger zone than in the spiral-vortical region. By comparing different pictures one can see that the two structures can occur simultaneously in more than 60 % but at different locations and then disappear near the free surface.

The conditionally ensemble averaged instantaneous liquid velocity components, gas hold-up and velocity field constructed with axial and streamwise liquid velocity components are shown in Fig 5.13 and 5.15. The weakness of (u, v) velocity field in comparison with the contribution of the axial velocity can be assessed. The streamwise velocity attains its maximum/minimum between the vortices and is symmetric in the selected plane, whereas the spanwise component corresponding to template 1 exhibits a minimum at the center of one circulation which nearly balanced by that at the other opposite circulation, that is, only v changes the sign. For the vortical structures of template 2, the v −velocity attains its maximum in each vortex. These changes of sign lead to movement of the vortical structure back and forth. Fig. 5.13(d) and Fig. 5.15(d) show the liquid flow fields with velocity vectors and contours of gas hold-up. The gas void fraction has the same trend as the axial

111

liquid velocity. The liquid flow is accelerated where more bubbles are located and decelerated with less bubbles. The bubbles are accumulated at the center of the plane and rise back or forth since the streamwise liquid velocity is very small.

In Fig. 5.14 we display the ensemble average of the fluctuation values. The magnitude of velocity fluctuations w' are higher than u' and v' which explain the anisotropy of the turbulence. The fluctuations of the axial velocity and gas hold-up peak at each cell vortex whereas u' peaks in the center. The nature of the fluctuations can be explained by the fact that the vortical structure move upward at the central part of the column and upward and downward close to the walls. The flow in this region experiences small fluctuations in the spanwise component of the liquid velocity leading v' to peak along the walls. The LES model predicts non-zero streamwise fluctuating velocities only at the center region of the column which accelerates the flow and force the bubble plume to meander only in this region. The trend of the void fraction fluctuations resembles that of the axial velocity fluctuations. It is clear that the bubbles induce a substantial turbulence both in central plume and fast bubble regions which gets stronger with increasing α'_G and show a peak in the vortical spiral region.

To further analyze the conditionally averaged flow structure responsible for the large vortical structures we use the vorticity vector calculated from instantaneous liquid velocity

$$\omega_x = \frac{\partial w}{\partial y} - \frac{\partial v}{\partial z}, \qquad \omega_y = \frac{\partial u}{\partial z} - \frac{\partial w}{\partial x}, \qquad \omega_z = \frac{\partial v}{\partial x} - \frac{\partial u}{\partial y}$$

and the magnitude $|\omega| = \left(\omega_x^2 + \omega_y^2 + \omega_z^2\right)^{1/2}$. A quantity used by Jeong and Hussain 1995 to detect the vortex cores and represent their topology and also by Simiano and Lakehal 2012 to analyze the mean flow filed in the bubble plume. The vorticity provides insights on the oscillatory behavior of the plume. Fig. 5.16(a)-(b) and 5.17(a)-(b) depict the lateral vorticity ω_y at the symmetry plane of the column and streamlines. The vorticity shows a complex radial distribution

with elevation: in the core region (0.04m $\leq x \leq$ 0.06 m), encompassing both the central plume and fast bubble region, ω_y is dominated by both $\partial u/\partial z$ and $\partial w/\partial x$ which reflects a flow retraction features to be discussed in the context of Fig. 5.15, and only by $\partial w/\partial x$ (i.e., $\omega_y \approx -\partial w/\partial x$) in the vortical-spiral region (0.07 m $\leq x \leq$ 0.1 m) which promote flow acceleration in the axial direction close to the walls, see Fig. 5.13. In fact, in the central plume region $\partial u/\partial z$ exhibits strong drop while $\partial w/\partial x$ remains small in some parts, and toward the walls $\partial w/\partial x$ has strong jumps meantime the streamwise velocity is very small. The rising bubbles have a two-dimensional zig-zag motion. It shows two lobes in the central plume region with inclined double roller structure and other two lobes in the vortical spiral flow region close to the walls. The vorticity magnitude is nearly equal in each lobe and the highest level occurs at the lower span-wise eddy. The focus of the primary vortices is located between the fast bubble region and the central plume region while the focus of the secondary vortices is shifted from the vortical spiral region to near wall by strong bubble backflow.

Three-dimensional plot of $|\omega|$ iso-contours are displayed in Fig. 5.16(c) and 5.17(c), the flow structure has spiral tube-shaped topology where swarm of bubbles rises along 3D helical trajectories around within the central bubble plume region. The plume rotates along the axial direction near the walls and the sharp edge corresponds to the peak of vorticity shown in Fig. 5.16(a)-(b) and Fig. 5.17(a)-(b). The flow structure responsible for liquid circulation convects the flow from the fast bubble plume region toward the walls. It seems that it doesn't cross the column via the centerline with an irregular rotation. This irregular movement is continuous for $U_G = 6$ cm/s and becomes faster for $U_G = 8.4$ cm/s but the shifting of the plume structure could be considered to be continuous and similar in both cases. A pair of counter-rotating cells are sustained through the flow and move spirally upwards while the bubble plume changes position which are found experimentally to entrain small bubble. The width of the plume is comparable with the column diameter and seems to fill the entire column. The picture is a schematic representation of the flow

structure in higher-aspect ratio bubble columns for both medium and high gas flow rate, as observed visually. The flow pattern displays a number of cells which move dynamically upward while the bubble plume changes position.

5.5 Conclusions

Database obtained from Euler-Euler large eddy simulations of the gas-liquid flow in a three-dimensional cylindrical bubble column has been analyzed to numerically investigate transient large flow structures associated with rising bubbles in a semi batch reactor. The sub-grid scale modeling is based in the one-equation model and the bubble-induced turbulence was modelled by extra source terms added in the transport equation for SGS kinetic energy. The initial superficial gas velocity is taken so that the flow is in the churn-turbulent flow regimes.

The instantaneous results of LES reveal that the flow pattern is dominated by vortical structures. Multiple low-frequency cells of different sizes have been observed in the vortical-spiral flow region. The averaged large flow structures are educed using a conditional sampling technique and they consist of two counter-rotating vortices that move in a wavy-spiral motion through the column. The cross-correlation coefficient maps were obtained. For one template a nearly 79 events were detected in the spiral flow regime and 82 events in the turbulent regime with a correlation coefficient of 0.65. The two flow structures can occur simultaneously in more than 60 % but at different locations. The procedure yielded the topology of the three-dimensional large-scale structure which was visualized using iso-surfaces of the vorticity for different gas flow rates. The structures have spiral tube-shaped topology rotating along the column near the walls with a pair of counter-rotating cells sustained through the flow. The trend of bubble induced turbulence resembles that of the void fraction. This study provides analysis of instantaneous flow information and pattern recognition of air-water flow which are crucial in further understanding hydrodynamics and flow transition of multiphase flow in bubble column reactors.

`	$\Delta x \times \Delta y \times \Delta z$ (mm^3)	Δ/d_B
Mesh 1	$7.5 \times 7.5 \times 7.5$	1.875
Mesh 2	$5 \times 5 \times 7$	1.4
Mesh 3	$5 \times 5 \times 5$	1.1
Mesh 4	$3 \times 3 \times 3$	0.75

Table 5.1. The computational mesh and grid spacing investigated.

(a)
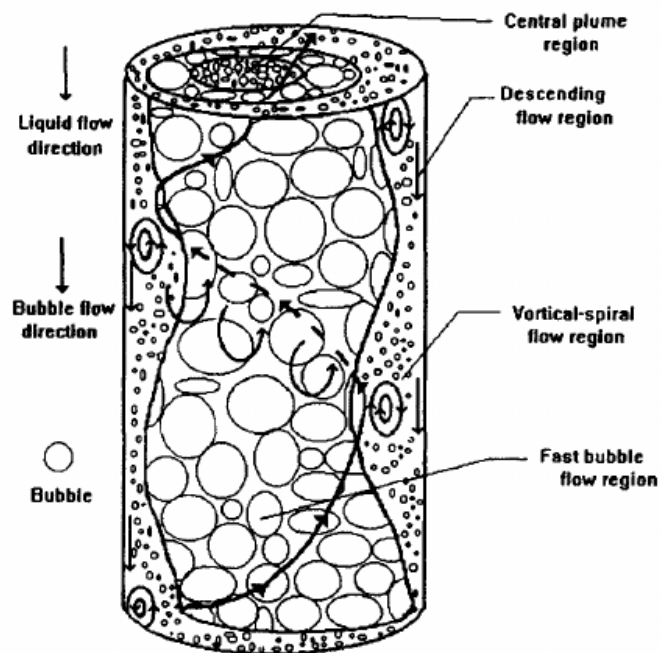
(b)
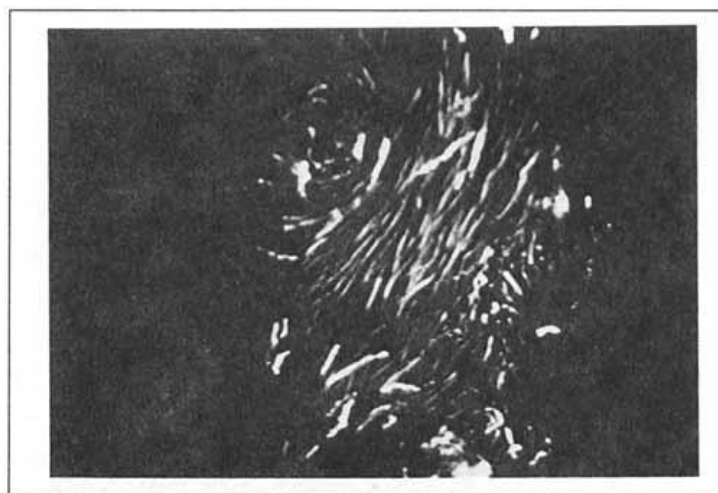
Fig. 5.1. (a) Instantaneous flow structure in a 3-D bubble column and (b) liquid flow field at $U_G = 3.3$ cm/s. (Chen et al., 1994).
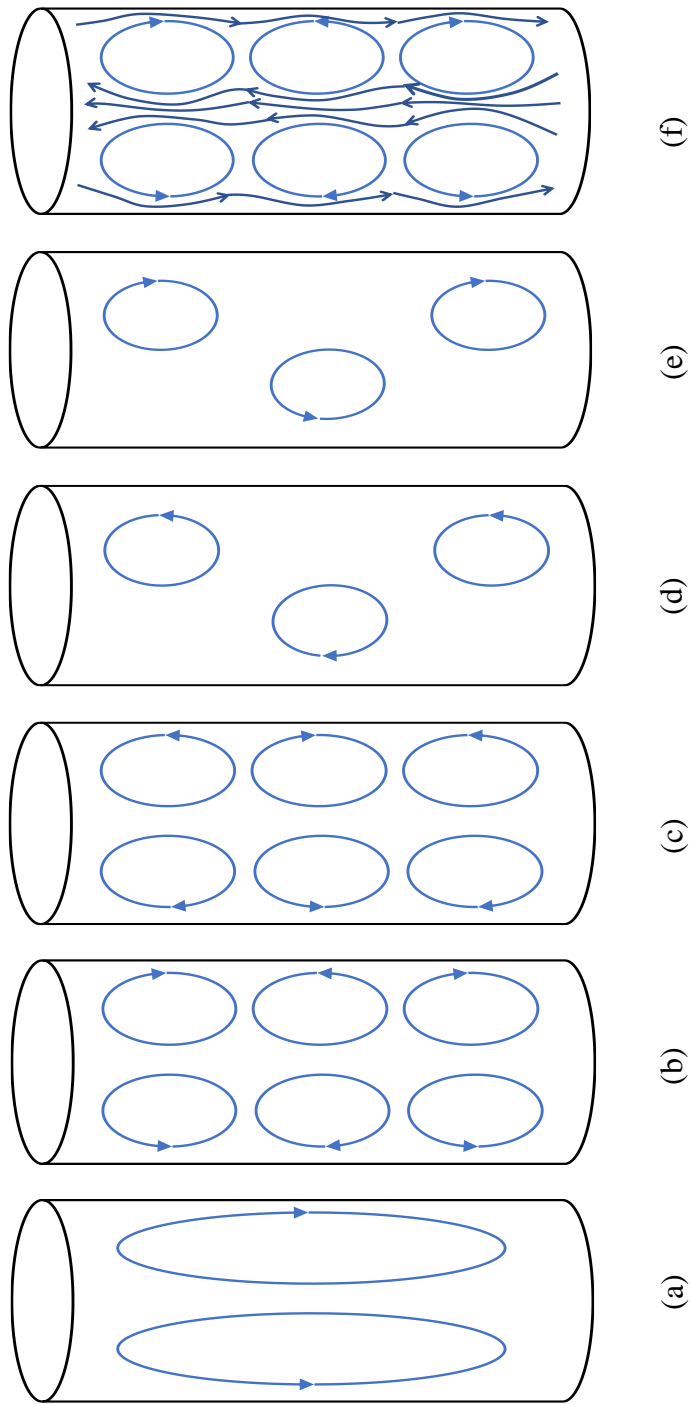
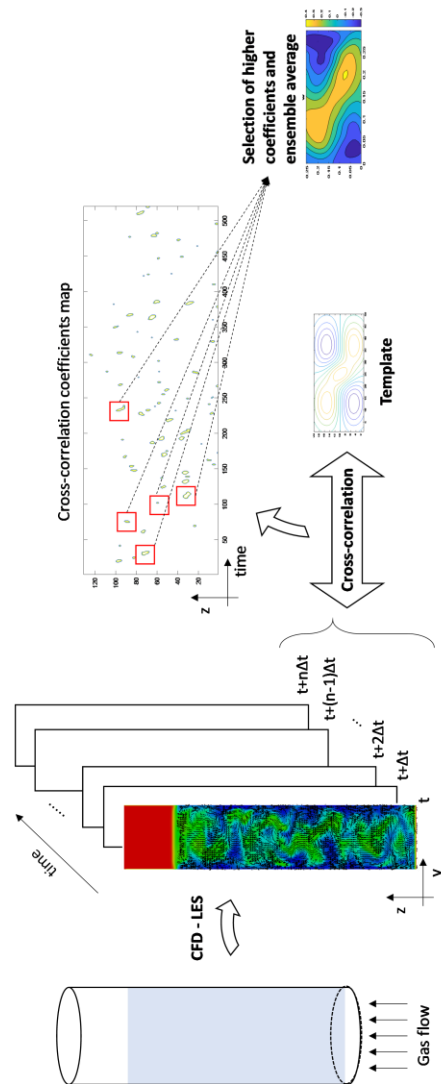**Fig. 5.2.** Different liquid circulation cell structures in bubble column

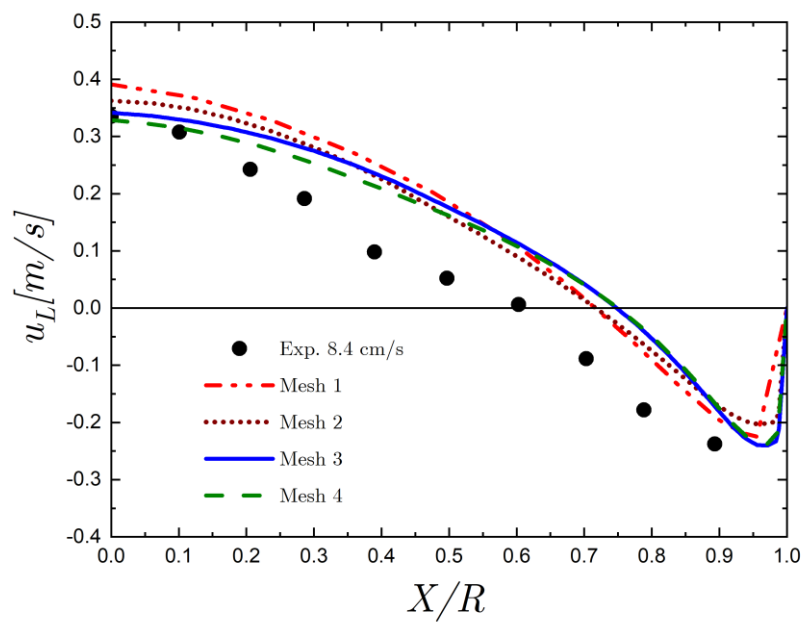**Fig. 5.3.** The different steps of the conditional sampling procedure

Fig. 5.4. Comparison of the time-averaged results for the axial liquid and the different meshes investigated at $U_G = 8.4$ cm/s.
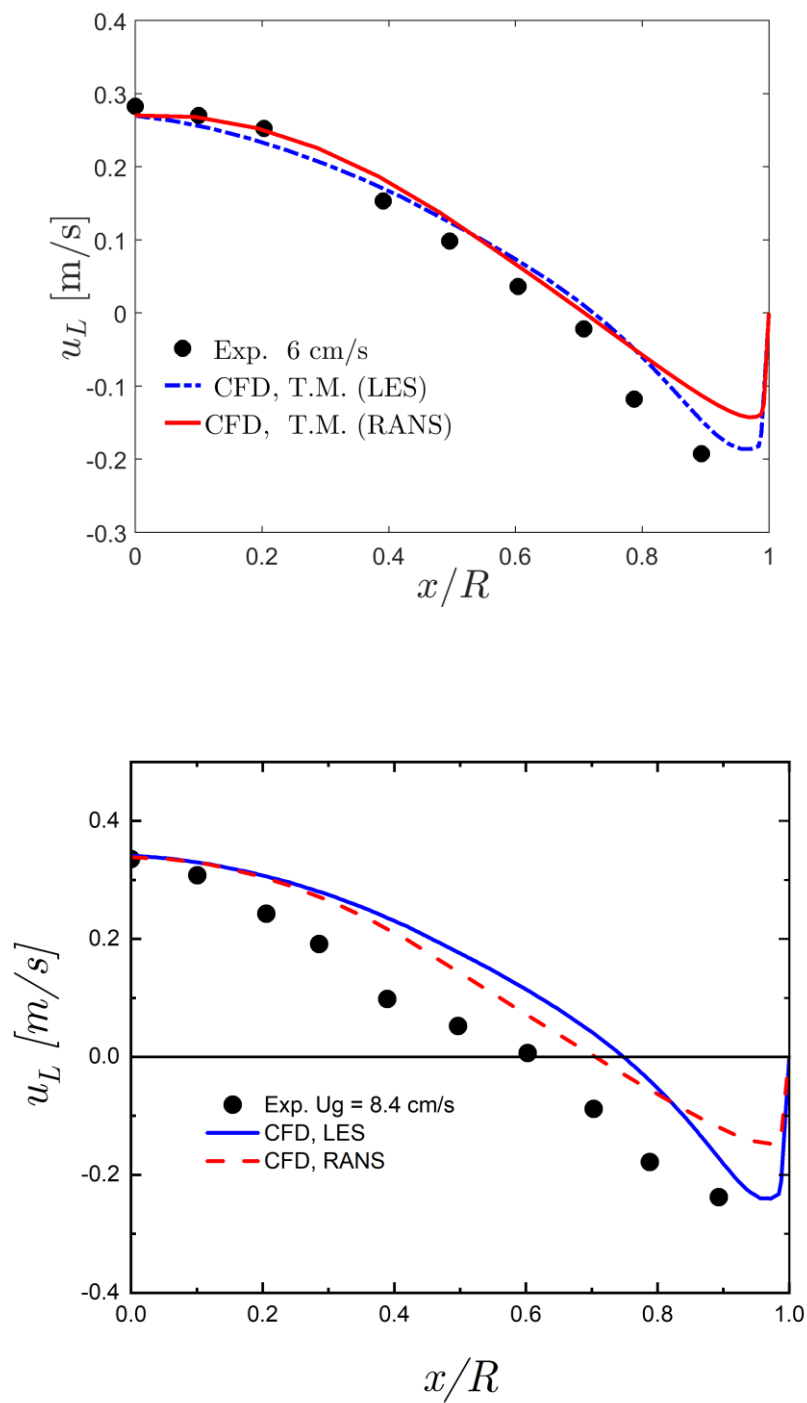
Fig. 5.5 Comparison of the calculated time averaged axial liquid velocity with experimental measurements at the height $h = 0.7$ m with mixture $k - \varepsilon$ and one-equation LES models.
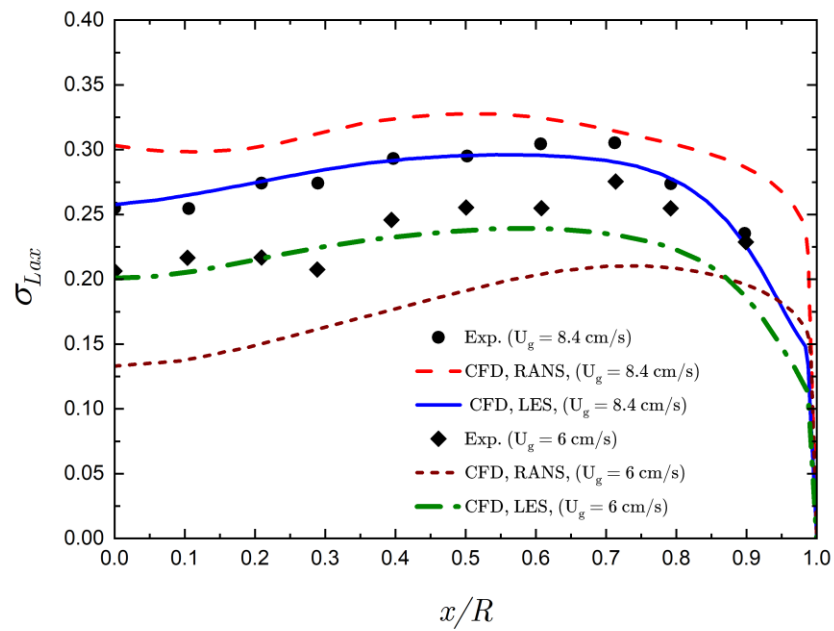
Fig. 5.6 Comparison of the calculated time averaged rms axial liquid velocity with experimental measurements at the height $h = 0.7$ m with mixture $k - \varepsilon$ and one-equation LES models.
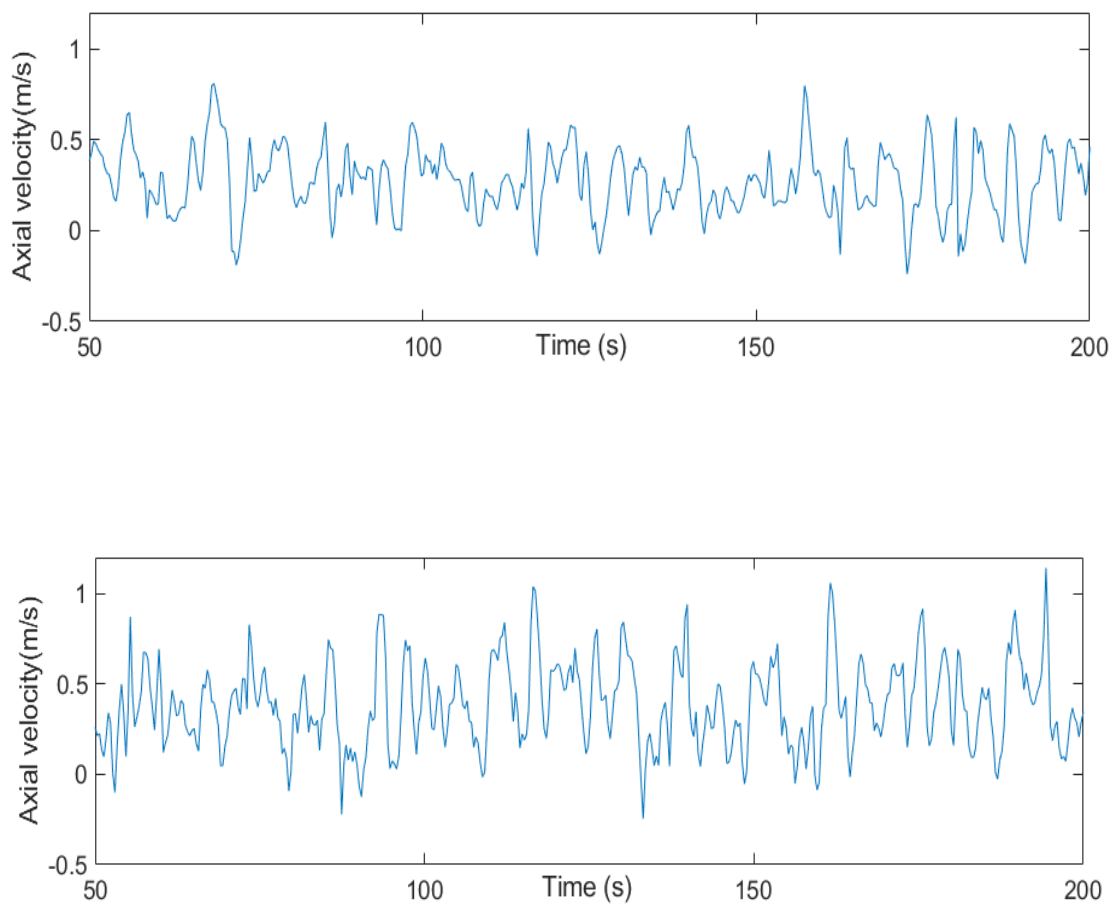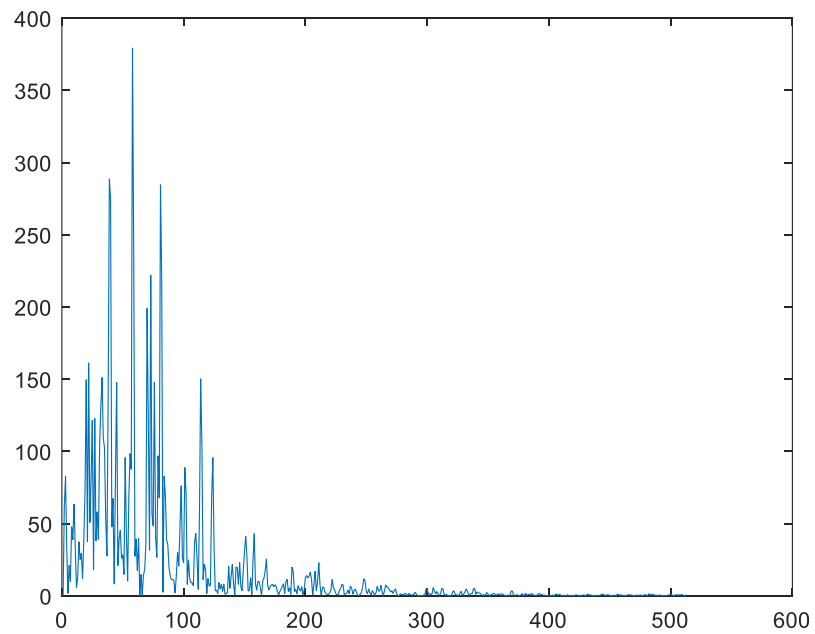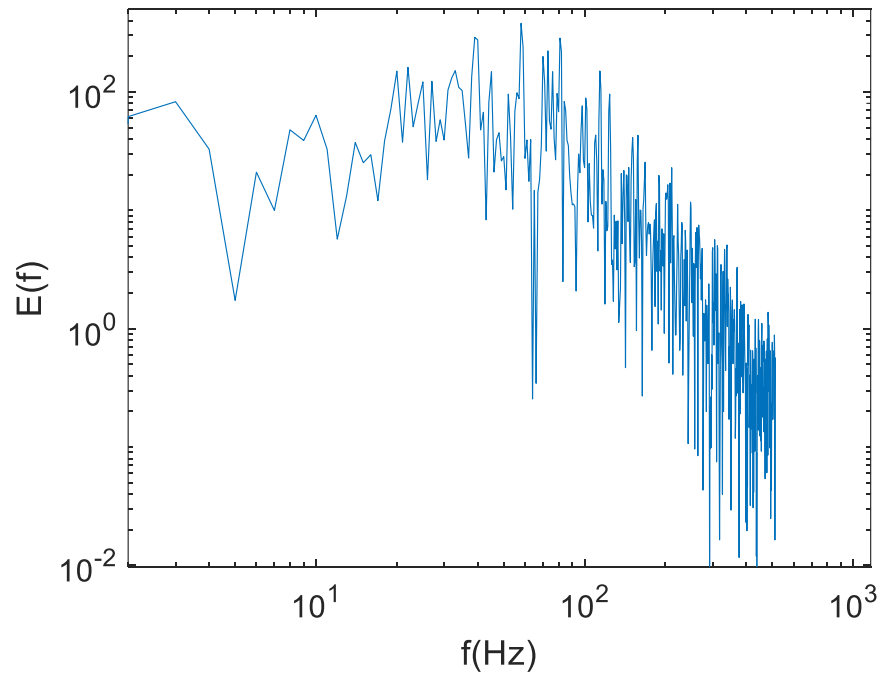
Fig. 5.7 Time history plots of the axial liquid velocity between $t =\ 50$ s and 200 s at $(0.0 \text{ m}, 0.0 \text{ m}, 0.7 \text{ m})$ of the column at inlet superficial gas velocity $U_G = 6$ cm/s (top) and $U_G = 8.4$ cm/s (bottom).

(a)

(b)
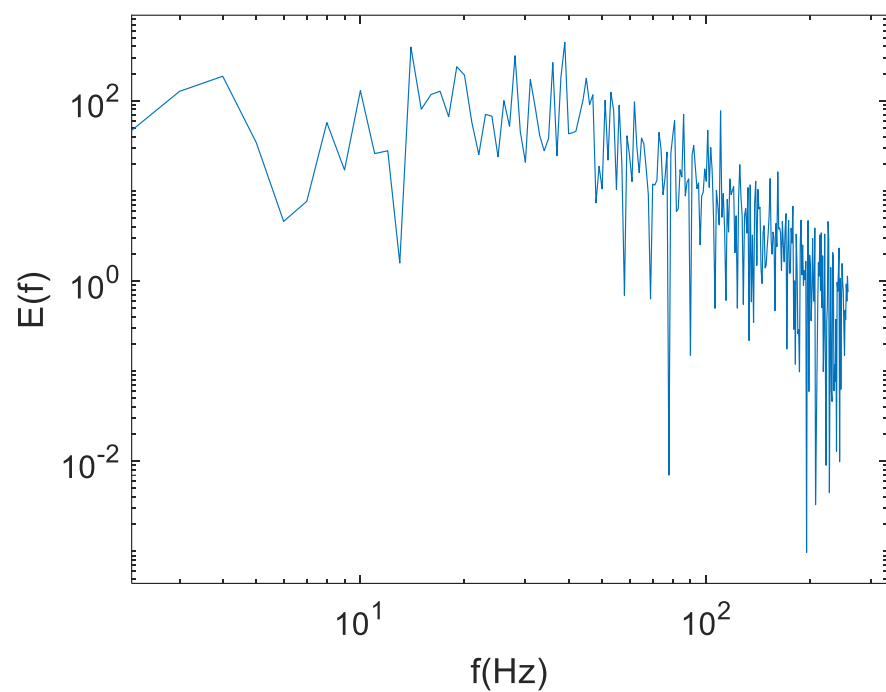
Fig. 5.8 Power spectra density of the axial liquid velocity at $(0.0 \text{ m}, 0.0 \text{ m}, 0.7 \text{ m})$ of the column at inlet superficial gas velocity $U_G = 6$ cm/s (a) and $U_G = 8.4$ cm/s (b).
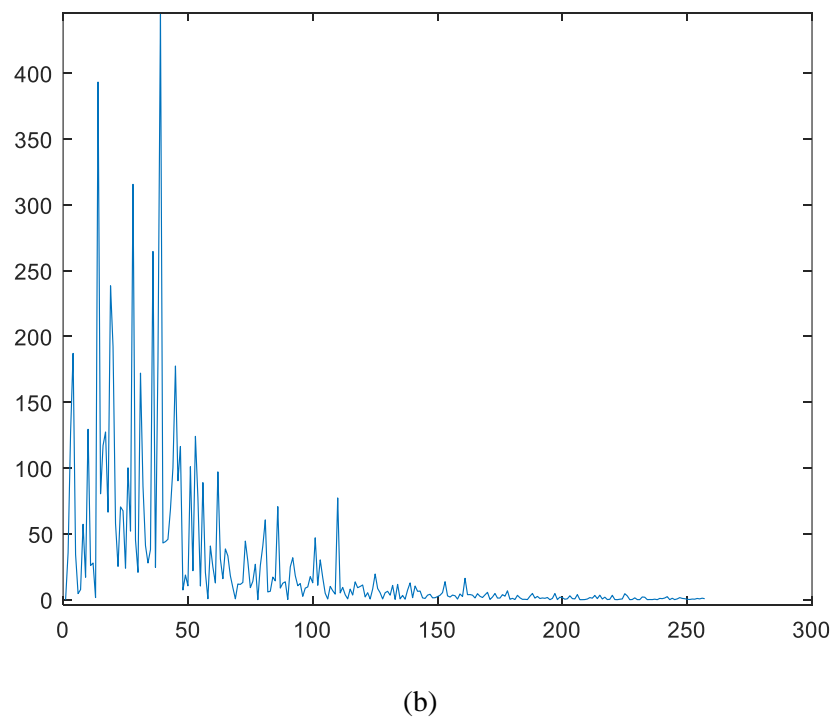
124

Fig.5.9 Predicted instantaneous and time-averaged vector field for liquid velocity and gas hold-up at inlet superficial gas velocity $U_G = 6$ cm/s (top) and $U_G = 8.4$ cm/s (bottom).
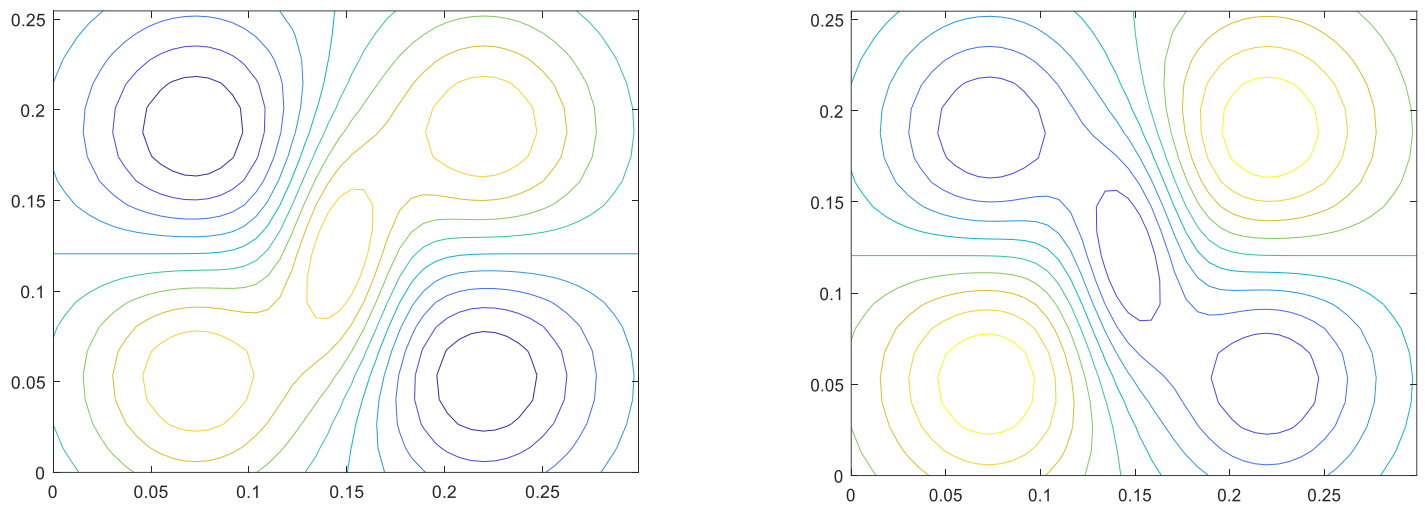
Fig. 5.10 Iso-contours of the initial templates depicting the cell circulations by the liquid velocity in the (x, z)-plane.
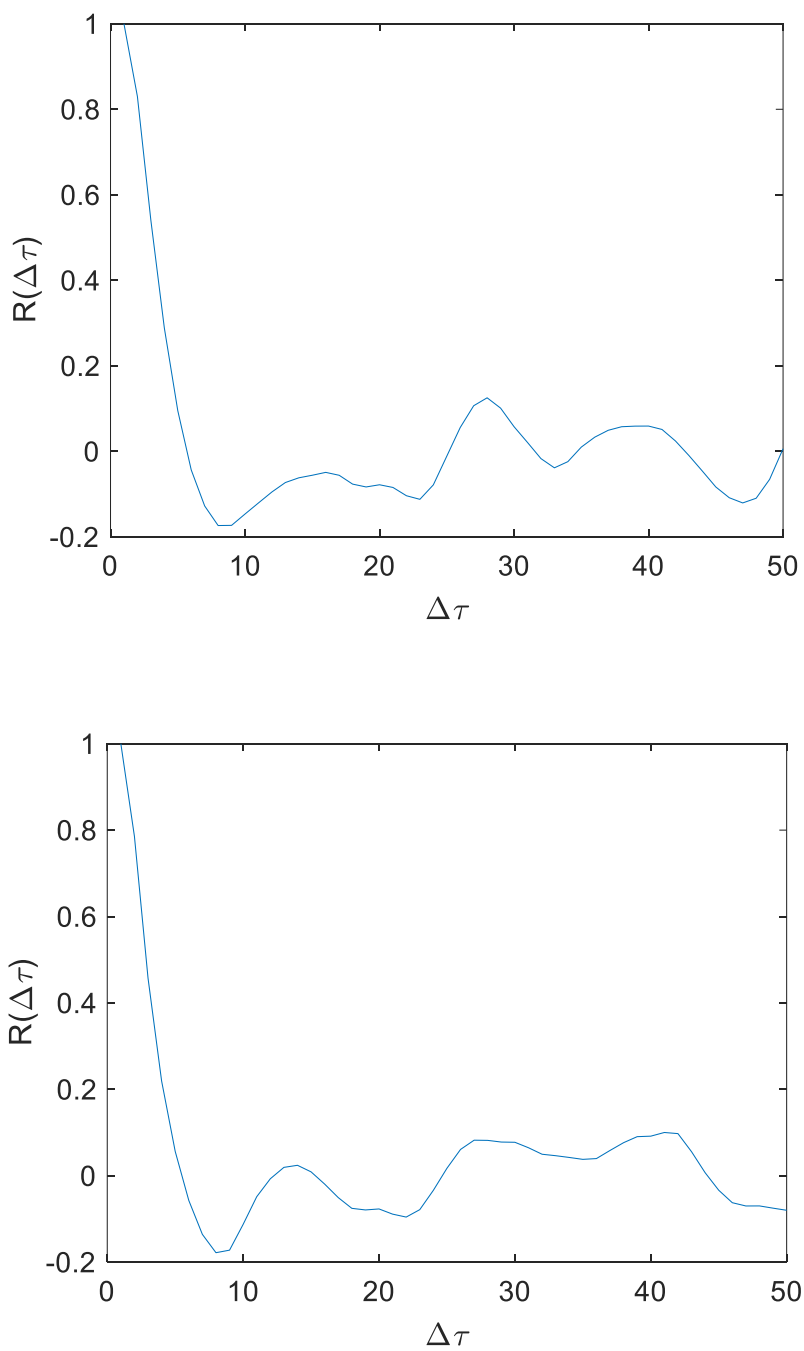
Fig. 5.11 Autocorrelation coefficient $R(\Delta\tau)$ for the axial liquid velocity at the height $h = 0.7$ m of the column at inlet superficial gas velocity $U_G = 6$ cm/s (top) and $U_G = 8.4$ cm/s (bottom).

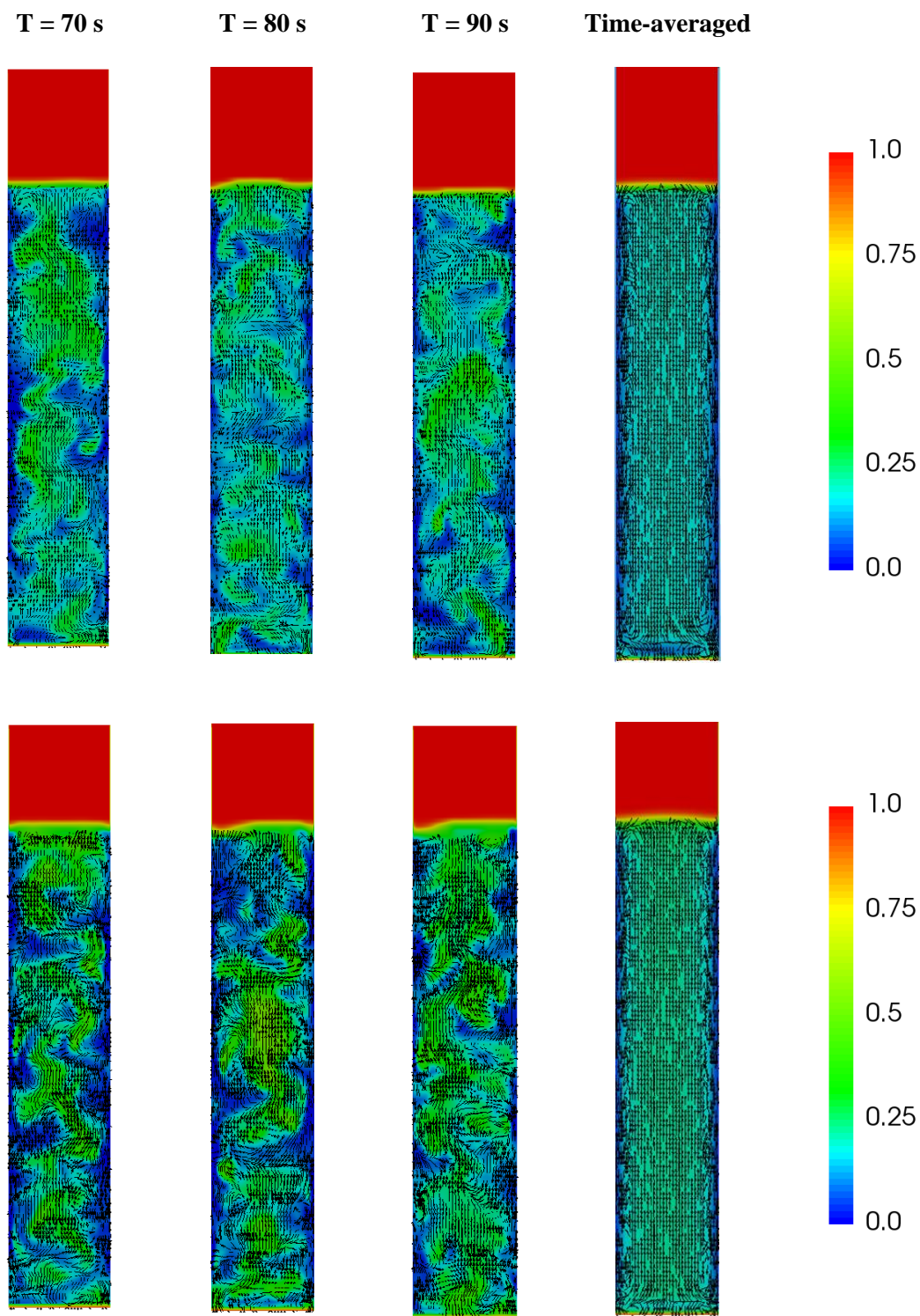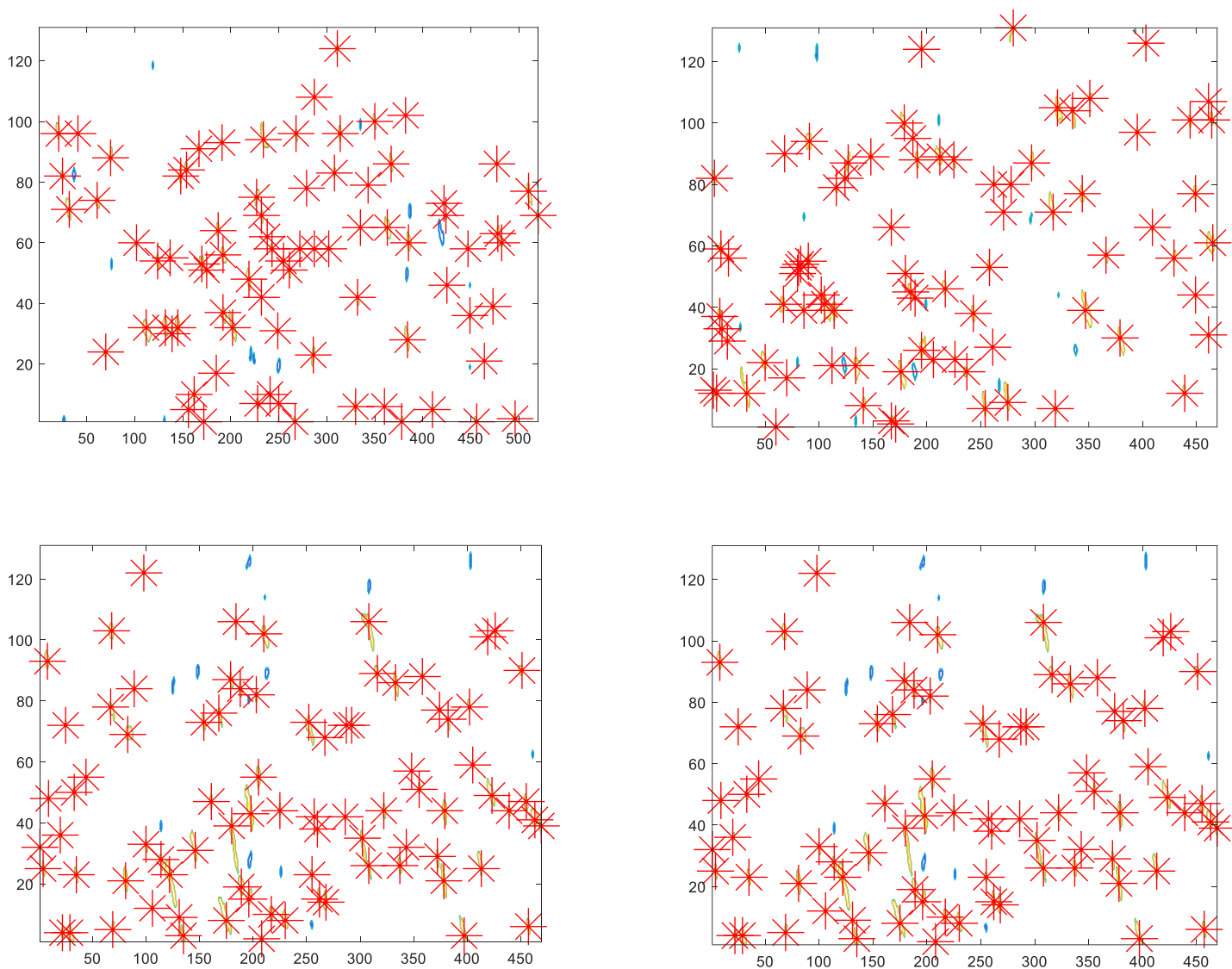**Fig. 5.12** Conditional sampled average flow structures map along the axial direction at each time at U_G cm/s=6cm/s (top) and $U_G = 8.4$ cm/s (bottom). The figures on the left-hand side correspond to template 1 and those on the right-hand side to template 2.

(e)

(f)

(g)

(h)
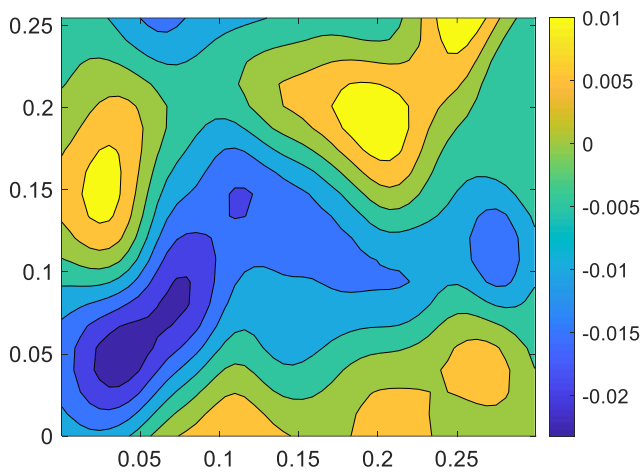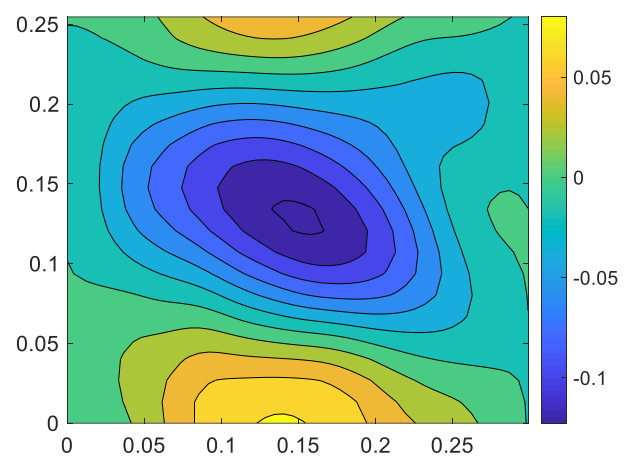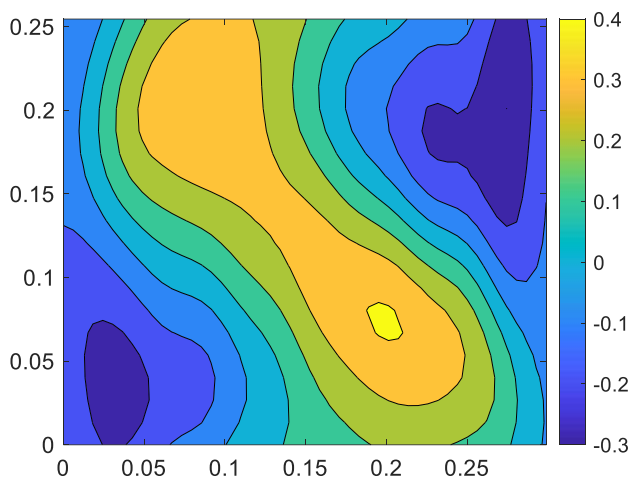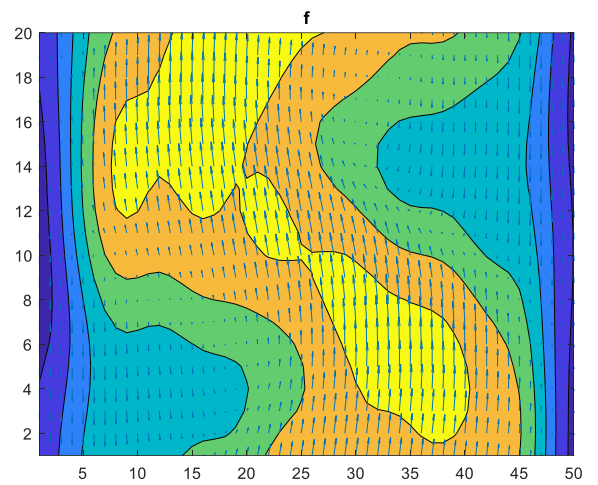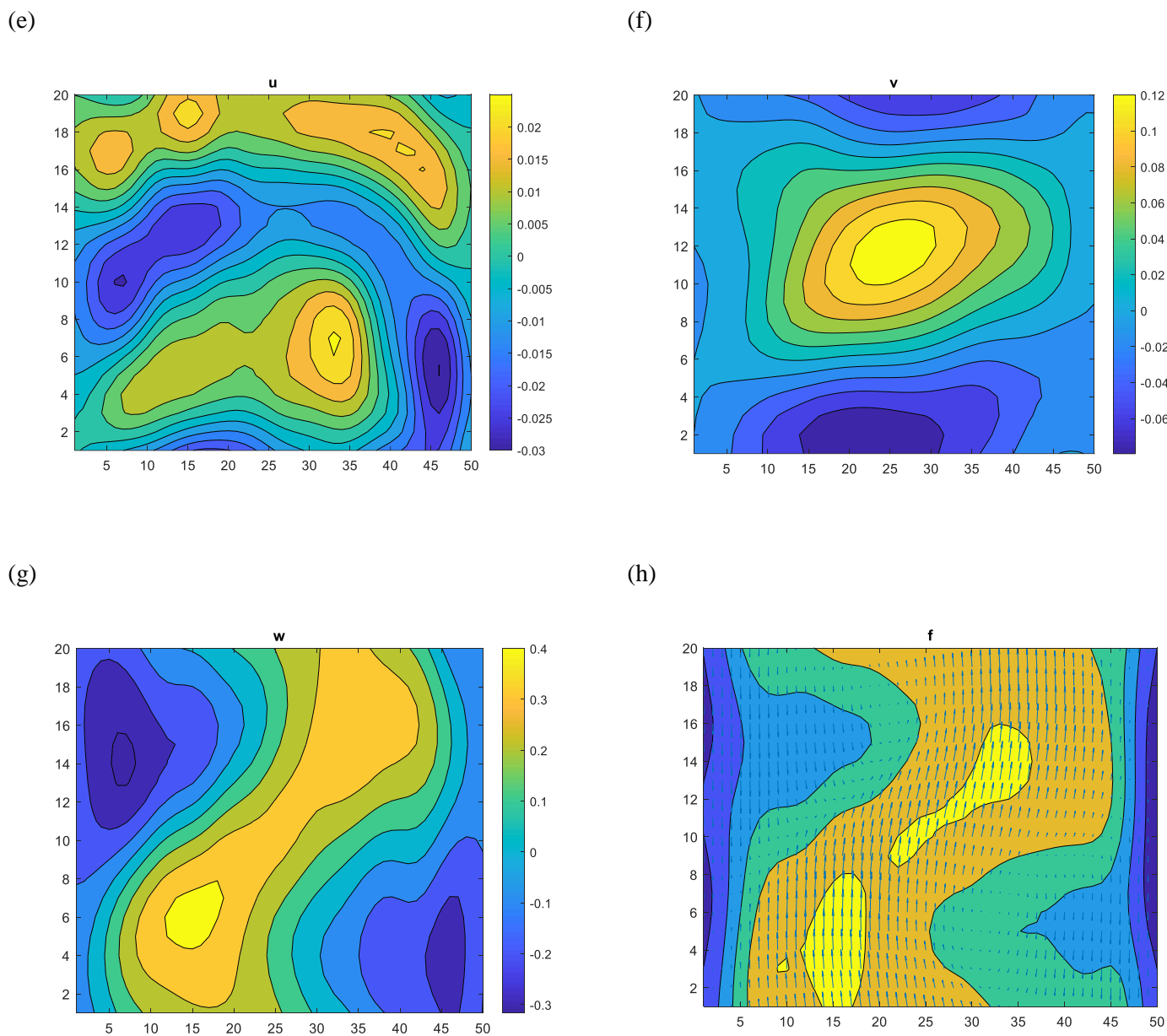
Fig. 5.13 Ensemble averaged of instantaneous liquid velocity and gas hold-up at $U_G = 6$ cm/s of (a, e) v −velocity, (b, f) u −velocity, (c, g) w −velocity, and (d, h) gas hold-up and vector field constructed with the axial and streamwise liquid velocity components. The figures (a)-(d) correspond to template 1 and (e)-(h) to template 2.

(a)

(b)

(c)

(d)
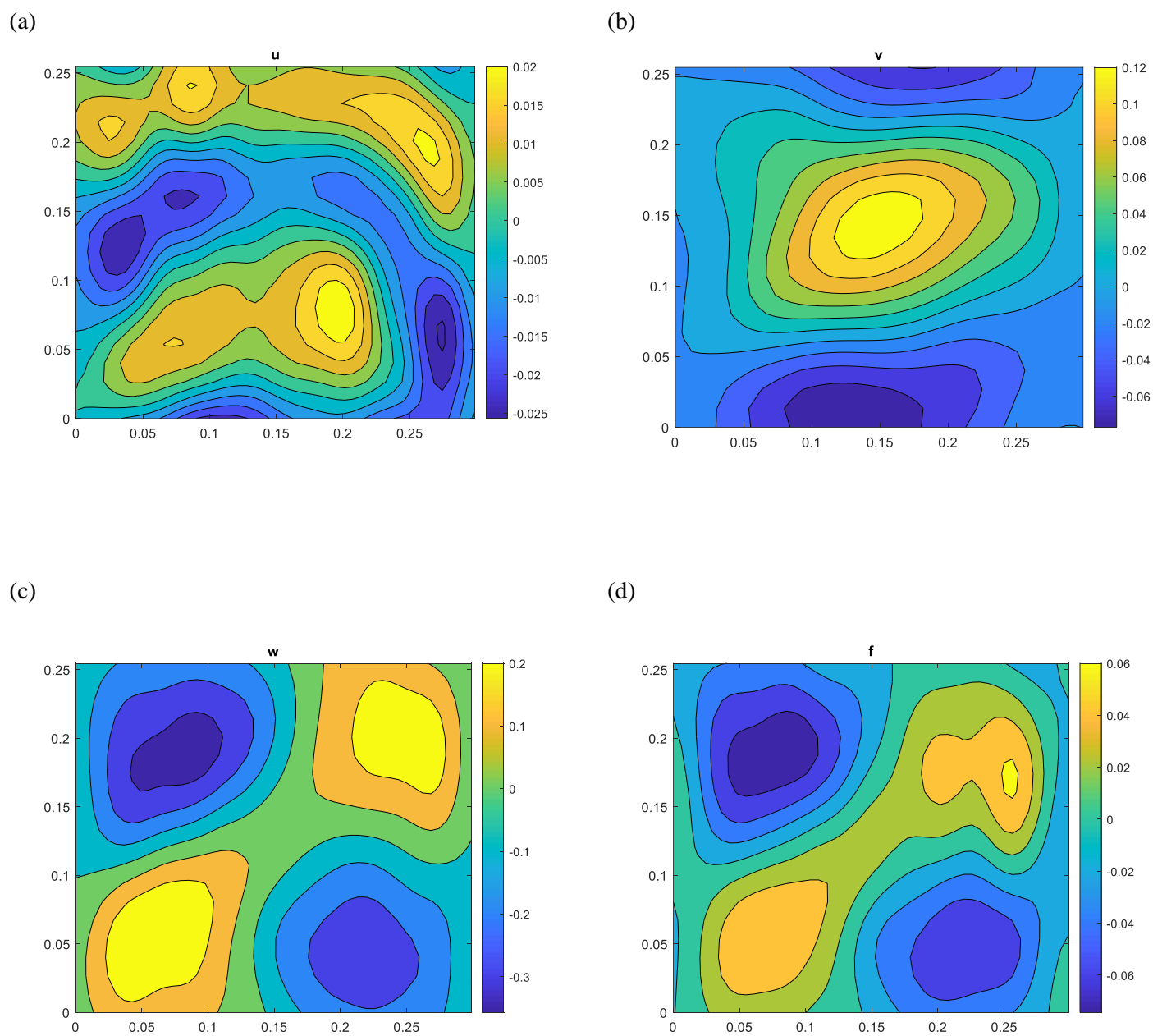
Fig. 5.14 Ensemble averaged of the fluctuation values at $U_G = 6$ cm/s of (a) v −velocity, (b) u −velocity, (c) w −velocity, and (d) gas hold-up.

(e)

(f)

(g)

(h)
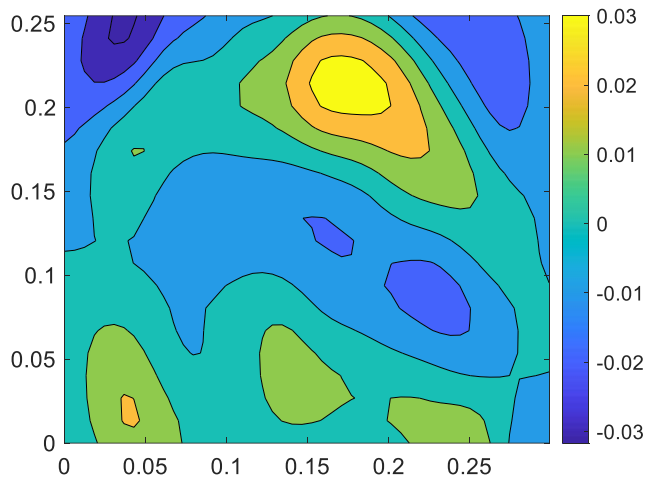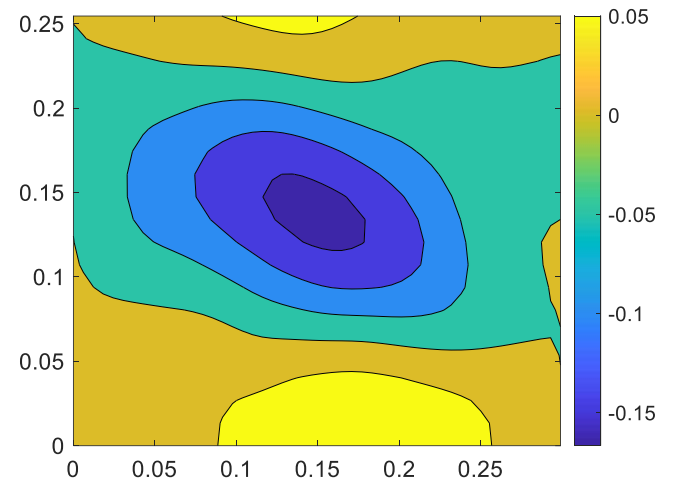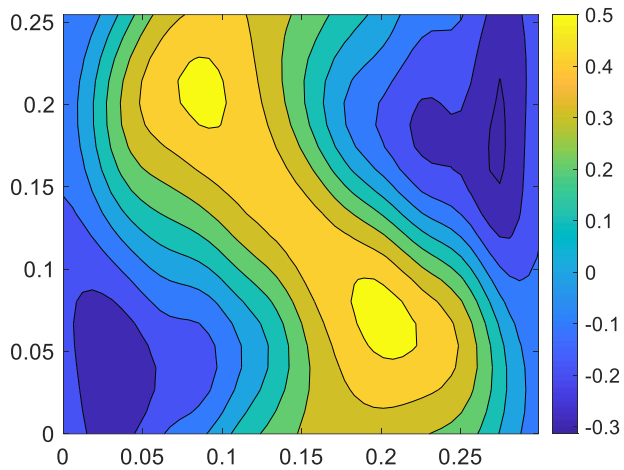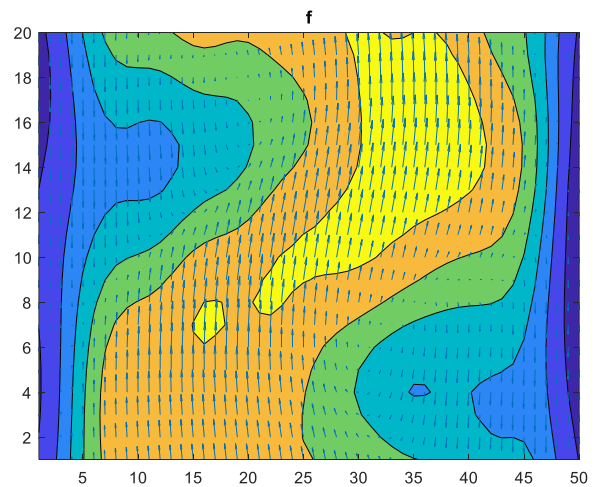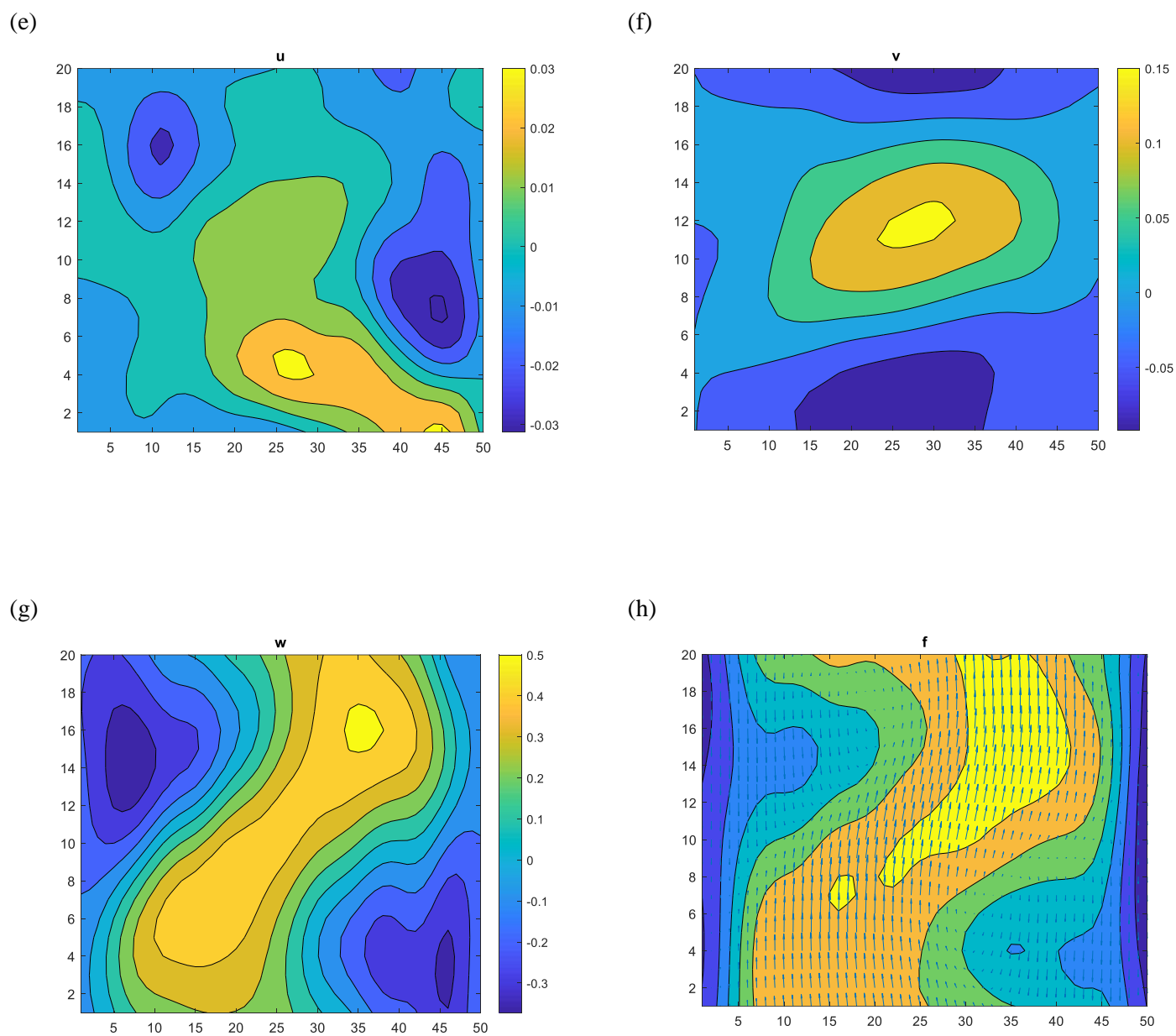
Fig. 5.15 Ensemble averaged of instantaneous liquid velocity and gas hold-up at $U_G = 8.4$ cm/s of (a, e) v −velocity, (b, f) u −velocity, (c, g) w −velocity, and (d, h) gas hold-up and vector field constructed with the axial and streamwise liquid velocity components. The figures (a)-(d) corresponded to template 1 and (e)-(h) to template 2.

133

(a)

(b)

(c)
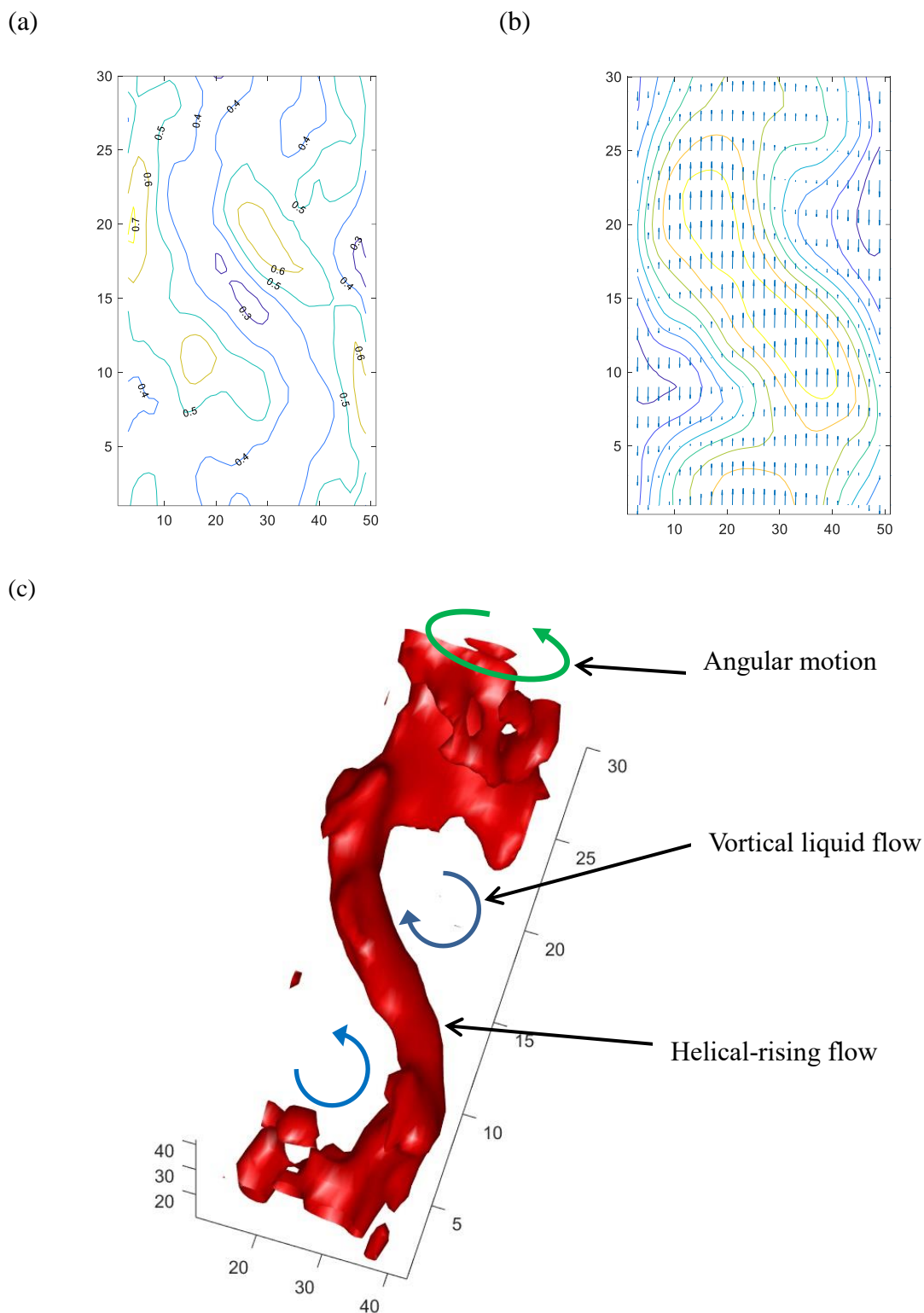
Fig. 5.16 (a) Sectional streamlines pattern, (b) ensemble average of ω_y with vector field constructed with the axial and streamwise liquid velocity components, (c) and three-dimensional view of vorticity iso-surface $|\omega| = 0.4 \, |\omega_{\max}|$ at $U_G = 6$ cm/s.

(a)

(b)

(c)
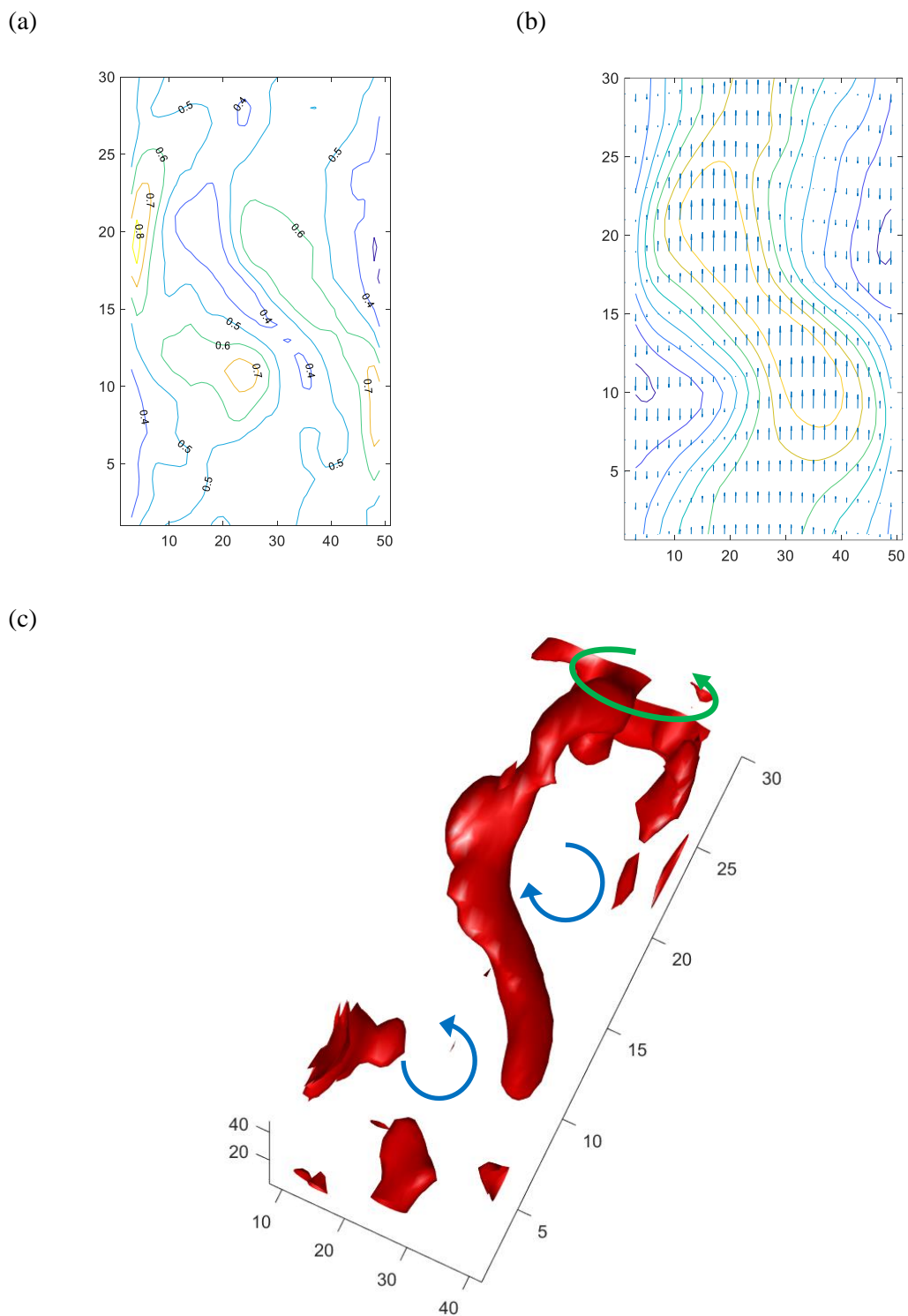
Fig. 5.17 (a) Sectional streamlines pattern, (b) ensemble average of ω_y with vector field constructed with the axial and streamwise liquid velocity components, and (c) three-dimensional view of vorticity iso-surface $|\omega| = 0.45 \, |\omega_{\mathrm{max}}|$ at $U_G = 8.4$ cm/s.

Chapter 6

Summary and conclusion

Hydrodynamic and gas-liquid mass transfer simulations have been carried out in a 3D cylindrical bubble column reactor of high aspect ratio (H/D) of 20 with a multiple orifice gas distributor for uniform aeration. We performed a multiscale analysis using the two-equation mixture $k - \varepsilon$ model, the LES model like Smagorinsky, and the one-equation SGS LES model to investigate turbulent multiphase flows and assess the above turbulence models. The predicted gas hold-up, liquid velocity, liquid velocity fluctuations, and the Reynolds stress tensors were displayed and compared with experimental measurements.

To assess the performance of the Euler-Euler mixture RANS model for simulations gas-liquid two phase flow in high ratio BCRs operated with uniform aeration and at superficial gas velocities in the range of 1.35 – 8.4 cm/s covering different flow regimes. Different combination of interfacial momentum forces, closure correlations, bubble diameters, and computational meshes were tested. The goal is in part to establish a generic two-phase model with appropriate closures to predict the hydrodynamic and regime transition for a broader range of flow conditions, compute mean scales of the flow and analyze the mass transfer. Therefore, to predict successfully 3D unsteady air-water flow in a high aspect ratio cylindrical bubble column, with twoPhaseEulerFoam solver implemented in the Open-FOAM CFD software, we found that

- a mixture $k - \varepsilon$ model with bubble induced turbulence, the Schiller-Neumann correlation for the drag force, and Lopez de Bortodano for the turbulence with $C_{TD} = 0.8$ dispersion force gives the best results for the whole range of gas flow rates considered.

- The lift force has insignificant influence.

- The results are in part very sensitive to the computational mesh. For instance, a finer grid resolution was possible only for high superficial gas velocities cases ($U_G > 2.6$ cm/s) and

are dependent on the bubble diameter in the center and mesh refinements in the near wall region.

- The CFD model was found to be more successful in calculating the local gas holdup, the axial velocity profile for the liquid and the *rms* of their fluctuations, and the global gas holdup in comparison to 2D calculations performed by other authors based on other models like the multifluid model or the population balance model, and have shown good agreements with the experiments. However, it over predicts the liquid recirculation in the near wall regions.

Locally, the calculated flow fields are characterized by different structures near the sparger corresponding to different transition flow regimes T_1 and T_2 with different pair vortices and several large flow structures along the column, which correspond to the experimental results reported by Olmos et al. 2003. The predicted overall mass transfer coefficient $K_L a_L$ agrees well with experimental measurements from the dynamic gassing-in and gassing-out method assuming both perfectly mixed liquid phase or axial dispersion for both homogeneous and heterogeneous regimes, though the slip penetration seems to do somewhat better than the eddy cell models with $K = 0.27$.

To simulate different flow scales and the transient and turbulent flow regimes the Eulerian-Eulerian LES, with zero- and one-equation SGS models, were used and large improvement with respect to the RANS approach was seen. The flow calculated by the Euler-Euler LES model is more dynamic and more details of the instantaneous local flow structure have been obtained including large-scale structures and vortices developed in the bubble plume edge. The one-equation model performs much better than the Smagorinsky model with $C_S = 0.08$ in the central plume and vortical flow regions. The Smagorinsky model improves the resolved axial liquid velocity profile in the near-wall region. Furthermore, the classical -5/3 law of power spectral density of the resolved liquid velocities is obtained for low frequency regions and -10/3 (-3) for high frequencies at $U_G = 6.0$ cm/s and $U_G = 8.4$ cm/s.

To identify different coherent structures developed and the transient large flow structures associated with rising bubbles in both the transient and churn-turbulent flow regimes we employed a conditional sampling technique with the sub-grid scale modeling based in the one-equation model and the bubble-induced turbulence. Different coherent structures were identified in the churn-turbulent flow regimes. The instantaneous results of LES reveal that the flow pattern is dominated by vortical structures. Multiple low-frequency cells of different sizes have been observed in the vortical-spiral flow region. The averaged large flow structures are educed using a conditional sampling technique and they consist of two counter-rotating vortices that move in a wavy-spiral motion through the column. The cross-correlation coefficient maps were obtained. For one template a nearly 79 events were detected in the spiral flow regime and 82 events in the turbulent regime with a correlation coefficient of 0.65. The two flow structures can occur simultaneously in more than 60 % but at different locations. The procedure yielded the topology of the three-dimensional large-scale structure which was visualized using iso-surfaces of the vorticity for different gas flow rates. The structures have spiral tube-shaped topology rotating along the column near the walls with a pair of counter-rotating cells sustained through the flow.

This study provides analysis of instantaneous flow information at different scales and pattern recognition of air-water flow which are crucial in further understanding hydrodynamics and flow transition of multiphase flow in bubble column reactors. Proper treatment for the wall region such as the use of low Reynolds number turbulence models combined with population balance models for accurate estimation of bubble size distribution are needed to better understand the turbulence and capture the liquid recirculation and the radial distribution of the gas hold-up in such reactors. Another key aspect for future research is to apply the sampling procedure together with Euler-Euler LES to identify transient flow structures in bubbly flows with contaminated fluids or in the presence of surfactants. An analysis of the kinetic energy budget is necessary to understand the effect of bubble induced turbulence and how energy is transferred toward and away the largest resolved scales.

BIBLIOGRAPHY

1. Asad, A., Kratzsch, C., and Schwarze, R., 2017. Influence of drag closures and inlet conditions on bubble dynamics and flow behavior inside a bubble column, *Eng. Appl. Comp. Fluid Mech.,* 11, 127–141

2. Bai, W., Deen, N.G. and Kuipers, J.A.M., 2011. Numerical analysis of the effect of gas sparging on bubble column hydrodynamics. *Industrial & Engineering Chemistry Research*, *50*(8), pp.4320-4328.

3. Bech, K., 2015. LES of a rectangular bubble column, *Conference on CFD in oil & gas,* metallurgical *& process industries. Fourth international Conference on CFD in the Oil and Gas, Metallurgical & Process Industries. SINTEF NTNU Trondheim, Norway*.

4. Behzadi, A., Issa, R.I. and Rusche, H., 2004. Modelling of dispersed bubble and droplet flow at high phase fractions. *Chemical Engineering Science*, *59*(4), pp.759-770.

5. Besagni, G., Inzoli, F., Ziegenhein, T. and Lucas, D., 2017. Computational Fluid-Dynamic modeling of the pseudo-homogeneous flow regime in large-scale bubble columns. *Chemical Engineering Science*, *160*, pp.144-160.

6. Besagni, G., Inzoli, F., and Ziegenhein, T., 2018. Two-phase bubble columns: a comprehensive review, *Chem. Eng*. 2, 13.

7. Bhusare, V.H., Dhiman, M.K., Kalaga, D.V., Roy, S., and Joshi, J.B., 2017. CFD simulations of a bubble column with and without internals by using OpenFOAM, *Chem. Eng. J*., 317, 157–174.

8. Bhole, M.R., Joshi, J.B. and Ramkrishna, D., 2008. CFD simulation of bubble columns incorporating population balance modeling. *Chemical Engineering Science*, *63*(8), pp.2267-2282.

9. Boisson, N., and Malin, M.R., 1996. Numerical prediction of two-phase flow in bubble columns, *Int. J. Numer. Methods Fluids*, 23, 1289–1310.

10. Buffo, A., Vanni, M., Renze, P. and Marchisio, D.L., 2016. Empirical drag closure for polydisperse gas–liquid systems in bubbly flow regime: Bubble swarm and micro-scale turbulence. *Chemical Engineering Research and Design*, *113*, pp.284-303.

11. Burns, A.D., Frank, T., Hamill, I. and Shi, J.M., 2004, May. The Favre averaged drag model for turbulent dispersion in Eulerian multi-phase flows. In *5th international conference on multiphase flow, ICMF* (Vol. 4, pp. 1-17). ICMF.

12. Buwa, V.V. and Ranade, V.V., 2002. Dynamics of gas–liquid flow in a rectangular bubble column: experiments and single/multi-group CFD simulations. *Chemical Engineering Science*, *57*(22-23), pp.4715-4736.

13. Buwa, V.V., Deo, D.S. and Ranade V.V., 2006. Eulerian–Lagrangian simulations of unsteady gas–liquid flows in bubble columns, *Int. J. Multiph. Flow*, 32, 864–885.

14. Buwa, V.V. and Ranade, V.V., 2004. Characterization of dynamics of gas–liquid flows in rectangular bubble columns, *AIChE J.*, 50, 2394–2407.

15. Bove, S., Solberg, T. and Hjertager, B.H., 2004. Numerical aspects of bubble column simulations. *International Journal of Chemical Reactor Engineering*, *2*(1).

16. Bauer, M. and Eigenberger, G., 1999. A concept for multi-scale modeling of bubble columns and loop reactors. *Chemical Engineering Science*, *54*(21), pp.5109-5117.

17. Cockx, A., Do-Quang, Z., Audic, J.M., Liné, A. and Roustan, M., 2001. Global and local mass transfer coefficients in waste water treatment process by computational fluid dynamics. *Chemical Engineering and Processing: Process Intensification*, *40*(2), pp.187-194.

18. Camarasa, E., Vial, C., Poncin, S., Wild, G., Midoux, N. and Bouillard, J., 1999. Influence of coalescence behaviour of the liquid and of gas sparging on hydrodynamics and bubble characteristics in a bubble column. *Chemical Engineering and Processing: Process Intensification*, *38*(4-6), pp.329-344.

19. Chen, R.C., Reese, J. and Fan, L.S., 1994. Flow structure in a three-dimensional bubble column and three-phase fluidized bed. *AIChE Journal*, *40*(7), pp.1093-1104.

20. Chen, Q., Zhong, Q., Qi, M. and Wang, X., 2015. Comparison of vortex identification criteria for planar velocity fields in wall turbulence. *Physics of Fluids*, *27*(8), p.085101.

21. Clift, R., Grace, J.R. and Weber, M.E., 1978. Bubbles, drops, and particles. *Academic Press, New York*.

22. Deen, N.G., Solberg, T. and Hjertager, B.H., 2001. Large eddy simulation of the gas–liquid flow in a square cross-sectioned bubble column. *Chemical engineering science*, *56*(21-22), pp.6341-6349.

23. Darmana, D., Deen, N.G., Kuipers, J.A.M., Harteveld, W.K. and Mudde, R.F., 2009. Numerical study of homogeneous bubbly flow: influence of the inlet conditions to the hydrodynamic behavior. *International journal of multiphase flow*, *35*(12), pp.1077-1099.

24. Davidson, L., 1997. *Large eddy simulations: A note on derivation of the equations for the subgrid turbulent kinetic energies*. Technical Report 97/11, Dept. of Thermo and Fluid Dynamics, Chalmers University of Technology, Gothenburg.

25. Dhotre, M.T., Niceno, B. and Smith, B.L., 2008. Large eddy simulation of a bubble column using dynamic sub-grid scale model. *Chemical Engineering Journal*, *136*(2-3), pp.337-348.

26. Dhotre, M.T., Niceno, B., Smith, B.L. and Simiano, M., 2009. Large-eddy simulation (LES) of the large scale bubble plume. *Chemical Engineering Science*, *64*(11), pp.2692-2704.

27. Dhotre, M.T., Deen, N.G., Niceno, B., Khan, Z. and Joshi, J.B., 2013. Large eddy simulation for dispersed bubbly flows: a review. *International Journal of Chemical Engineering*, *2013*.

28. De Bertodano, M.L., Lahey Jr, R.T. and Jones, O.C., 1994. Phase distribution in bubbly two-phase flow in vertical ducts. *International Journal of Multiphase Flow*, *20*(5), pp.805-818.

29. Drew, D.A., Lahey, R.T., 1979. Application of general constitutive principles to the derivation of multidimensional two-phase equations, *Int. J. Multiph. Flows* 4, 243–246.

30. Drew, D.A., Passman, S.L., 1998. Theory of multicomponent fluids, *Springer-Verlag, New York* 135.

31. Ekambara, K. and Dhotre, M.T., 2010. CFD simulation of bubble column. *Nuclear engineering and design*, *240*(5), pp.963-969.

32. Eppinger, T., Matheus, H. and Aglave, R., 2015. 3D simulation and validation of a lab scale bubble column, *Chem. Eng. Trans.*, 43, 1639–1644.

33. Franz, K., 1984. Flow structure in bubble columns. *Ger. Chem. Eng.*, *7*, pp.365-374.

34. Fard, M.G., Vernet, A., Stiriba, Y. and Grau, X., 2020. Transient large-scale two-phase flow structures in a 3D bubble column reactor. *International Journal of Multiphase Flow*, p.103236.

35. Gourich, B., Vial, C., Essadki, A.H., Allam, F., Soulami, M.B. and Ziyad, M., 2006. Identification of flow regimes and transition points in a bubble column through analysis of differential pressure signal—influence of the coalescence behavior of the liquid phase. *Chemical Engineering and Processing: Process Intensification*, *45*(3), pp.214-223.

36. Gourich, B., Vial, C., El Azher, N., Soulami, M.B. and Ziyad, M., 2008. Influence of hydrodynamics and probe response on oxygen mass transfer measurements in a high aspect ratio bubble column reactor: Effect of the coalescence behaviour of the liquid phase. *Biochemical engineering journal*, *39*(1), pp.1-14.

37. Gourich, B., Vial, C., El Azher, N., Soulami, M.B. and Ziyad, M., 2006. Improvement of oxygen mass transfer estimation from oxygen concentration measurements in bubble column reactors. *Chemical Engineering Science*, *61*(18), pp.6218-6222.

38. Groen, J.S., 2004. Scales and structures in bubbly flows – Experimental analysis of the flow in bubble columns and in bubbling fluidized beds, *PhD Thesis*, Delft University of Technology.

39. Huang, Z., McClure, D.D., Barton, G.W., Fletcher, D.F. and Kavanagh, J.M., 2018. Assessment of the impact of bubble size modelling in CFD simulations of alternative bubble column configurations operating in the heterogeneous regime. *Chemical Engineering Science*, *186*, pp.88-101.

40. Hu, G. and Celik, I., 2008. Eulerian–Lagrangian based large-eddy simulation of a partially aerated flat bubble column. Chemical Engineering Science, 63(1), pp.253-271.

41. Harteveld, W.K., Mudde, R.F. and Van Den Akker, H.E., 2003. Dynamics of a bubble column: influence of gas distribution on coherent structures. *The Canadian Journal of Chemical Engineering*, *81*(3-4), pp.389-394.

42. Ishii, M. and Hibiki, T., 2010. *Thermo-fluid dynamics of two-phase flow*. Springer Science & Business Media.

43. Jakobsen, H.A., 2001. Phase distribution phenomena in two-phase bubble column reactors. *chemical Engineering science*, *56*(3), pp.1049-1056.

44. Jakobsen, H.A., Lindborg, H. and Dorao, C.A., 2005. Modeling of bubble column reactors: progress and limitations. *Industrial & engineering chemistry research*, *44*(14), pp.5107-5151.

45. Jamialahmadi, M. and Müller-Steinhagen, H., 1989. Bubble formation and coalescence in bubble columns. *Chemie Ingenieur Technik*, *61*(9), pp.715-718.

46. Jeong, J. and Hussain, F., 1995. On the identification of a vortex. *Journal of fluid mechanics*, *285*, pp.69-94.

47. Joshi, J.B., Sharma, M.M., 1979. A circulation cell model for bubble columns. Trans. of the Inst. of Chem. Eng. Sci., 57, 244-251.

48. Joshi, J.B., 1980. Axial mixing in multiphase contactors – a unified correlation. Trans. of the Inst. of Chem. Eng. Sci., 58, 155-165.

49. Joshi, J.B., 2001. Computational flow modelling and design of bubble column reactors. *Chemical engineering science*, *56*(21-22), pp.5893-5933.

50. Joshi, J.B., Vitankar, V.S., Kulkarni, A.A., Dhotre, M.T. and Ekambara, K., 2002. Coherent flow structures in bubble column reactors. Chemical Engineering Science, 57(16), pp.3157-3183.

51. Kawase, Y., Halard, B. and Moo-Young, M., 1987. Theoretical prediction of volumetric mass transfer coefficients in bubble columns for Newtonian and non-Newtonian fluids. *chemical Engineering science*, *42*(7), pp.1609-1617.

52. Kantarci, N., Borak, F., and Ulgen, K.O., 2005. Bubble column reactors, *Proc. Biochem.*, 40, 2263-2283.

53. Khan, Z., Mathpati, C. S., Joshi, J. B., 2017. Comparison of turbulence models and dynamics of turbulence structures in bubble column reactors: effects of sparger design and superficial gas velocities, Chem. Eng. Sci. 164, 34-52.

54. Kouzbour, S., Stiriba, Y., Gourich, B. and Vial, C., 2020. CFD simulation and analysis of reactive flow for dissolved manganese removal from drinking water by aeration process using an airlift reactor. *Journal of Water Process Engineering*, *36*, p.101352.

55. Krishna, R. and Van Baten, J.M., 2001. Eulerian simulations of bubble columns operating at elevated pressures in the churn turbulent flow regime. *Chemical Engineering Science*, *56*(21-22), pp.6249-6258.

56. Kulkarni, A.A., 2007. Mass transfer in bubble column reactors: effect of bubble size distribution. *Industrial & engineering chemistry research*, *46*(7), pp.2205-2211.

57. Laborde-Boutet, C., Larachi, F., Dromard, N., Delsart, O. and Schweich, D., 2009. CFD simulation of bubble column flows: Investigations on turbulence models in RANS approach. *Chemical Engineering Science*, *64*(21), pp.4399-4413.

58. Lamont, J.C. and Scott, D.S., 1970. An eddy cell model of mass transfer into the surface of a turbulent liquid. *AIChE Journal*, *16*(4), pp.513-519.

59. Law, D., Battaglia, F. and Heindel, T.J., 2008. Model validation for low and high superficial gas velocity bubble column flows. *Chemical Engineering Science*, *63*(18), pp.4605-4616.

60. Lehr, F., Millies, M. and Mewes, D., 2002. Bubble-size distributions and flow fields in bubble columns. *AIChE Journal*, *48*(11), pp.2426-2443.

61. Le Moullec, Y., Potier, O., Gentric, C. and Leclerc, J.P., 2008. Flow field and residence time distribution simulation of a cross-flow gas–liquid wastewater treatment reactor using CFD. *Chemical Engineering Science*, *63*(9), pp.2436-2449.

62. Lin, T.J., Reese, J., Hong, T. and Fan, L.S., 1996. Quantitative analysis and computation of two-dimensional bubble columns. *AIChE Journal*, *42*(2), pp.301-318.

63. Liu, Z. and Li, B., 2018. Scale-adaptive analysis of Euler-Euler large eddy simulation for laboratory scale dispersed bubbly flows. *Chemical Engineering Journal*, *338*, pp.465-477.

64. Lu, J. and Tryggvason, G., 2013. Dynamics of nearly spherical bubbles in a turbulent channel upflow. *Journal of Fluid Mechanics*, *732*, p.166.

65. Lance, M. and Bataille, J., 1991. Turbulence in the liquid phase of a uniform bubbly air–water flow. Journal of fluid mechanics, 222, pp.95-118.

66. Lapin, A. and Lübbert, A., 1994. Numerical simulation of the dynamics of two-phase gas—liquid flows in bubble columns. Chemical Engineering Science, 49(21), pp.3661-3674.

67. Lakehal, D., Smith, B., Milelli, M., 2018. Large-Eddy Simulation of bubbly turbulent shear flows, J. Turbul. 25, 1-21.

68. Lakehal, D., 2018. Status and future developments of Large-Eddy Simulation of turbulent multi-fluid flows (LEIS and LESS), *Int. J. Multiph. Flow* 104, 322-337.

69. Ma, T., Lucas, D., Ziegenhein, T., Fröhlich, J, and Deen, NG, 2015a. Scale-adaptive simulation of a square cross-sectional bubble column, Chem. Eng. Sci. 131, 101–108.

70. Ma, T., Ziegenhein, T., Lucas, D., Krepper, E., Fröhlich, J., 2015b. Euler-Euler large eddy simulations for dispersed turbulent bubbly flows, *Int. J. Heat Fluid Flow* 56, 51–59.

71. Ma, T., Ziegenhein, T., Lucas, D. and Fröhlich, J., 2016. Large eddy simulations of the gas–liquid flow in a rectangular bubble column. *Nuclear Engineering and Design*, *299*, pp.146-153.

72. Martinez Mercado, J., Chehata Gomez, D., van Gils, D., Sun, C. and Lohse, D., 2009. On bubble clustering and energy spectra in pseudo-turbulence. APS, 62, pp.AK-005.

73. Masood, R.M.A. and Delgado, A., 2014. Numerical investigation of the interphase forces and turbulence closure in 3D square bubble columns. *Chemical Engineering Science*, *108*, pp.154-168.

74. Masterov, M.V., Baltussen, M.W., Kuipers, J.A.M., 2018. Numerical simulation of a square bubble column using Detached Eddy Simulation and Euler-Lagrange approach, Int. J. Multiph. Flow 107, 275–288.

75. Montoya, G., Lucas, D., Baglietto, E., Liao, Y., 2016. A review on mechanisms and models for the churn-turbulent flow regime, Chem. Eng. Sci. 141, 86–103.

76. Myong, H.K., Kasagi, N., 1990. A new approach to the improvement of turbulence model for wall-bounded shear flows, JSME Int. J., 33, 63-72.

77. Mudde, R.F. and Simonin, O., 1999. Two-and three-dimensional simulations of a bubble plume using a two-fluid model. *Chemical Engineering Science*, *54*(21), pp.5061-5069.

78. Mudde, R.F., Groen, J.S., Van Den Akker, H.E.A., 1997. Liquid velocity field in a bubble column: LDA experiments. Chem. Eng. Sci. 52, 4217-4224.

79. Mudde, R.F., Groen, J.S., Van Den Akker, H.E.A., 2002. Coherent structures and axial dispersion in bubble column reactors. Chem. Eng. Sci. 51, 2511-2520.

80. Mudde, R.F., 2005. Bubbly gravity-driven flows. Annu. Review. Fluid. Mech. 37, 393-423.

81. Milelli, M., 2002. A numerical analysis of confined turbulent bubble plume. Diss. EH. No. 14799, Swiss Federal Institute of Technology, Zurich, 2007.

82. Ničeno, B., Dhotre, M.T. and Deen, N.G., 2008. One-equation sub-grid scale (SGS) modelling for Euler–Euler large eddy simulation (EELES) of dispersed bubbly flow. Chemical Engineering Science, 63(15), pp.3923-3931.

83. Olmos, E., Gentric, C., Vial, C., Wild, G. and Midoux, N., 2001. Numerical simulation of multiphase flow in bubble column reactors. Influence of bubble coalescence and break-up. *Chemical engineering science*, *56*(21-22), pp.6359-6365.

84. Olmos, E., Gentric, C. and Midoux, N., 2003. Identification of Flow Regimes in a Flat Gas-liquid Bubble Column via Wavelet Transform. *The Canadian Journal of Chemical Engineering*, *81*(3-4), pp.382-388.

85. Olmos, E., Gentric, C. and Midoux, N., 2003. Numerical description of flow regime transitions in bubble column reactors by a multiple gas phase model. Chemical Engineering Science, 58(10), pp.2113-2121.

86. Olmos, E., Gentric, C., Vial, Ch., Wild, Midoux, N., 2003. Description of flow transitions in bubble column via laser Doppler anemometry signals processing. Chem. Eng. Sc. 58, 1731-1742.

87. OpenFOAM Ltd., United Kingdom, 2012, OpenFOAM v.4.0.0 user's guide.

88. Pan, Y., Dudukovic, M.P. and Chang, M., 1999. Dynamic simulation of bubbly flow in bubble columns. *Chemical Engineering Science*, *54*(13-14), pp.2481-2489.

89. Paul, M., Strassl, F., Hoffmann, A., Hofmann, M., Schlüter, and Herres-Pawlis, S., 2018. Reaction systems for bubbly flows, *Eur. J. Inorg. Chem.,* 2101-2124.

90. Pfleger, D., Gomes, S., Gilbert, N.., and Wagner, H.G., 1999. Hydrodynamic simulations of laboratory scale bubble columns fundamental studies of the Eulerian–Eulerian modelling approach, *Chem. Eng. Sci.,* 54, 5091–5099.

91. Pfleger, D. and Becker, S., 2001. Modelling and simulation of the dynamic flow behaviour in a bubble column. *Chemical engineering science*, *56*(4), pp.1737-1747.

92. Pallares, J., Vernet, A., Ferre, J.A., Grau, F.X., 2010. Turbulent large-scale structures in natural convection vertical channel. Int. J. Heat Mass Transf. 53, 4168-4175.

93. Pope, S., Turbulent flows, 2011. Cambridge University Press.

94. Prakash, V.N., Mercado, J.M., van Wijngaarden, L., Mancilla, E., Tagawa, Y., Lohse, D. and Sun, C., 2016. Energy spectra in turbulent bubbly flows. Journal of fluid mechanics, 791, pp.174-190.

95. Parekh, J, and Rzehak, R., 2017. Euler–Euler multiphase CFD-simulation with full Reynolds stress model and anisotropic bubble-induced turbulence, *Int. J. Multiph Flow*, 99, 231–245.

96. Pourtousi, M., Sahu, J.N., Ganesan, P., 2014. Effect of interfacial forces and turbulence models on predicting flow pattern inside the bubble column, *Chem. Eng. Process. Process Intensif.* 75, 38–47.

97. Rusche, H., and Issa, R.I., 2000. The effect of voidage on the drag force on particles, droplets and bubbles in dispersed two-phase flow, *the Japanese Society for Multiphase Flow, Tshkuba, Japan*.

98. Rusche, H., 2002. *Computational fluid dynamics of dispersed two-phase flows at high phase fractions* (Doctoral dissertation, University of London).

99. Rampure, M.R., Mahajani, S.M., and Ranade, V.V., 2019. CFD simulation of bubble columns: modeling of nonuniform gas distribution at sparger, *Ind. Eng. Chem. Res*., 48, 8186–8192.

100. *Rampure*, M.R., Buwa, V.V. and Ranade, V.V., 2003. Modelling of gas-liquid/ gas-liquid-solid flows in bubble columns: experiments and CFD simulations, *Can. J. Chem. Eng.,* 81, 692–706.

101. Ranade, V.V., 1997. Modelling of turbulent flow in a bubble column reactor, Chem. Eng. Res. Des., 75, 14–23.

102. Ranade, V.V., 1992. Flow in bubble columns: some numerical experiments, Chem. Eng. Sci., 47, 1857–1869.

103. Rollbusch, Ph., Bothe, M., Becker, M., Ludwig, M., Grünewald, M., Schülter, M., Franke, R., 2015. Bubble columns operated under industrially relevant conditions – Current understanding of design parameters, *Chem. Eng. Sci.*, 126, 660-678.

104. Riboux, G., Risso, F. and Legendre, D., 2010. Experimental characterization of the agitation generated by bubbles rising at high Reynolds number. Journal of Fluid Mechanics, 643, p.509.

105. Schlüter, S., Steiff, A., and Weinspach, P.-M., 1995. Heat transfer in two- and three-phase bubble column reactors with internals, *Chem. Eng. and Proc.*, 34, 157-172.

106. Selma, B., Bannari, R. and Proulx, P., 2010. A full integration of a dispersion and interface closures in the standard k–ε model of turbulence. *Chemical engineering science*, *65*(20), pp.5417-5428.

107. Simonnet, M., Gentric, C., Olmos, E. and Midoux, N., 2008. CFD simulation of the flow field in a bubble column reactor: Importance of the drag force formulation to describe regime transitions. *Chemical Engineering and Processing: Process Intensification*, *47*(9-10), pp.1726-1737.

108. Sato, Y. and Sekoguchi, K., 1975. Liquid velocity distribution in two-phase bubble flow. *International Journal of Multiphase Flow*, *2*(1), pp.79-95.

109. Snip, A.I., Kolhatkar, R.V., Swamy, D., Joshi, J.B., 1992. Criteria for the transition from the homogeneous to the heterogeneous regime in two-dimensional bubble column reactors, *Chem. Eng. Sci.,* 18, 505–726.

110. Sokolichin, A. and Eigenberger, G., 1999. Applicability of the standard k–ε turbulence model to the dynamic simulation of bubble columns: Part I. Detailed numerical simulations. *Chemical Engineering Science*, *54*(13-14), pp.2273-2284.

111. Sokolichin, A., Eigenberger, G. and Lapin, A., 2004. Simulation of buoyancy driven bubbly flow: established simplifications and open questions. *AIChE Journal*, *50*(1), pp.24-45.

112. Stiriba, Y., Gourich, B. and Vial, C., 2017. Numerical modeling of ferrous iron oxidation in a split-rectangular airlift reactor. *Chemical Engineering Science*, *170*, pp.705-719.

113. Sathe, M.J., Mathpati, C.S., Deshpande, S.S., Khan, Z., Ekambara, K. and Joshi, J.B., 2011. Investigation of flow structures and transport phenomena in bubble columns using particle image velocimetry and miniature pressure sensors. Chemical engineering science, 66(14), pp.3087-3107.

114. Simiano, M. and Lakehal, D., 2012. Turbulent exchange mechanisms in bubble plumes. International journal of multiphase flow, 47, pp.141-149.

115. Sun, J., Wang, J. and Yang, Y., 2012. CFD simulation and wavelet transform analysis of vortex and coherent structure in a gas–solid fluidized bed. Chemical engineering science, 71, pp.507-519.

116. Tabib, M.V., Roy, S.A. and Joshi, J.B., 2008. CFD simulation of bubble column—an analysis of interphase forces and turbulence models. *Chemical Engineering Journal*, *139*(3), pp.589-614.

117. Tabib, M.V. and Schwarz, P., 2011. Quantifying sub-grid scale (SGS) turbulent dispersion force and its effect using one-equation SGS large eddy simulation (LES) model in a gas–liquid and a liquid–liquid system. *Chemical engineering science*, *66*(14), pp.3071-3086.

118. Tang, K-L., Ouyang, Y., Agarwal, R.K., Chen, J-M, Xiang, Y., Chen, J-F., 2020. Computation of gas-liquid flow in a square bubble column with Wray-Agarwal one-equation turbulence model, *Chem. Eng. Sci.* 218, 115551.

119. Talvy, S., Cockx, A. and Liné, A., 2007. Modeling of oxygen mass transfer in a gas–liquid airlift reactor. *AIChE Journal*, *53*(2), pp.316-326.

120. Tomiyama, A., Tamai, H., Zun, I. and Hosokawa, S., 2002. Transverse migration of single bubbles in simple shear flows. *Chemical Engineering Science*, *57*(11), pp.1849-1858.

121. Tzeng, J.W., Chen, R.C. and Fan, L.S., 1993. Visualization of flow characteristics in a 2-D bubble column and three-phase fluidized bed. AIChE journal, 39(5), pp.733-744.

122. Usera, G., Vernet, A., Pallares, J. and Ferré, J.A., 2006. A conditional sampling method based on fuzzy clustering for the analysis of large-scale dynamics in turbulent flows. European Journal of Mechanics-B/Fluids, 25(2), pp.172-191.

123. Vial, C., Camarasa, E., Poncin, S., Wild, G., Midoux, N. and Bouillard, J., 2000. Study of hydrodynamic behaviour in bubble columns and external loop airlift reactors through analysis of pressure fluctuations. *Chemical engineering science*, *55*(15), pp.2957-2973.

124. Vial, C., Laine, R., Poncin, S., Midoux, N. and Wild, G., 2001. Influence of gas distribution and regime transitions on liquid velocity and turbulence in a 3-D bubble column. *Chemical engineering science*, *56*(3), pp.1085-1093.

125. Vial, C. and Stiriba, Y., 2013. Characterization of bioreactors using computational fluid dynamics. In *Fermentation Processes Engineering in the Food Industry* (pp. 121-164). Taylor & Francis Group.

126. Vial, C., Poncin, S., Wild, G. and Midoux, N., 2001. A simple method for regime identification and flow characterization in bubble columns and airlift reactors. Chemical Engineering and Processing: Process Intensification, 40(2), pp.135-151.

127. Van den Hengel, E.I.V., Deen, N.G. and Kuipers, J.A.M., 2005. Application of coalescence and breakup models in a discrete bubble model for bubble columns. *Industrial & engineering chemistry research*, *44*(14), pp.5233-5245.

128. Van Den Akker, H.E., 1998. Coherent structures in multiphase flows. Powder Technology, 100(2-3), pp.123-136.

151

129. Vernet, A., Kopp, G.A., Ferré, J.A. and Giralt, F., 1999. Three-dimensional structure and momentum transfer in a turbulent cylinder wake. Journal of Fluid Mechanics, 394, pp.303-337.

130. Vitankar, V.S., Dhotre, M.T., and Joshi, J.B., 2002. A low Reynolds number $k - \varepsilon$ model for the prediction of flow pattern and pressure drop in bubble column reactors, *Chem. Eng. Sci.* 57, 3235–3250.

131. Weller, H.G., Tabor, G., Jasak, H. and Fureby, C., 1998. A tensorial approach to computational continuum mechanics using object-oriented techniques. Computers in physics, 12(6), pp.620-631.

132. Weller, H., 2002. A code independent notation for finite volume algorithms. Technical Report TR/HGW/02, Nabla Ltd.

133. Weller, H.G. and Derivation, M., 2005. Solution of the Conditionally Averaged Two-Phase Flow Equations. OpenCFD, Ltd.

134. Wang, T. and Wang, J., 2007. Numerical simulations of gas–liquid mass transfer in bubble columns with a CFD–PBM coupled model. Chemical engineering science, 62(24), pp.7107-7118.

135. Wilcox, D.C., 2006. Turbulence modeling for CFD. La Canada, CA: DCW Industries. Inc, November.

136. Ziegenhein, T., Rzehak, R., Ma, T. and Lucas, D., 2017. Towards a unified approach for modelling uniform and non-uniform bubbly flows. The Canadian Journal of Chemical Engineering, 95(1), pp.170-179.

137. Zhang, D., Deen, N.G. and Kuipers, J.A.M., 2006. Numerical simulation of the dynamic flow behavior in a bubble column: a study of closures for turbulence and interface forces. *Chemical Engineering Science*, *61*(23), pp.7593-7608.

138. Zehner, P., 1982. Momentum, mass and heat transfer in bubble columns. Intern. Chem. Eng. 26, 22-35